

The Pennsylvania State University
The Graduate School
Department of Electrical Engineering

**EFFICIENT OPTIMIZATION OF ANTENNA AND ELECTROMAGNETIC
DEVICES AT MEDIUM, RADIO, AND OPTICAL FREQUENCIES**

A Dissertation in
Electrical Engineering
by
Donovan E. Brocker

© 2016 Donovan E. Brocker

Submitted in Partial Fulfillment
of the Requirements
for the Degree of

Doctor of Philosophy

August 2016

The dissertation of Donovan Brocker was reviewed and approved* by the following:

Douglas H. Werner
Professor of Electrical Engineering
Dissertation Advisor
Chair of Committee

Timothy J. Kane
Professor of Electrical Engineering

Ram M. Narayanan
Professor of Electrical Engineering

Douglas E. Wolfe
Professor of Materials Science and Engineering

Kultegin Aydin
Professor of Electrical Engineering
Head of the Department of Electrical Engineering

*Signatures are on file in the Graduate School

ABSTRACT

The fast growth of computer technology has led to aggressive advancement in engineering design, where in the past, analytical methods and/or intuitive trial and error through experiments were the most lucrative tools. Specifically in electromagnetics, powerful computers can be used to run simulation models subject to numerical solutions of Maxwell's equations, providing extremely accurate predictions of the device performance. Growing computer resources also offer the ability to optimize devices via simulation, facilitating fine-tuning before fabrication. Hence, engineering design has drifted more and more towards computer modeling and optimization and has, in some cases, drifted away from intuition-based design and experimental fine-tuning. Although the former approach has the tendency to lower research and development costs and, at times, predict novel devices, the latter is still essential to the overall advancement of engineering design. With this in mind, this dissertation summarizes multiple efforts, ranging across many sub-fields of electromagnetics, where computer modeling and optimization was strongly coupled to intuitive design. This approach leads to efficient optimization of high performance designs that would likely not be possible with analytical or brute-force computer optimization alone. First, a hybrid approach combining transmission line equations and full-wave models is developed to optimize large communication networks in coal mines for emergency response applications. Secondly, a miniaturized dual-band antenna with an interdigitated slot load is proposed based on transmission line models and fine-tuned using computer simulation models. The antenna was fabricated and characterized, showing excellent agreement with simulation predictions. Next, an ultra-thin electromagnetic absorber design is proposed based on an equivalent circuit model. In particular, the circuit model is used to optimize the absorber design for wide bandwidth. Subsequently, the circuit model is used to simplify the optimization routine by cascading the scattering properties of the different absorber regions. Finally, gradient-index

lens design methodology is developed based on transformation optics, enabling superior mono- and polychromatic lens performances.

TABLE OF CONTENTS

List of Figures	vii
Acknowledgements.....	xii
Chapter 1 Introduction	1
1.1 Background	1
1.2 Overview of Problems.....	4
1.2.1 Transmission Line Models for the Efficient Modeling of Communication Networks in Coal Mines	4
1.2.2 Miniaturized Dual-Band Patch Antenna with Independent Band Control using an Interdigitated Slot Loading	4
1.2.3 Circuit Models for the Design and Optimization of Ultra-Thin Radio- Frequency Absorbers.....	5
1.2.4 Application of Transformation Optics for Mono- and Poly-chromatic Optimization of Gradient-Index Optical Lenses	6
1.3 Original Contributions	8
Chapter 2 Transmission Line Models for Optimization of Communication Links in Coal Mines.....	9
2.1 Introduction	9
2.2 A Hybrid Approach of Efficient Optimization of Communication Networks in Coal Mines	12
2.2.1 Initial Examples.....	18
2.2.2 Propagation with an Earth Return	22
2.2.3 Hybrid Approach for a Wire with Earth Return.....	25
2.2.3 Large-scale Optimizations using the Hybrid Approach	30
2.4 Conclusions.....	36
Chapter 3 Miniaturized Dual-Band Folded Patch Antenna with Independent Band Control Utilizing an Interdigitated Slot Loading	37
3.1 Introduction.....	37
3.2 Miniaturized WiFi Antenna Utilizing an Interdigitated Slot Loading	39
3.2.1 Fabrication Consideration and Simulation Results	41
3.2.2 Experiments.....	44
3.3 Independent Band Control of the Interdigitated Slot Loading.....	46
3.3.1 Antenna Performance Sensitivity Analysis	46
3.3.2 Independent Frequency-Band Control	50
3.4 Considerations of Utilizing Small Ground Planes	51
3.5 Conclusions.....	53
Chapter 4 Ultra-thin Radio Frequency Absorber Design using Circuit Approximations	55

4.1 Introduction.....	55
4.2 Two-Layer Absorbers: Ultra-Thin Absorbers Comprised by Cascaded High-Impedance and Frequency Selective Surfaces	55
4.3 Single Layer FSS Design for Further and Path for Thickness Reduction.....	66
4.4 Conclusions.....	74
Chapter 5 Optimization of Optical Lens Systems Using Transformation Optics and a Custom Ray Tracer for Arbitrary 3-Dimensional Gradient-Index Profiles	75
5.1 Introduction.....	75
5.2 Spherical Aberration Correction by Applying Asphere-to-Sphere Transformations	75
5.3 Achromatic Gradient-Index Lens Design using Transformation Optics.....	85
5.4 Transformation Optics-Inspired Achromatic Gradient-Index Lens Design.....	89
5.4.1 Axial Chromatic Aberration of Classic Lenses	90
5.4.2 Axial Chromatic Aberration of a Ge-Si GRIN Singlet	91
5.5 Dispersion Corrected Dispersive Metamaterial Lenses using Ray Tracing Equations.....	94
5.6 Field-of-View Enhancement of Gradient-Index Lenses Inspired by Transformation Optics.....	101
Chapter 6 Summary and Suggestions for Future Work	111
6.1 Summary	111
6.2 Suggestions for Future Work	112
Bibliography	114

LIST OF FIGURES

Figure 2.1. Comparison of a strictly full-wave model to a hybrid model using both full-wave regions and transmission line equations.	13
Figure 2.2. Example geometry constructed to determine the full-wave sections required to accurately calculate power transfer from Tx to Rx.	15
Figure 2.3. Required length of full-wave (moment method) section to accurately couple electromagnetic energy from a small antenna element to the twin lead transmission line shown in Fig. 2.2.	16
Figure 2.4. Geometry of a T-intersection full-wave and hybrid model comparison using open, shorted, and matched terminations.	19
Figure 2.5. Currents calculated using equivalent full-wave and hybrid models. The calculated current magnitudes were normalized to the source current.	20
Figure 2.6. Geometry of a $27 \lambda_0$ long TL (<i>i.e.</i> 16.2 km) placed between two parallel boundaries of lossy earth used to test the hybrid model subject to environmental loading.	22
Figure 2.7. Current magnitudes and phases calculated on the R_x TL section were compared between full-wave and hybrid models for shorted and open terminations.	22
Figure 2.8. Geometry of single wire above lossy earth and free space boundary.	23
Figure 2.9. Geometry: 1-mm radius wire placed 20 cm above lossy earth return.	27
Figure 2.10. Currents for full-wave and hybrid models were calculated and are compared for both shorted and open terminations.	27
Figure 2.11. (a) Geometry: wire placed above a lossy earth return. (b) Geometry: wire placed above a mine tunnel floor. (c) Side-view of mine tunnel hybrid model with a wire positioned 50 cm above a mine floor.	28
Figure 2.12. Currents for full-wave and hybrid models were calculated and are compared for both shorted and open terminations and two different return path conductivities.	30
Figure 2.13. Large TL network used to demonstrate the feasibility of performing large-scale optimizations by utilizing the hybrid approach. The optimization protocol was to simultaneously maximize power transfer from T_x to three different receivers by implementing open and shorted terminations at each node and endload.	32
Figure 2.14. Map of mining area showing room-and-pillar layout.	33
Figure 2.15. Geometry for optimization problem using the hybrid approach. A network of single conductors is constructed and optimized for minimum SWR on the segments	

nearest to the transmitter and receiving antennas. Optimization is performed by varying the length of grounding rods at the end of each open segment.....	34
Figure 2.16. (a) Current comparison for optimized hybrid and full-wave models. (b) Current comparison for hybrid and full-wave model after a line break was introduced. The TL section corresponding to R_{x1} is located after the TL break, as is evident in the relatively small current magnitudes.....	35
Figure 3.1. Configuration of the proposed antenna structure: (a) perspective and (b) side geometric views.	40
Figure 3.2. Fabricated antenna used for validation. (Left) shows a perspective view of antenna with foam inserts and (right) shows a side view of antenna without foam inserts.....	42
Figure 3.3. (a) Surface currents around the interdigitated slot at 2.4 GHz and (b) 5.0 GHz. The arrows' colors and direction represent the current magnitude and phase, respectively.	43
Figure 3.4. Simulated and measured S_{11} of the antenna.....	44
Figure 3.5. (a) Simulated and measured normalized radiation patterns of antenna element in the E -plane at 2.4 GHz and (b) 5.0 GHz. (c) Simulated and measured normalized radiation patterns of the antenna element in the H -plane at 2.4 GHz and (d) 5.0 GHz....	46
Figure 3.6. Simulated and measured broadside realized gains of antenna element.	46
Figure 3.7. Simulated S_{11} of the antenna with varying (a) L_1 and (b) W	49
Figure 3.8. Simulated S_{11} of the antenna with varying (a) h_1 and (b) h_2	49
Figure 3.9. Simulated S_{11} of the antenna with varying (a) R_L and (b) R_W	50
Figure 3.10. Simulated S_{11} and broadside gain of three antenna designs utilizing the same folded antenna base with different interdigitated slot loadings. The TM_{30} mode was independently shifted by up to 10%. Design 1 corresponds to interdigitated slot geometry of $R_W = 0.8328W$ and $R_L = 0.8485L_2$. Design 2 corresponds to $R_W = 0.8837W$ and $R_L = 0.7851L_2$. Design 3 corresponds to $R_W = 0.9584W$ and $R_L = 0.6711L_2$. All other antenna values are common to each design and are given in Table 1 column 2.....	51
Figure 3.11. Simulated co-polarized forward and backward gains of antenna element.	53
Figure 3.12. Simulated co-polarized forward gain and maximum cross-polarization in the H -plane.....	53
Figure 4.1. Equivalent circuit of an HIS loaded by a series RLC circuit. (b) HIS susceptance along with the susceptance of the RLC load for increasing values of $R_2 = 0 \Omega$ and $R_2 = 200 \Omega$	58

Figure 4.2. (a) Total admittance of the <i>RLC</i> loaded HIS. (b) Absorber reflection coefficient.....	59
Figure 4.3. (a) Absorber unit cell side view. (b) Transmission line equivalent of the loading scheme.....	60
Figure 4.4. (a) Pixelized FSS. Copper corresponds to PEC and white to free space. (b) Input susceptance of the HIS, the targeted series lossless <i>RLC</i> circuit, and the pixelized FSS.	61
Figure 4.5. Comparison between the full-wave input susceptance of the HIS loaded by a lossless pixelized FSS, against the semi-analytical transmission line model for four different HIS/FSS separation distances.....	63
Figure 4.6. Reflection coefficient corresponding to the four absorber designs.	65
Figure 4.7. Circuit models for the (a) absorber and the (b) fss with PEC-backed substrate and loss removed.....	67
Figure 4.8. Array of patches (a) 2D geometry and simulation model, (b) circuit model, and (c) input reactance.	68
Figure 4.9. Fishnet (a) 2D geometry and simulation model, (b) circuit model, and (c) input reactance.	69
Figure 4.10. Parallel patch-fishnet configuration (a) 2D geometry and simulation model, (b) circuit model, and (c) input reactance.	69
Figure 4.11. Parallel patch-Jerusalem cross configuration (a) 2D geometry and simulation model, (b) circuit model, and (c) input reactance with C_{patch} (C_{eff}) and $L_{fishnet}$ values given in the legend of Fig. 4.10c and $C_{gap} = 50$ fF.....	70
Figure 4.12. Predicted S_{11} of circuit model optimization.....	71
Figure 4.13. (a) Optimized FSS geometry and simulation model, where $a = 6.546$ mm, $trace = 0.139$ mm, $gap = 0.067$ mm, and $gap = 0.364$ mm. (b) Optimized circuit model. (c) Complex reflection coefficient of simulated FSS compared with circuit model.....	72
Figure 4.14. Optimized FSS with PEC-backing (a) geometry and simulation model, (b) circuit model, and (c) complex reflection coefficient comparison.....	73
Figure 4.15. Absorber S_{11} comparison.....	73
Figure 5.1. Illustration of bulk and layered qTO geometries for the GRIN asphere lenses.....	77
Figure 5.2. qTO-optimized GRIN profiles for the bulk and layered GRIN $f/2.5$ asphere lenses with 10 mm entrance pupil diameter. (Top) Bulk GRIN lens. (Center) Thick-layered GRIN lens. (Bottom) Thin-layered GRIN lens.	80

Figure 5.3. (Top) Surface contours of each lens design. Note that the surface contours of the GRIN lenses correspond to the virtual domain definition. (Center) Asphere contours. (Bottom) Normalized asphere contours.....	83
Figure 5.4. Example coordinate transformation used for dispersion correction.	87
Figure 5.5. GRIN material requirement for dispersion-correction.	88
Figure 5.6. Focal drift of a standard homogeneous and TO-corrected GRIN lens.	89
Figure 5.7. Ray trace diagrams and refractive index distributions of the (a) Germanium singlet, (b) Silicon singlet, (c) Germanium-Silicon doublet, and (d) Germanium-Silicon GRIN singlet.....	93
Figure 5.8. (a) Geometry and GRIN profile of metamaterial lens at the center frequency f_2 and (b) dispersive properties of metamaterial.	98
Figure 5.9. (a) COMSOL simulations showing focal drift of flat and (b) dispersion-corrected metamaterial lenses. The black vertical lines mark the targeted focus.	99
Figure 5.10. Lens surface curvature as a function of GRIN ratio and lens thickness for f/2.0 singlet: (top) total surface radii and (bottom) total surface curvature.	99
Figure 5.11. Normalized intensity profiles for flat and dispersion-corrected metamaterial lenses with (a) 25-lambda and (b) 5-lambda apertures. Dashed, dash-dot, and solid lines correspond to frequencies 1, 2, and 3, respectively. The plots show a reduced focal drift for the dispersion-corrected lenses.	100
Figure 5.12. Flattened Luneburg lens GRIN profile and ray trace at 0 degrees (blue), 15 degrees (green), and 30 degrees (red).	101
Figure 5.13. Polynomial fitting of flattened Luneburg lens without the use of cross-terms. The order of the polynomial was varied from 2 to 12. Without cross-terms, the polynomial fitting routine cannot reproduce the characteristics of the Luneburg.....	103
Figure 5.14. Polynomial fitting analysis with no cross-terms: (a) Polynomial fitting maximum and mean error, (b) foci location in the x-y plane at 0, 15, and 30 degrees, and (c) minimum RMS spot size at 0, 15, and 30 degrees. Analyses are functions of polynomial order.	104
Figure 5.15. Polynomial fitting of flattened Luneburg lens with the use of cross-terms. The order of the polynomial was varied from 2 to 12. The polynomial fitting routine successfully reproduces the characteristics of the Luneburg once cross-terms are introduced.....	105
Figure 5.16. Polynomial fitting analysis including cross-terms: (a) Polynomial fitting maximum and mean error, (b) foci location in the x-y plane at 0, 15, and 30 degrees, and (c) minimum RMS spot size at 0, 15, and 30 degrees. Analyses are functions of	

polynomial order. The polynomial-fitted Lunenburg lens converges to diffraction limited performance at approximately order 12.	106
Figure 5.17. Comparison of various lens types over a (a) 20 degree half-FOV and (b) 5 degree half-FOV.	107
Figure 5.18. Eight-term radial GRIN with significantly improved 30-degree FOV. (a) Ray trace of chief and marginal rays for 0, 5, 10, and 15 degrees incidence. (b) Zoom of 51-ray trace focal plane. Spot sizes were calculated to be 110, 165, 328, and 518 μm at 0, 5, 10, and 15 degrees, respectively.....	108
Figure 5.19. Eight-term axial-radial GRIN with significantly improved 30-degree FOV. (a) Ray trace of chief and marginal rays for 0, 5, 10, and 15 degrees incidence. (b) Zoom of 51-ray trace focal plane. Spot sizes were calculated to be 108, 154, 328, and 540 μm at 0, 5, 10, and 15 degrees, respectively.....	109
Figure 5.20. Eight-cross-term GRIN with significantly improved 30-degree FOV. (a) Ray trace of chief and marginal rays for 0, 5, 10, and 15 degrees incidence. (b) Zoom of 51-ray trace focal plane. Spot sizes were calculated to be 26, 46, 65, and 77 μm at 0, 5, 10, and 15 degrees, respectively.	109

ACKNOWLEDGEMENTS

This dissertation would not have been possible without the support from numerous people. First and foremost, I would like to express my utmost gratitude to my advisor and committee chair, Dr. Douglas H. Werner, for his invaluable academic and gracious financial support throughout my Ph.D. work. I would also like to thank Dr. Timothy J. Kane, Dr. Ram M. Narayanan, and Dr. Douglas E. Wolfe for serving on my committee and providing valuable feedback on my dissertation.

I owe thanks to all of the students and postdoc researchers that I have collaborated with for their fruitful discussions, support, and help: Philip Gorman, Spencer Martin, Zikri Bayraktar, Xiande Wang, Qi Wu, Jeremy Bossard, Micah Gregory, Frank Namin, Jeremy Turpin, Clinton Scarborough, Yong Zeng, Jason Ashbach, Sawyer Campbell, Qiang Ren, Daniel Binion, John Easum, Bingqian Lu, Idellyse Martinez, Joe Nagar, Yifeng Qin, Tiawei Yue, Danny Zhu, Kenneth Morgan, Zachary Morgan, Cooper Cicero, and Lei Kang. I also note particular gratitude to Anastasios Panaretos, Zhi Hao Jiang, and Peter E. Sieber, for their companionship and dedicated guidance throughout my Ph. D research.

I also would like to thank new friends I have met during my stay in State College; particularly, Spencer Martin, Phil Gorman, and Elle Haberer, for my time here would not have been the same without them. I also thank my dear friends back in Milwaukee, Josh Delaney, Cory Elbert, S. Michael Krause, and Nate Winter, for always providing me with the kind of support and entertainment that professional colleagues and family cannot. Finally, I express my deepest love to my family, Edward, Belinda, and Chelsea Brocker, who have always provided me with all forms of support and encouragement.

To Belinda and Edward, my beloved parents. To my sister, Chelsea.

To the city of Milwaukee, for shaping who I am; I will always belong to you.

Chapter 1

Introduction

This chapter introduces the topic of the dissertation, which is the application of approximate methods for efficient optimization of RF and optical systems. A brief background on computer aided-design of electromagnetic (EM) systems is given, followed by a more detailed explanation of the research goals for this dissertation. Finally, an overview of the specific EM problems considered is given in addition to the original contributions made.

1.1 Background

The field of EM has undoubtedly evolved with the invention and advancement of computers. With what seems like increasingly limitless computational resources available to more and more engineers, so too grows their ability to predict EM phenomena and model devices previously unimaginable. An example is the prediction of negative refractive index materials in 1968 [1]. It was not until decades later, after advancements in manufacturing and computing, that this obscure idea could be revisited [2, 3]. This approximately marks the infancy of the field of metamaterials [4]. Metamaterials achieve their esoteric characteristics by exploiting engineered resonant EM responses. Furthermore, utilizing sub-wavelength features, metamaterials can often be engineered locally using circuit equations while simultaneously considered globally as an effective medium, analogous to the way collections of atoms create bulk materials. Following shortly after the advent of metamaterials was the birth of Transformation Optics (TO) [5-7], which exploits the invariance of Maxwell's equations by interpreting a bending of 3-dimensional space as a material distribution in a different volume. These material compositions are generally

inhomogeneous and anisotropic. Because of this near-arbitrary bending of space, many incredible new devices were predicated with never before seen properties including invisibility cloaks [8-10], omni-directional field concentrators [11], electromagnetic ‘black holes’ [12], reflectionless beam bends and splitters [13], polarization rotators [14], flattened lenses [15, 16], and reconfigurable surface plasmon polariton wave adapters using liquid crystals [17].

As previously stated, the successes of metamaterials and TO would not be what they are today without the aid of computers, which can be used to simulate numerical solutions to Maxwell’s equations using techniques such as method of moments (MoM), finite-element method (FEM), and finite-difference time-domain (FDTD). Furthermore, computer resources have also been increasingly allocated for utilizing optimization algorithms, such as the genetic algorithm (GA) [18-20], particle swarm optimization (PSO) [21-23], differential evolution (DE) [24,25], and the covariance matrix adaptation evolutionary strategy (CMA-ES) [26-28], in EM design. The goal of these algorithms is the same: to find the best set of design parameters that satisfies the objectives for a given problem. Such algorithms are often applied when local, gradient-based search algorithms are not able to do a sufficient global search within a multi-modal, nonlinear, and/or noisy objective space. As a result, global optimization algorithms are often able to find suitable candidate designs in design spaces that would be impossible to search otherwise.

Finally, combining state-of-the-art optimization algorithms to EM numerical software provides engineers with a powerful design framework. With that said, such computational resources should not be used to replace the utility of intelligent physics-based engineering design. Simple uninspired, brute-force computer optimization typically leads to inefficient design processes. Furthermore, it is often very difficult to learn from a design task when little to no intuition is used while setting up a problem and subsequently analyzing the results.

This dissertation considers various EM problems where physical concepts are applied in a way to simplify or approximate full-wave analysis. As a result, computational requirements are

reduced and often physical insight is gained. The EM problems considered are: 1) modeling medium frequency propagation in coal mines, 2) miniaturized RF antenna design, 3) RF absorber design, and 4) gradient-index (GRIN) optical lens design. These design problems are put into two general categories:

1. Fine-tuning

In this class of problems, before optimization, simplifications and approximations have been applied to provide designs that come close to meeting all objectives. Optimizations are used to subsequently fine-tune the design to an optimal solution. An example of this would be to first apply circuit equations to design a patch antenna, getting it close to the desired resonant frequency, and then linking an optimization algorithm to a full-wave solver for final fine-tuning.

2. Assisted/Intelligent Global Search

In this class, a global search is necessary for finding designs that satisfy a given set of criteria. However, the search routine is accelerated, with respect to time, by applying approximate methods to either replace EM full-wave numerical solvers or to work in tandem with them. An example of this is the signal distribution on a transmission line network where an antenna is the source. In this example, the coupling between the antenna and nearby transmission line conductors would be modeled with full-wave techniques while the subsequent signal propagation through the remaining transmission line network could be modeled using efficient transmission line equations.

1.2 Overview of Problems

1.2.1 Transmission Line Models for the Efficient Modeling of Communication Networks in Coal Mines

In the second chapter, an efficient procedure for modeling medium frequency (MF) communications in coal mines is introduced [29]. In particular, a hybrid approach is formulated and demonstrated utilizing ideal transmission line (TL) equations to model MF propagation in combination with full-wave sections used for accurate simulation of local antenna-line coupling and other near field effects. This work confirms that the hybrid method accurately models signal propagation from a source to a load for various system geometries and material compositions, while reducing computation time by factors into the hundreds. With such dramatic improvement to solution times, it becomes feasible to perform large-scale optimizations with the primary motivation of improving communications in coal mines both for daily operations and emergency response. Furthermore, it is demonstrated that the hybrid approach is suitable for modeling and optimizing large communication networks in coal mines that may otherwise be intractable to simulate using traditional full-wave techniques such as moment methods or finite element analysis.

1.2.2 Miniaturized Dual-Band Patch Antenna with Independent Band Control using an Interdigitated Slot Loading

In Chapter 3, a compact linearly polarized dual-band patch antenna with independent band control for WiFi applications is presented [32, 33]. Miniaturization was achieved through a combination of shorting, folding, and by replacing the standard slot loading with a slot that features a meander-line. Importantly, by employing this interdigitated slot the patch surface current distributions at each operational frequency band were swapped when contrasted with the

conventional slotted patch antenna, facilitating antenna miniaturization and resulting in an element equal to or smaller than $0.1\lambda_0$ in all three Cartesian dimensions. A detailed antenna design procedure is outlined and a prototype was fabricated and measured for impedance matching, radiation pattern, and broadside gain. A simulated parametric analysis was carried out to determine how sensitive the antenna performance is to each geometric parameter. Then, based on the sensitivity analysis, it was further demonstrated that the two operational bands of the antenna element could be independently controlled by changing only the geometrical dimensions of the interdigitated slot, leaving the base of the antenna entirely unaltered. As a result, the lower operating band could be fixed while the upper operating band could be shifted by up to 10%. Lastly, the effect of utilizing a small ground plane, in an effort to achieve a small antenna footprint, is discussed. It was determined that the small ground plane needed to be included in the overall antenna design due to the strong diffraction and subsequent contribution to the radiation pattern.

1.2.3 Circuit Models for the Design and Optimization of Ultra-Thin Radio-Frequency Absorbers

In Chapter 4, the theoretical basis for an ultra-thin broadband absorber is established [34]. Initially a 2-layer design is proposed, which is comprised of a mushroom-type High Impedance Surface (HIS) and a pixelized Frequency Selective Surface (FSS). The latter is engineered to exhibit a prescribed series *RLC* circuit response and it is placed at an electrically small distance above the HIS. Through a transmission line analysis it is demonstrated that the admittances of the two structures cancel each other out resulting in an almost zero input reactance and a resistance that fluctuates around that of free space within the frequency range of interest. The resulting

structure has a total thickness that does not exceed 2 mm while achieving a -10 dB S_{11} for normal incidence from 9-13 GHz.

Next, a single-layer absorber is developed based on the findings from the 2-layer design. By revisiting the circuit approximations of the FSS design, the series *RLC* contribution from the previous FSS was embedded into the patch region of the 2-layer design, resulting in a single-layer absorber design. A 2-mm-thick design was targeted for direct comparison with the 2-layer absorber. It was found that in addition to improved manufacturability, the single-layer absorber displayed improved bandwidth. Furthermore, the layer-to-layer coupling that was experienced in the 2-layer design, leading to degradation in the realized absorption bandwidth, was eliminated in the single-layer absorber design.

1.2.4 Application of Transformation Optics for Mono- and Poly-chromatic Optimization of Gradient-Index Optical Lenses

The final chapter focuses on applying TO to design high performance all-dielectric gradient-index (GRIN) lenses. GRIN lenses are predicted by many to have superior performance compared with lens systems using conventional homogeneous material compositions. Namely, the complexity of classic (i.e. homogeneous) multi-lens sequences required for high performance optical systems can be instead manifested into GRIN profile complexity, allowing for refraction throughout the volume of a lens and not just at the physical surface boundaries. As GRIN material technologies continue to evolve, facilitating more practical GRIN lens implementations, the knowledgebase and design tools to optimize GRIN lens systems must simultaneously evolve.

First, by using quasi-conformal mappings we demonstrate spherical-aberration-corrected lenses with spherical surface profiles by mimicking the optical behavior of aspherical lenses [35]. Several approaches for mapping aspherical to spherical contours are described and contrasted,

including the use of bulk GRIN regions throughout the entire lens as well as layered designs where the GRIN profiles are restricted to thin laminar layers at the surface of the otherwise homogeneous lens. Hence, the proposed methodology provides engineers with a powerfully intuitive means to design, compare, and contrast various equivalently performing GRIN lenses, adding new modeling capabilities to the existing, well-known remedies for optical system optimization. Furthermore, such an approach facilitates straightforward monitoring and manipulation of material gradients and overall change in refractive index.

Next, TO was applied to interpret the dispersive nature of materials via changes in geometry, providing an alternative methodology for dispersion correction [36]. A GRIN lens example is proposed and analyzed to demonstrate the effectiveness of the proposed technique. The findings of this study are subsequently applied to consider a more general methodology for designing achromatic GRIN lenses. A GRIN focusing lens based on the mixing of Germanium (Ge) and Silicon (Si) is proposed and designed to have minimal focal drift [37]. Subsequently, a related analytical method based on paraxial ray-tracing equations is proposed for designing GRIN metamaterial lenses with dispersion-correction [38]. An instructive example is considered to demonstrate the effectiveness. Finally, a design approach based on the flattened Luneburg lens [39] is proposed for predicting GRIN lenses with improved field-of-view (FOV). By decomposing the flattened Luneburg, which is a GRIN lens known to have good FOV, into a polynomial basis, it is determined that polynomial cross-terms (those with non-zero mixed partial derivatives) are required to accurately represent the flattened Luneburg. Notably, little to no discussion of cross-terms has been previously reported, in large part to the analytical difficulty and lack of support in commercial ray tracing software. An example demonstrates the stark advantages of GRIN profiles utilizing polynomial cross-terms, particularly for improved FOV.

1.3 Original Contributions

The research that I have performed during my Ph.D. studies at Penn State has led to several new developments in the fields of RF and optical system design, including:

- Development of a hybrid solution method, combining efficient transmission line models with method of moments, for efficient modeling of large emergency response communication networks in coal mines.
- Design, fabrication, and characterization of miniaturized dual-band WiFi antenna utilizing an interdigitated slot loading with independent operational frequency band control.
- Design of ultra-thin electromagnetic absorbers based on low-frequency circuit representations of frequency selective surfaces.
- Development of spherical aberration correction theory based on asphere-to-sphere transformations.
- Development of GRIN lens achromatic theory by introducing a set of independent quasi-conformal mappings for each wavelength, then interpreting the results to provide a practical method for color-correction.
- Development of achromatic theory for GRIN metamaterial lenses using paraxial ray-tracing.
- Development of a GRIN lens design for improved field-of-view by introducing polynomial cross-terms.

Chapter 2

Transmission Line Models for Optimization of Communication Links in Coal Mines

2.1 Introduction

Reoccurring tragedies have emphasized the need for communication systems in the mining industry with improved survivability. In response to such types of disasters, the United States Congress passed the Mine Improvement and New Emergency Response (MINER) Act in 2006, considered to be the most significant mine safety legislation since the Federal Mine Safety and Health Act of 1977. Over the years, researchers have performed extensive research on the design optimization and implementation of communication systems for use in coal mining operations [40-44]. A large range of frequencies have been proposed for various types of coal mine communications, ranging from VHF and UHF technologies [45-54], typically for in-mine daily operations, to emergency tracking systems [55-59] based on VLF through-the-earth technologies. Medium frequencies have also been proposed for in-mine communications [47], [60-69], which is the focus of this chapter.

Medium frequencies are identified for their ability to parasitically couple into conductor infrastructure within a mine tunnel and propagate large distances through various room-and-pillar architectures with relatively low attenuation [66, 67]. In practice, this means that an MF system may take advantage of existing conductor infrastructure in a coal mine, only requiring wireless handhelds for communications. Examples of typical conductors in mines include trolley rails, lighting and telephone wiring, and machinery power cables. Another advantage of MF signals is their ability to propagate hundreds of meters through the coal seam without metallic conductors present [70, 71], because the relative conductivities of the coal and surrounding rock layers can form a suitable waveguide. As mandated by the MINER Act, current research efforts are to

primarily focus on improving the survivability of existing technologies and developing new solutions for emergency tracking. Hence, the characteristics outlined above make MF communications attractive for day to day mining operations as well as in the event of an emergency, although the low carrier frequency generally limits the system to a single channel. As a result, there is a renewed interest in MF technologies [29,72-78] to address this mandate.

The current modes that can be excited along multiple-conductor configurations within a coal mine tunnel are characterized as differential mode (DM) and common mode (CM) propagations. DM refers to propagation 180 degrees out of phase along conductors; CM refers to in-phase propagation along conductor networks whereby currents return through surrounding mine-earth boundaries. Many times one mode is dominant in a communication system; however, the most general propagation is a superposition of both CM and DM. Furthermore, CM and DM propagation modes can experience discernible differences in attenuation and coupling efficiency from antenna to transmission line [79-81]. Because of these differences, accurate modeling of both modes is crucial for understanding and optimizing MF communications in coal mines. The remainder of this chapter will demonstrate the proposed hybrid approach by concentrating on each mode individually and leaves multimodal (or, multiconductor) transmission line analysis for consideration in future work. Looking forward, when the proposed hybrid approach is extended to accommodate multiconductor systems, it will be constructed in the same way as outlined in this chapter, with the difference in that TL models would be represented by matrix equations to accommodate multiconductor configurations [82-84].

In order to determine what factors most influence the behavior of MF propagation in coal mines, extensive numerical and analytical modeling is required. Many previous models of MF propagation in earth-bounded systems [85, 86] develop modal equations that require sophisticated numerical methods in order to facilitate accurate calculations. Alternatively, constructing representative models using commercial method of moments (MoM) codes presents a separate

challenge because they require considerable computational resources and time. For example, a typical coal mine tunnel cross section is on the order of meters, suggesting information about the meshing resolution of the MoM model; meanwhile, the length of a mine may be on the order of kilometers, indicating the overall size of the model. Hence, full-wave simulation of signal propagation from one end of a mine to another can become an extremely large problem for traditional computational electromagnetic (EM) modeling codes. The hybrid approach outlined and demonstrated in the following sections mitigates this challenge. The general concept is illustrated in Fig. 2.1, showing “black box” regions of interest that are to be modeled using MoM. These sections could contain a source/transmitter coupling to a transmission line, a load/receiver receiving a signal from a transmission line, or a line break and scattered overburden due to a mine collapse; essentially, these sections are used to model anything not trivially represented by simple analytical expressions. In contrast, interconnects for these regions are typically a network of conductors, or a transmission line, providing a uniform path for MF propagation and hence can be modeled with simple TL equations. This technique allows for efficient simulation of communication paths while providing modeling flexibility and enabling parametric investigations of the source and receiver/load sections in addition to effects associated with mining disaster events. Exhaustive parametric studies of excitation (*i.e.* antenna-line coupling) and line termination types would be impractical, if not impossible, if the entire propagation path in a given communication link were modeled using full-wave techniques alone. As will be demonstrated, this hybrid approach significantly reduces the amount of computational resources and time required to make calculations of interest.

Ultimately, a primary objective of this work is to facilitate system-level optimization of coal mine communication networks. For example, optimizations may include maximizing power transfer from a transmitting antenna to a receiving antenna and minimizing standing wave ratio (SWR). Another goal may be to design an MF communication system that is more survivable

during disaster events. In order to efficiently optimize such large problems, specialized global search algorithms were used in conjunction with the proposed hybrid model to analyze fitness of candidate network designs. Such an optimization technique, which may require hundreds or even thousands of function evaluations, would not be feasible without the significant improvement of solution times afforded by the hybrid approach. For demonstration, the final example in this work minimized SWR ratio near the transmitting and receiving antennas of an MF communication network. Subsequently, a line break was introduced to the previously optimized design, simulating the event of a mine collapse. Once again the hybrid approach was applied by modeling the broken TL with a full-wave region and it was shown to accurately reproduce the corresponding propagation effects and power losses. These effects would be difficult to reproduce applying only TL equations; however, on the other hand the entire communication network is too large to model and optimize using MoM or FEM techniques alone. The solution is to use both full-wave and TL models in a hybrid approach, which is formulated in the follow sections with examples to demonstrate the efficiency, accuracy, and modeling versatility it can offer.

2.2 A Hybrid Approach of Efficient Optimization of Communication Networks in Coal Mines

When constructing the hybrid models, it is important to both maintain accuracy and minimize solution times. That is, when properly implemented, a hybrid model should yield results consistent with its full-wave counterpart (*i.e.* no TL equations) and reduce the corresponding calculation time. Medium frequency propagation in a coal mine, whether along multiple conductors in a DM state or those involving lossy earth return paths, can commonly be approximated as TEM modes [80]. When a quasi-TEM approximation is valid, full-wave sections in a MoM model can be represented by TL equations; this is how the hybrid approach is

constructed. Full-wave sections are strategically retained within a hybrid model to include local effects such as antenna-line coupling and other near field interactions that are difficult to generalize with TL equations. This general idea is illustrated in Fig. 2.1.

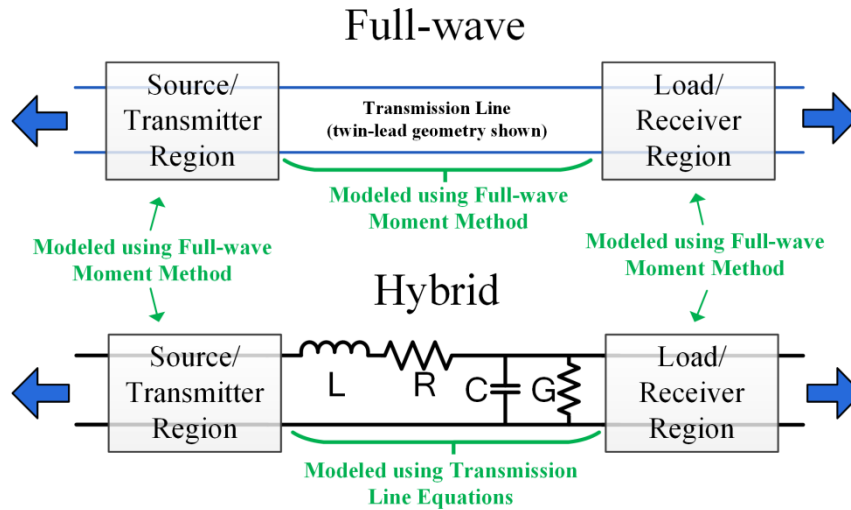


Figure 2.1. Comparison of a strictly full-wave model to a hybrid model using both full-wave regions and transmission line equations.

There are two major steps to perform when constructing a hybrid model for a given MF communication system: 1) determine adequate sizes for all full-wave sections, capable of capturing sufficient detail of the near-field interactions within the system and 2) determine the TL equations that best represent the uniform MF propagation occurring in the coal mine communication network. In other words, “what is the correct ratio of full-wave sections to TL equation sections?” This is important since the smaller and less frequent the full-wave sections are, the smaller the resulting computational cost.

Starting with the determination of the full-wave sections, consider two examples of particular interest for analyzing and optimizing the survivability of a communication network. First, consider a transmission line excited by a transmitting antenna. The length of the

transmission line in the vicinity of the transmitter must be adequately long in order to capture the correct antenna-to-line coupling. A hybrid model with this type of full-wave section could be used to determine how best to excite an MF communication network in an underground mine. Because the antenna coupling section is modelled using full-wave techniques, it would be straightforward to move the antenna, change its orientation, or change its position and then use the TL equations within the hybrid approach to calculate the impressed currents on the remainder of communication network. For the second important example, consider a broken transmission line due to a collapsed tunnel. Again, it is extremely important to use a full-wave region sufficiently large enough to accurately model the power losses associated with the broken transmission line.

Based on the experience gained from this work, there is no generalizable procedure that can answer how much of a given MF communication network should be modeled using full-wave sections and how much can be modeled using TL equations. In fact, this highlights the motivation behind the hybrid approach. That is to say, if the designer could trivially model and predict how various antennas would couple to a given communication network, and how that network would respond to extreme environmental changes induced by a mine collapse, then analytical expressions, such as transmission line equations, would suffice alone. Unfortunately, this modeling task is not so straightforward. Hence, choosing the appropriate full-wave sections must be done on a case-by-case basis.

To show how this was typically done in this work, an example was constructed which is outlined in Fig. 2.2 showing a twin-lead transmission line having a separation distance of 2 m and wire radius of 1 mm ($Z_0 = 911 \Omega$). The transmission line, which was terminated at both ends with loads Z , was positioned near two small loop antennas (20-cm diameter) separated by a distance L that were displaced from the plane of the transmission line by a distance Δx . The objective in this example was to determine what length of the transmission line near the two antennas must be

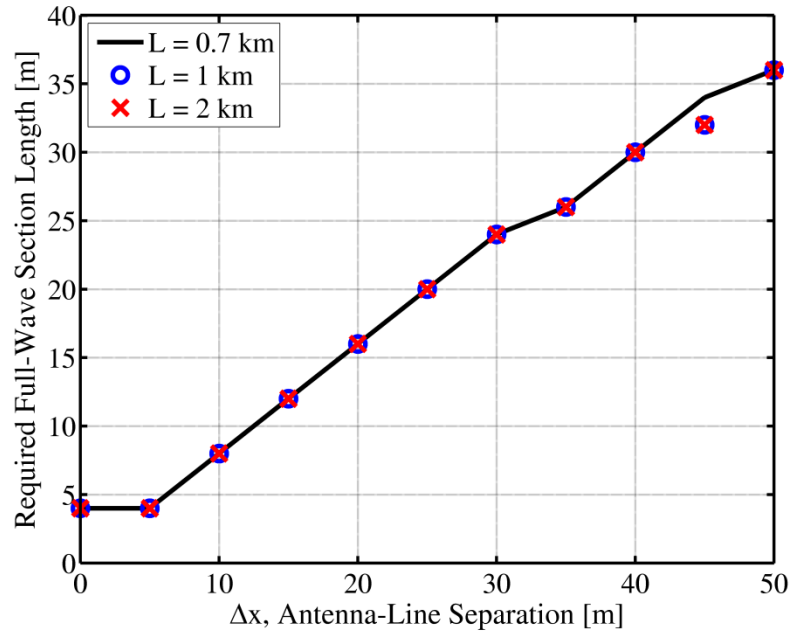


Figure 2.3. Required length of full-wave (moment method) section to accurately couple electromagnetic energy from a small antenna element to the twin lead transmission line shown in Fig. 2.2.

Note that even though this example suggested rather short full-wave sections were required to model accurate antenna coupling, all of the examples explored in the remainder of the chapter made use of longer ($\sim\lambda/4$ to $\lambda/2$) full-wave sections. The main reason for this was so that when presenting hybrid model calculations the variations in line current magnitude and phase could be easily identified and compared with the full-wave equivalent models.

In order to apply TL equations to the hybrid models, the propagation constant and characteristic impedance associated with the system must be calculated beforehand. With this data, TL equations may be formulated to calculate the equivalent loading and excitation on the full-wave sections associated with the sources and loads (*e.g.* transmitters and receivers), respectively. The TL propagation constant and characteristic impedance can be calculated using

either numerical or analytical techniques. Typically, closed form solutions are preferred due to the ease with which calculations can be made; however, they are not always available for the diverse range of geometries and materials commonly encountered in coal mines. Many times only approximate solutions or more complex modal equations can be formulated. In this respect, it can be most straightforward to use available commercial codes to model prescribed geometries and calculate the associated propagation characteristics. For example, when considering low-loss TL, it can be shown that the propagation phase and attenuation constants are approximated by [75]

$$\beta = \frac{1}{2L} \left(\arctan \left[\frac{\operatorname{Im} \left(\frac{1+A}{1-A} \right)}{\operatorname{Re} \left(\frac{1+A}{1-A} \right)} \right] + 2m\pi \right) \quad (2.1)$$

and

$$\alpha = \frac{1}{2L} \ln \left| \frac{1+A}{1-A} \right|. \quad (2.2)$$

Here, L is the length of the TL, m is a non-negative integer, and $A = \sqrt{Z_{sc} / Z_{oc}}$, where Z_{sc} and Z_{oc} are the input impedances for shorted and open terminations, respectively. Finally, the characteristic impedance can be calculated by [87]

$$Z_0 = \sqrt{Z_{oc} Z_{sc}}. \quad (2.3)$$

In this way, the parameters required for the TL equations of the hybrid approach can be solved by calculating only the input impedances corresponding to open and shorted terminations. This technique, when applied to modeling performed with commercial codes, provides an efficient alternative when straightforward analytic methods are not available. Once propagation characteristics have been calculated, TL equations can be implemented in the hybrid approach and subsequently applied to optimization procedures. The remainder of the chapter will concentrate on examples where the hybrid approach was applied.

2.2.1 Initial Examples

Ultimately, it is desired to model and optimize full-scale mines with the hybrid approach. Before this is done, it is instructive to demonstrate the efficiency and accuracy of the hybrid approach for a less complex geometry. The initial example considered demonstrates the accurate modeling of a TL T-intersection in free space, where Fig. 2.4 details the geometry that was used. A 1-W ideal power source, operating at 500 kHz (free space wavelength, $\lambda_0 \approx 600$ m) was used to feed the network. The twin-lead TLs were assigned a separation distance of 2 m and wire radius of 1 mm ($Z_0 = 911 \Omega$). Each branch of the T-intersection was chosen to be 500 m long and was terminated with a load Z , which for TL analysis was chosen to be open, shorted, and matched. As shown in Fig. 2.4, three different hybrid models, Hybrids 1, 2, and 3, were considered and corresponded to utilizing ideal TL sections that were 100 m, 300 m, and 400 m long, respectively. The three hybrid models and the original full-wave model were compared in order to demonstrate the accuracy and increasingly reduced computational demands of the hybrid approach when larger and larger ideal TL sections were utilized, which effectively reduced the size of matrices used in MoM calculations. Figure 2.5 compares the calculated current profiles of the full-wave and hybrid models along the X and Y axis-aligned branches. The current calculations, which were normalized to the source current, indicate that the hybrid approach agreed well with its full-wave counterpart. Note that where current values have been omitted indicates the location of the analytic ideal TL sections. Finally, using an 8-core Intel E5620, hybrid models 1, 2, and 3 reduced simulation times approximately 4, 20, and 80 times, respectively, compared to the equivalent full-wave model.

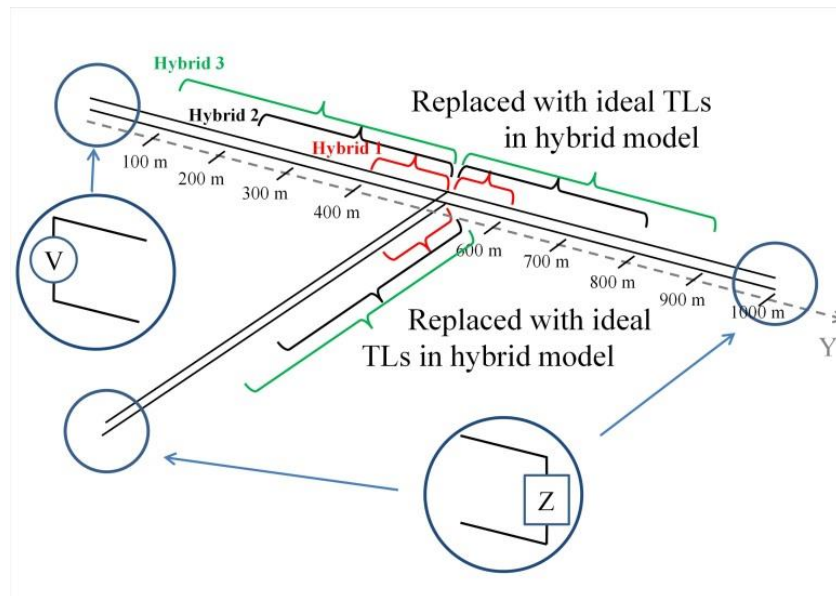


Figure 2.4. Geometry of a T-intersection full-wave and hybrid model comparison using open, shorted, and matched terminations.

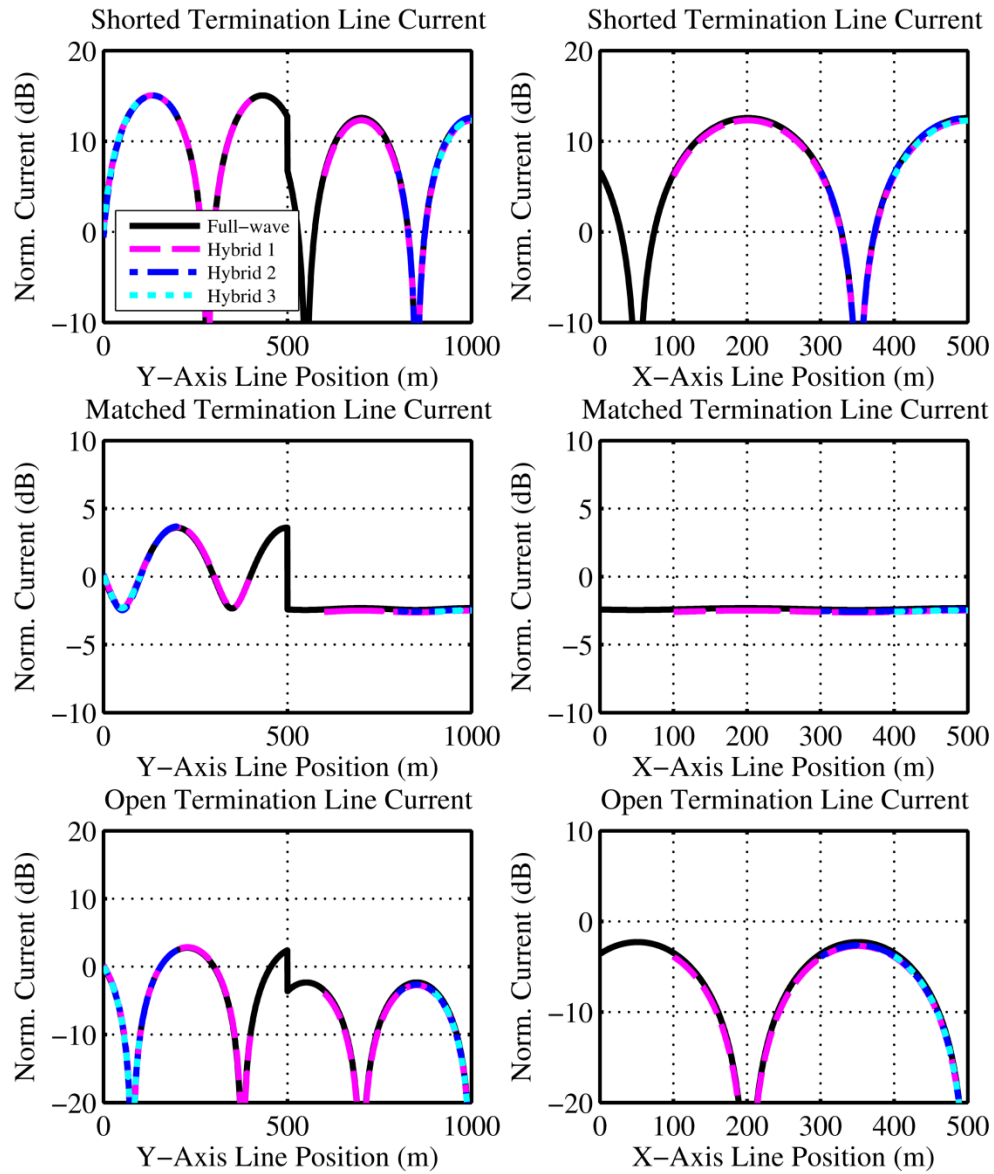


Figure 2.5. Currents calculated using equivalent full-wave and hybrid models. The calculated current magnitudes were normalized to the source current.

In the previous example, the computational time required by the hybrid model depended only on the size of full-wave sections used for the source and load regions. Subsequently, the hybrid approach allows networks to increase in size without discernible change in computational

times, whereas an equivalent full-wave model using MoM would require more computational time and resources as the physical size of the model increases. This makes the hybrid approach attractive for large problems, but also facilitates modeling of full-scale mines whereas using MoM would not be feasible, even with notable computer resources.

In the next example, this fact was exploited and tested. Specifically, a TL $27 \lambda_0$ long at 500 kHz (*i.e.* 16.2 km) was placed between two parallel plates of lossy earth in order to test the hybrid model subject to environmental loading; an important consideration when modeling MF communication networks in coal mines. The TL possessed the same separation and wire radius as in the previous example. A 10-cm radius loop antenna with a wire radius of 1 mm was used for both the transmitting (T_x) and receiving (R_x) antennas. T_x was fed by a 1-W power source operating at 500 kHz. This geometry is illustrated in Fig. 2.6. For this example, the environmentally-loaded TL equations were constructed using moment method models in conjunction with the techniques discussed in [75]. Currents along the full-wave section surrounding R_x were calculated for shorted and open terminations and are compared for the hybrid and full-wave models in Fig. 2.7. This example clearly demonstrates the accuracy of the hybrid approach, even over very large distances of propagation. Because of this large distance, computational times for the full-wave and hybrid models were 5,540 seconds and 6.9 seconds, respectively, on an 8-core Intel E5630. This equated to a factor of 800 reduction in computation time.

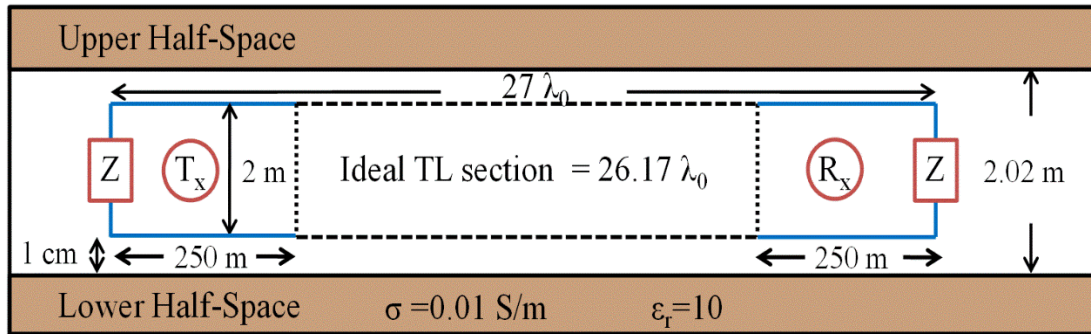


Figure 2.6. Geometry of a $27 \lambda_0$ long TL (*i.e.* 16.2 km) placed between two parallel boundaries of lossy earth used to test the hybrid model subject to environmental loading.

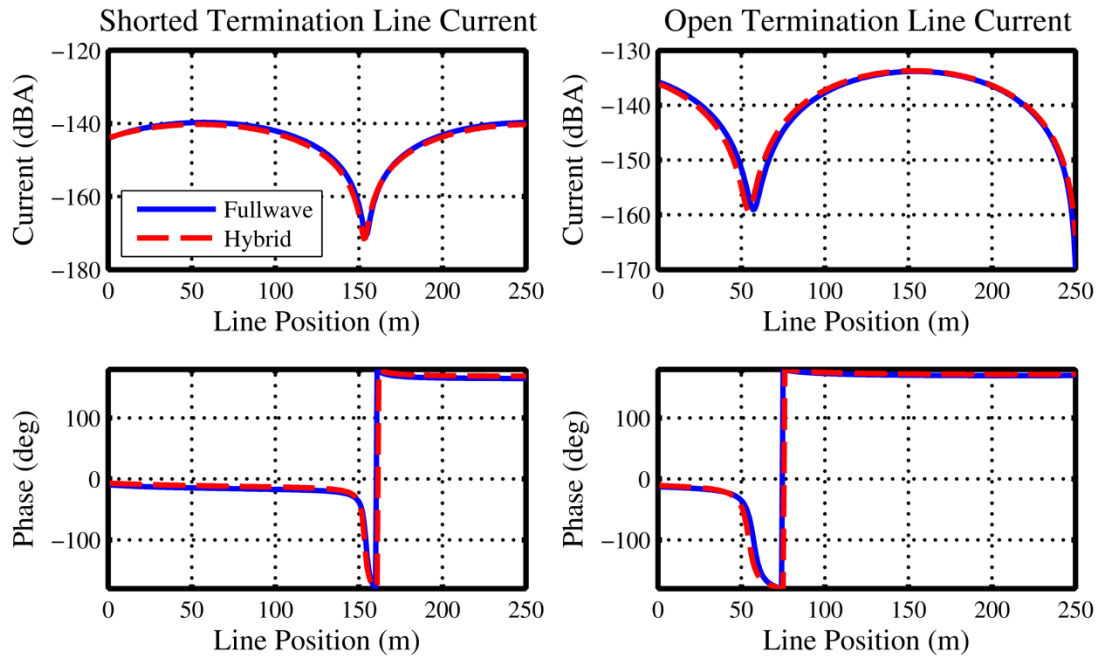


Figure 2.7. Current magnitudes and phases calculated on the R_x TL section were compared between full-wave and hybrid models for shorted and open terminations.

2.2.2 Propagation with an Earth Return

In order to account for the various possible MF propagation modes in coal mines, it is also important to consider those which use the surrounding earth material as a current path. This

may occur when either a multiple wire system is experiencing CM propagation or a single wire conductor is placed within the coal mine tunnel. In the following sections, the modeling of a single wire conductor placed close (*i.e.* much less than one wavelength) to a lossy earth material is considered. This geometry, as shown in Fig. 2.8, can equivalently represent multiple wire conductors facilitating in-phase propagation (CM propagation) and subsequently using the earth as the current return path. As predicted in the literature [86, 88, 89], at MF a quasi-TEM mode is readily established between a single conductor and earth material return path. Because of this characteristic, the modeling of a conductor positioned near a single earth layer should be a good approximation to an identical conductor placed nearest to one (out of four) of the boundaries within a mine tunnel (more on this and its importance shortly). This is a reasonable application since, in practice, conductors would usually be supported by ceilings or floors. As will be shown, with this approximation the TL analysis is significantly simplified. However, it is worth noting that this approximation may not hold as well when the conductor is placed in a corner of the tunnel cross section, effectively placing it close to two intersecting earth surfaces. Developing accurate and efficient models for this scenario is a topic of future consideration.

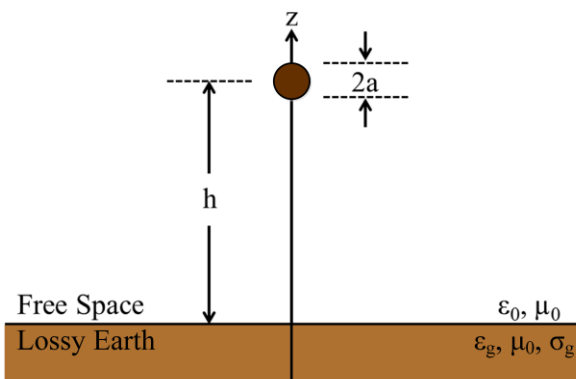


Figure 2.8. Geometry of single wire above lossy earth and free space boundary.

Propagation with earth return has been a topic of interest for almost a century. First

reported in 1926, Carson [89] derived approximate TL solutions under the assumption that the wires are thin, placed in close proximity to the ground, and that the ground return dissipation factor is characteristic of good conductors (*i.e.* $\sigma/\epsilon\omega \gg 1$). In effect, Carson's approximation provides straightforward calculations, but requires low frequencies of operation and/or the return path to have high conductivity, which may not be the case for all mine materials of interest. Significant improvement was made in 1972, when J. R. Wait's analysis [86] provided the exact modal equation for all ranges of both electrical and geometric parameters. Wait's model showed that the propagation constant, $j\gamma$, could be written in terms of the standard TL modal equation given by

$$j\gamma = \sqrt{ZY}, \quad (2.4)$$

where Z and Y are the equivalent series impedance and shunt admittance, respectively, and are functions of γ .

The difficulty with Wait's approach is that γ is a function of itself and therefore requires advanced numerical methods to compute solutions in all but the simplest cases. To avoid the challenges associated with solving the exact modal equation and obtain intuition for the system, attempts to improve on Carson's original approximation have been reported which introduce corrective terms that account for displacement currents associated with lossy dielectrics. The approximation used here was reported in 1996 by D'Amore and Sarto [88]. The derivation assumes a thin wire diameter and wire heights that are much smaller than one wavelength (*i.e.* $a \ll \lambda$ and $h \ll \lambda$ in Fig. 2.8, respectively). With these assumptions, the approximate form of the propagation constant in (2.4) is given by

$$\gamma^2 \approx k_0^2 \left(\frac{\frac{2\pi Z_{\text{int}}}{j\omega\mu_0} + \ln\left(\frac{2h}{a}\right) + 2S_1(h)}{\ln\left(\frac{2h}{a}\right) + S_2(h)} \right), \quad (2.5)$$

where Z_{int} is the wire's internal impedance, while S_1 and S_2 are the small argument, logarithmic approximations for the associated Sommerfeld integrals given by

$$S_1(h) = \frac{1}{2} \ln(1 + \alpha r^{-1}) \quad (2.6)$$

and

$$S_2(h) = \frac{k_0^2}{k_g^2 + k_0^2} \ln(1 + \beta r^{-1}) \quad (2.7)$$

Here, jk_0 and jk_g are the propagation constants of unbounded electromagnetic waves in the free space and ground media, respectively. Lastly, $r = (4h^2 + a^2)^{1/2}$ where h is the distance from the earth/free space boundary to the center of a wire conductor with radius a , shown in Fig. 2.8. The α and β terms are defined by

$$\alpha = \frac{2}{\sqrt{k_0^2 - k_g^2}} \quad (2.8)$$

$$\beta = \frac{k_0^2 + k_g^2}{k_0^2 \sqrt{k_0^2 - k_g^2}}. \quad (2.9)$$

Note that the propagation constant, γ , is no longer a function of itself, making subsequent transmission line equations in the hybrid approach a straightforward task. When compared with Wait's exact modal equation (2.4), this approximation is remarkably simple to use, so long as the appropriate limiting conditions are met, providing an accurate means to perform rapid computations of the propagation constant and characteristic impedance.

2.2.3 Hybrid Approach for a Wire with Earth Return

Next, a hybrid model was constructed using the D'Amore approximation outlined in the previous subsection. The example considered was a wire placed 20 cm above an earth/air

interface. The lossy earth return was assigned material parameters of $\sigma = 0.01$ S/m and $\epsilon = 10$. The 5-km-long copper wire had a 1-mm radius and was terminated into the ground, normal to the air/earth surface boundary. The grounding rod was 1.5 m long and had a radius of 1 mm. At one end of the TL there was an ideal voltage source operating at 500 kHz. At the opposite end there was a load Z . The corresponding geometry is illustrated in Fig. 2.9. In this hybrid model, a 4.4-km-long section between the source and load was replaced by TL equations constructed using the D'Amore approximation. Effectively, these TL equations were used to properly load the source section and excite the load section. Line currents were calculated and are compared in Fig. 2.10 for the load Z designated to be both an open and a short. It is extremely important to note that there was an additional resistance associated with the grounding rod geometry (*i.e.* length and diameter) beneath the earth's surface, which can be seen from the reduced SWR of the so-called shorted currents. To account for this in the hybrid model, the resistance was approximated using the low-frequency, power system equations for grounding rod resistance discussed in [90], which is given by

$$R_{term} = \frac{1}{2\pi\sigma l} \log\left(\frac{2l}{a}\right) \quad (2.10)$$

where σ is the ground conductivity, l is the length of the grounding rod, and a is the radius of the grounding rod. It is important to note that this equation assumes the earth material surrounding the grounding rod is characteristic of a good conductor. This is often the case for MF propagation in coal mines; however, an alternative approach would be required for low conductivity earth materials.

The current calculations in Fig. 2.10 indicate only a small current error between the hybrid and full-wave models—approximately an error of 2 dB and 15 degrees in phase. Again note that the omission of currents in the hybrid model indicates where TL equations have been applied. The good agreement of current calculations for both termination types further indicates

the accuracy of the D'Amore approximation for these geometries when excited with MF. Furthermore, using an 8-core Intel E5620, the hybrid models were simulated in 7.4 seconds. The full-wave counterpart was completed in 440 seconds which corresponded to a factor of 60 reduction in computation time.

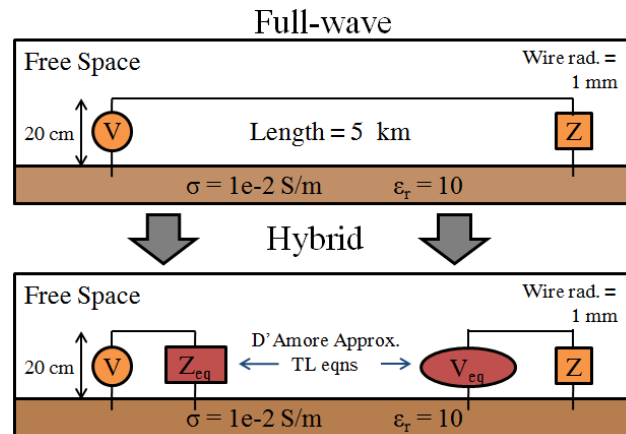


Figure 2.9. Geometry: 1-mm radius wire placed 20 cm above lossy earth return.

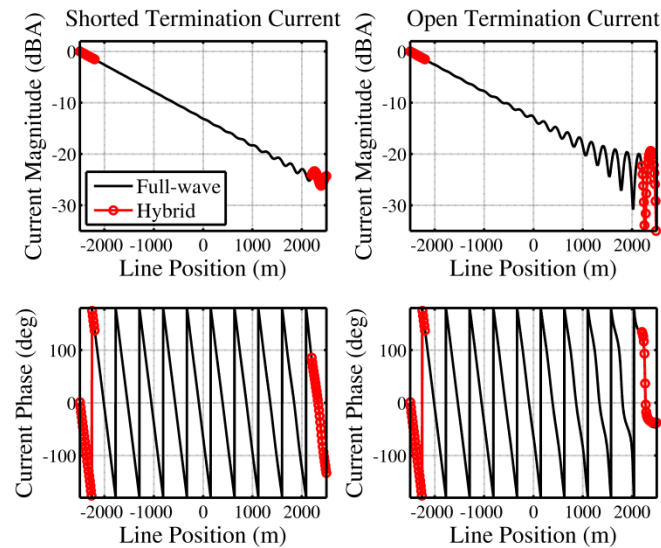


Figure 2.10. Currents for full-wave and hybrid models were calculated and are compared for both shorted and open terminations.

As was previously suggested, the D'Amore approximation can be effectively utilized due to the TEM nature of MF waves in coal mines, where most of the electromagnetic energy is

confined between the wire conductor(s) and the nearest tunnel boundaries. The next example considered employing the hybrid technique to support this argument. In this example, we made use of the fact that if a wire conductor is positioned closer to one tunnel boundary than the others, such as is shown in Fig. 2.11b, then the electromagnetic environment should be approximately equivalent to that shown in Fig. 2.11a, which is the geometry that was just previously considered for a hybrid model.

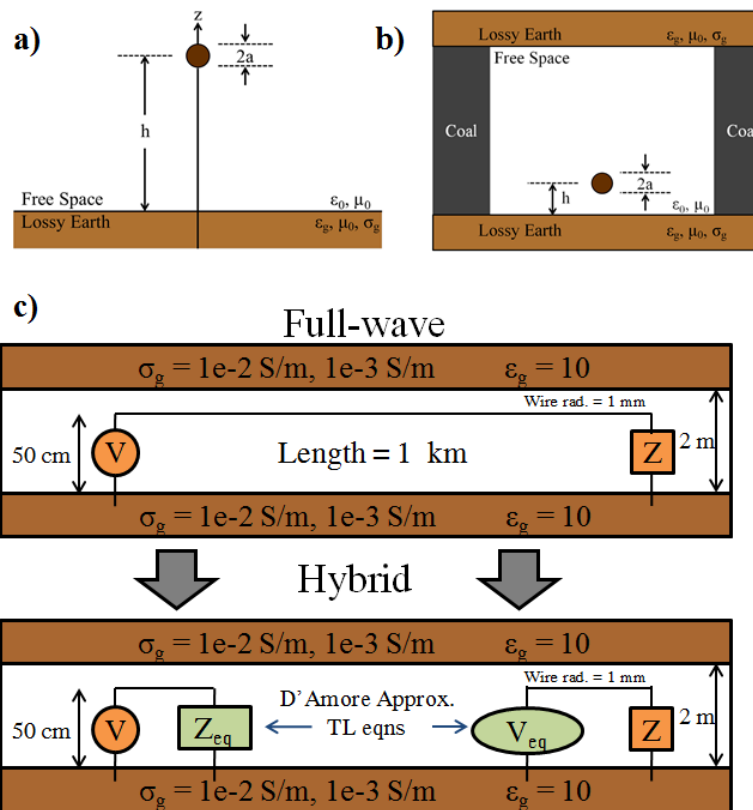


Figure 2.11. (a) Geometry: wire placed above a lossy earth return. (b) Geometry: wire placed above a mine tunnel floor. (c) Side-view of mine tunnel hybrid model with a wire positioned 50 cm above a mine floor.

In the next example, a 1 km long wire conductor was positioned 50 cm above a mine tunnel floor. The tunnel cross section was assigned typical coal mine dimensions with a height of 2 m and a width of 6 m; however, due to the approximation used here, these dimensions were not

expected to greatly affect the propagation characteristics. That is, only the mine floor material parameters and distance the wire was positioned from that surface would dictate the electromagnetic properties of the TL. An ideal voltage source operating at 500 kHz was positioned opposite to either a short or open termination. This geometry is illustrated in Fig. 2.11c. Currents for the hybrid and full-wave models were calculated for both termination types and two different mine floor conductivities ($\epsilon_g = 10$): $\sigma_g = 1e-2$ S/m and $1e-3$ S/m. The corresponding currents that were calculated are compared in Fig. 2.12. There was some disagreement in the calculated currents, likely due to additional loading from the other tunnel boundaries; however, overall the results demonstrate the accuracy of the hybrid approach for mine tunnels where a single conductor is placed close to one of the boundaries. Again, it is important to note that this assumption will need further consideration and revision in geometries where the wire conductor is placed equally close to two intersecting surfaces. Furthermore, to add complexity to the system, the coal seam (*i.e.* tunnel walls) and conductive rock layers (*i.e.* ceiling and floor) generally have conductivities that differ by one to several orders of magnitude [66]. This is a topic to be considered in future work, but remember it is always possible to construct accurate TL models by applying the techniques formulated in [75] to representative full-wave models. This is what was done in the example previously presented which considered the environmentally-loaded TL placed between two lossy earth boundaries. To conclude this example with calculation time comparisons, the full-wave and hybrid models were simulated in 3,800 seconds and 720 seconds, respectively, on an 12-core Intel E5645. This equated to a factor of 5.2 reduction in the computation time. It is very important to note that for this example, the memory requirements were 37.7 GB and 4.6 GB for the full-wave and hybrid models, respectively. Hence, for typical computers, the coal mine tunnel length is very limited using full-wave techniques alone; only the hybrid approach can allow for substantial line lengths required to model large-scale coal mine communication networks. Furthermore, optimizing such networks without the

hybrid method would be infeasible all together.

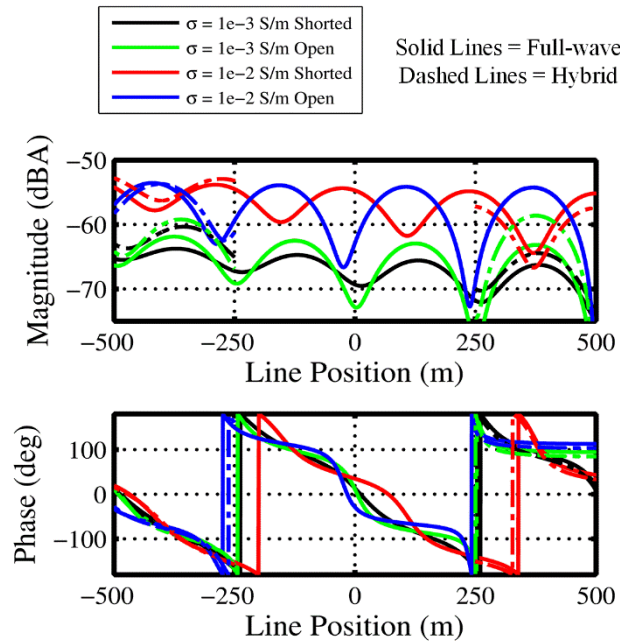


Figure 2.12. Currents for full-wave and hybrid models were calculated and are compared for both shorted and open terminations and two different return path conductivities.

2.2.3 Large-scale Optimizations using the Hybrid Approach

As previously mentioned, the main motivation behind the hybrid approach was to facilitate large-scale optimizations of coal mine communication networks that would otherwise be very challenging due to the limited analytic solutions or the large computational cost of full-wave (MoM) computer models. With the previous examples establishing the basic tools for constructing communication networks with the hybrid approach, two final, optimization examples were formulated and are presented next.

The first example optimized power transfer from a single transmitter to three receivers through a large TL network placed in free space. Each segment of the TL network was 240 m long. Each antenna had a 10-cm diameter and a 1-W power source operating at 500 kHz. A

binary genetic algorithm (GA) was used to maximize power transfer by choosing whether an open or short (*i.e.* one or zero bit) should be placed at each node and end termination. The goal of power maximization was achieved by implementing the following cost function:

$$\text{cost} = \sum_i |10 \log_{10}(P_i)| \quad (2.11)$$

where i represents each receiving antenna and absolute values were imposed because evolutionary algorithms traditionally try to minimize cost. Each iteration of the optimization using the hybrid model required only 7.9 seconds on an 8-core Intel E5620. In comparison, the full-wave counterpart required 356 seconds, a runtime factor difference of about 45. To fully appreciate this time difference, consider that this example was converged by generation 25 using a population of 20. Hence, totaling 500 iterations for convergence, the hybrid approach required about 1 hour whereas optimizations employing the full-wave models would require approximately 2 days. The optimal solution is shown pictorially in Fig. 2.13 where unfilled and filled circles represent open and shorted terminations, respectively. The hybrid model calculated power transfer from T_x to be -156.3 dB, -148.9 dB, and -157.4 dB to R_{x1} , R_{x2} , and R_{x3} , respectively. Using the same terminations in an equivalent full-wave model, the calculated power transfer was determined to be -156.3 dB, -148.6 dB, and -157.4 dB to R_{x1} , R_{x2} , and R_{x3} , respectively. Hence, even for a large communication network, the hybrid model produces extremely accurate results.

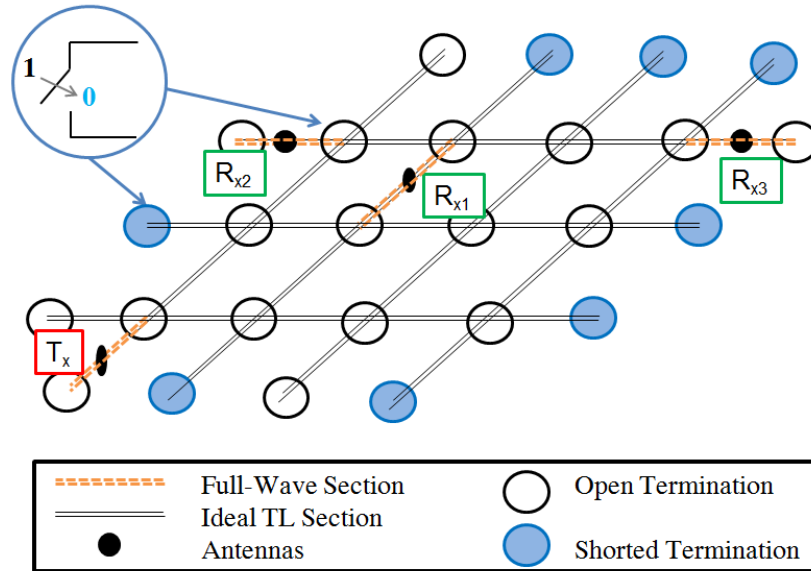


Figure 2.13. Large TL network used to demonstrate the feasibility of performing large-scale optimizations by utilizing the hybrid approach. The optimization protocol was to simultaneously maximize power transfer from T_x to three different receivers by implementing open and shorted terminations at each node and endload.

The second and final example optimized a communication network similar to what could be used within a room-and-pillar mine architecture such as the one shown in Fig. 2.14. To simplify the problem, conductors were placed much closer to the floor than to other surfaces, such as the coal pillars and ceiling, allowing the system to be approximated as if only the floor were present.

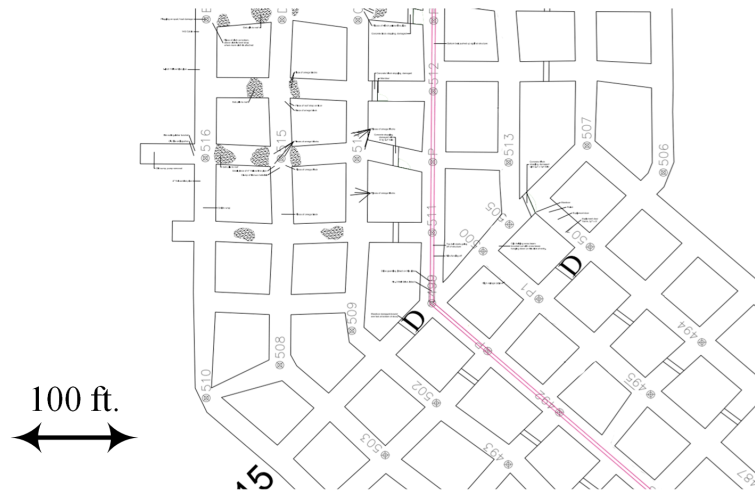


Figure 2.14. Map of mining area showing room-and-pillar layout.

The communication network used for optimization is shown in Fig. 2.15, which illustrates the top view of a series of single conductor interconnects that use the earth as a return path. The lossy earth layer was assigned material properties $\sigma = 0.01$ S/m and $\epsilon = 10$. All copper wires were positioned 20 cm offset from the air/earth interface. In this example, SWR was minimized by apply the CMA-ES to the cost function,

$$\text{cost} = \sum_i \frac{\max |I_j|}{\min |I_j|} \quad (2.12)$$

where I_j are the currents on the wire sections closest to the transmitting and receiving antennas, which are represented by orange-dashed lines in Fig 2.15. This was accomplished by simply extracting the calculated currents along the full-wave sections from the simulation output files. Subsequently the corresponding SWR values were calculated and used as a feedback mechanism for CMA-ES. Network tuning was accomplished by varying the distance that the grounding rods penetrated into the ground (*i.e.* grounding rod length) at the end of each TL section, which

effectively varied their individual termination resistances. The geometries of the transmitting antenna and two receiver antennas were identical: 10-cm loop antennas with 1-mm radius wire. To excite the network, T_x was fed by a 1-W ideal power source operating at 500 kHz. Only the 200-m full-wave sections nearest to the antennas were left in the hybrid model. Figure 2.16 compares the currents calculated in the optimized hybrid model and the equivalent full-wave model. All currents were normalized to the source current on T_x in order to indicate overall power transfer from T_x to R_{x1} and R_{x2} . The agreement between currents was extremely good considering the beneficial improvement in computational speed. The full-wave models required 1,157 seconds to simulate on an 8-core Intel E5620. On the same machine, the hybrid model required only 10.7 seconds, providing a runtime reduction factor of 110.

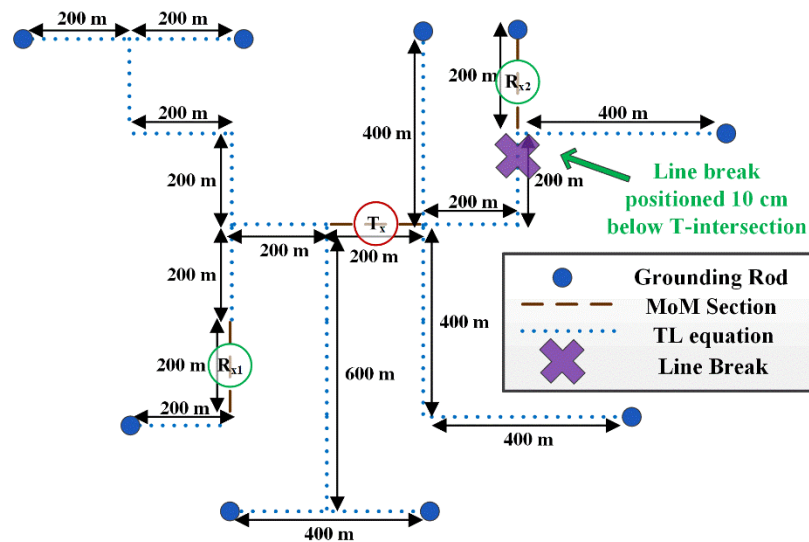


Figure 2.15. Geometry for optimization problem using the hybrid approach. A network of single conductors is constructed and optimized for minimum SWR on the segments nearest to the transmitter and receiving antennas. Optimization is performed by varying the length of grounding rods at the end of each open segment.

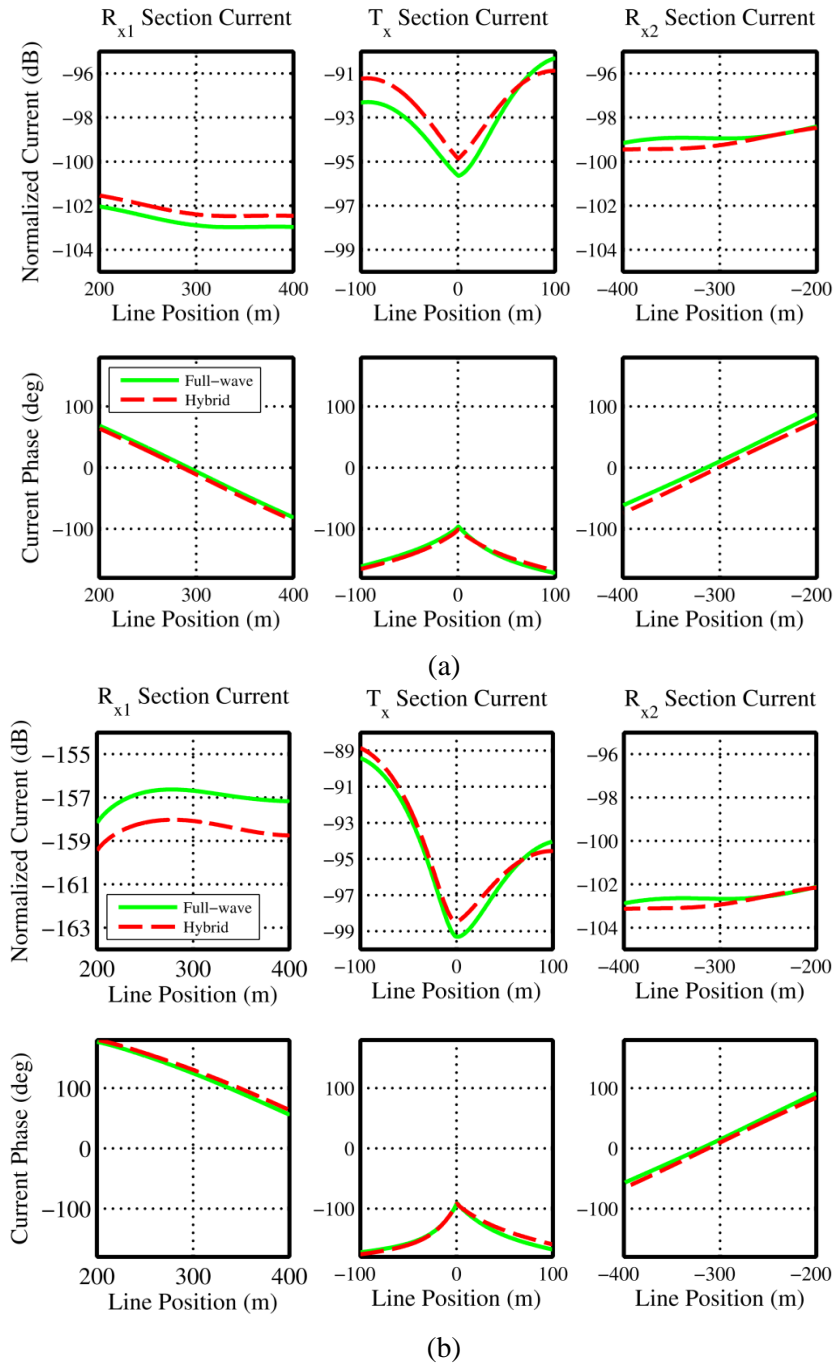


Figure 2.16. (a) Current comparison for optimized hybrid and full-wave models. (b) Current comparison for hybrid and full-wave model after a line break was introduced. The TL section corresponding to R_{x1} is located after the TL break, as is evident in the relatively small current magnitudes.

Lastly, to further demonstrate the power of the hybrid approach, a TL break (1-cm section removed), simulating a mine collapse, was introduced into the communication network, represented by a red “X” in Fig. 2.15. Such an electromagnetic model would not be easily represented using simple TL equations. However, using the hybrid method, a full-wave section introduced to model the line break fully captured the propagation effects and associated power losses. The currents predicted by the hybrid model were calculated and are compared with the equivalent full-wave model in Fig. 2.16. The reliability and versatility of the hybrid approach for near field effects such as line breaks will be crucial for performing parametric studies on communications systems designed for emergency response in coal mines and improved survivability.

2.4 Conclusions

The hybrid approach was shown to significantly improve computational efficiency while simultaneously providing a high degree of precision. First, TLs making a T-intersection placed in free space were verified. Then, geometries that utilize earth materials as a current return path were approximated using D’Amore’s method. From this approximation, appropriate TL equations were implemented into both above earth and coal mine tunnel hybrid models which were validated through comparisons with full-wave simulations. With these basic tools, it was demonstrated that full-scale coal mine communication networks can be constructed and optimized both for daily operations as well as emergency communications and tracking. The combined methods of numerical and analytic modeling with measurements should provide a powerful engineering package for future system design.

Chapter 3

Miniaturized Dual-Band Folded Patch Antenna with Independent Band Control Utilizing an Interdigitated Slot Loading

3.1 Introduction

Notable emphasis has been placed on the miniaturization of antennas for mobile and wireless communications [91, 92]. Microstrip patch antennas are particularly attractive candidates due to their low profile and low fabrication cost [93]. However, a conventional patch antenna has an electrical length of $\sim\lambda_0/2$, making it too large for many desirable wireless applications. As a result, several design methodologies have been developed to reduce the size of the patch antenna. Typically these techniques utilize some combination of meandering [94, 95], notching [96], shorting [97], folding [98, 99], slit cuts [100], high permittivity substrates [101], magneto-dielectric substrate loading [102, 103], and more recently metamaterials [104-106]. Generally speaking, the trade-off cost of employing these size-reducing techniques is manifested in reduced bandwidth, reduced gain, and increased cross-polarization. In addition to size reduction, many wireless systems also benefit from multi-band operation. Several techniques to achieve dual- or multi-band operation with patch antennas have been reported and are often some variation of a stacked patch configuration [107] or those placing slots on the patch surface [108-110].

Employing a composition of the mentioned techniques to both reduce the size of a patch antenna as well as exhibit multi-band operation creates the possibility of developing design methodologies for reducing the size of multi-band patch antennas [111-118]. For example, a shorting wall can be applied to a dual-resonant stacked patch configuration [111], reducing the antenna size by a factor of around two. The shorting wall can also be applied to a slotted patch antenna [112]. Further size reduction can be achieved by reducing the width of the shorting plane. In [113, 114], a folding technique was applied to miniaturize a shorted slotted patch (SSP) antenna

and a patch antenna with a U-slot, respectively. Yet, in all four cases the lateral size of the resulting antenna elements was greater than $0.1\lambda_0$. Furthermore, the corresponding radiation patterns increasingly deteriorated with decreasing antenna size, exhibiting asymmetric radiation properties (*i.e.* beam squinting), in some cases with additional beam splitting, and high levels of cross-polarization. In [115, 116], additional slots were added to the patch surfaces, perturbing the current path and shifting the resonant conditions to lower frequencies. However, again there was no clear path for antenna element size smaller than $0.1\lambda_0$ using a single feeding method. A similar meandered patch surface approach combined with folding and shorting was considered in [117] where a small (*i.e.* $<0.1\lambda_0$) element and a small footprint were achieved, however high cross-polarization was exhibited in addition to pattern asymmetry at the second resonant frequency. In [118], a multiband antenna with size approaching $\leq 0.1\lambda_0$ for mobile applications was presented, but required a complex PIFA antenna geometry utilizing a combination of slot, capacitive, and shorting loads.

This chapter demonstrates a miniaturized linearly-polarized dual-band folded patch antenna loaded by an interdigitated slot. All antenna dimensions are $\leq 0.1\lambda_0$, which also facilitates the use of a small, $0.3\lambda_0$, square ground plane, providing a notably small antenna footprint. Here, λ_0 refers to the free space wavelength under TM_{10} operation. In sub-section 3.2, the antenna design procedure is presented, with emphasis on miniaturization. To demonstrate and verify the proposed design procedure, 2.4 GHz and 5.0 GHz were targeted for prototype fabrication and testing. In sub-section 3.2.1, several fabrication considerations are incorporated into the simulation models, from which the antenna performance is predicted. Furthermore, by analyzing the currents circulating the interdigitated slot it is revealed that the current distributions at each operational frequency band were swapped relative to those shown in [108]. Subsequently, this phenomenon is used to help explain the antenna miniaturization achieved. Then, fabrication and characterization of the proposed antenna element is presented in sub-section 3.2.2. Measurements of antenna input

impedance, radiation pattern, and broadside realized gain are presented and compared with simulation predictions. In section 3.3, a sensitivity analysis was numerically performed on the antenna element, providing a physical insight into its performance and, specifically, how the interdigitated slot dictates the antenna performance. This analysis inspired a straightforward means for independently controlling the two operating bands. The impact of using a small ground plane is section 3.4. Finally, the conclusions are provided in section 3.5.

3.2 Miniaturized WiFi Antenna Utilizing an Interdigitated Slot Loading

To obtain a single-layer dual-frequency patch antenna, a pair of transverse slots positioned near the radiating edges can be added to a conventional patch antenna surface [108]. The two operational modes of the slotted patch antenna, which are TM_{10} and TM_{30} , have a zero potential at the center plane (y - z plane) of the patch [112]. Hence, a short can be implemented in this plane, resulting in an SSP antenna with its length reduced by a factor of ~ 2 . In addition to reduced gain pattern asymmetry, the SSP antenna will exhibit an increased level of cross-polarization, particularly in the H -plane.

Next, based on the SSP antenna, further reducing the width of the slotted patch is considered. First, it is known that the dual-band frequency ratio is determined by the slot lengths [108]. Therefore, the width of the patch and slot is fixed by the targeted frequencies, presenting a challenge for further patch size reduction. This limitation can be partially mitigated by controlling the width of the shorting-plane, which further reduces both resonant frequencies [112]. However, even with this modification the width of the patch still restricts the antenna size to be larger than $0.1\lambda_0$. To overcome this constraint we propose to replace the straight slot with an interdigitated slot, creating a longer path for the perimeter currents and allowing for a reduced patch width. Furthermore, the interdigitated slot has more variability than a straight slot, providing additional

degrees of freedom for the resulting frequency ratio and, as will be demonstrated, the independent control of each operational band. Next, the antenna element was further reduced by folding the shorted patch antenna [98]. The resulting antenna element is a folded SSP antenna, which was discussed in [113] for improved impedance bandwidth. Then, when the folded SSP antenna is combined with the proposed interdigitated slot loading as a technique to reduce the width of the patch, there is then a basis for reducing the overall footprint of the dual-band patch antenna. The resulting antenna geometry is shown in Fig. 3.1. This design procedure was originally proposed in [119] for ISM applications, but a detailed analysis on how the interdigitated slot aids in element miniaturization has not yet been reported. Additionally, utilizing the interdigitated slot for independently controlling the two operational bands has not yet been investigated. Both topics are discussed in the following sections.

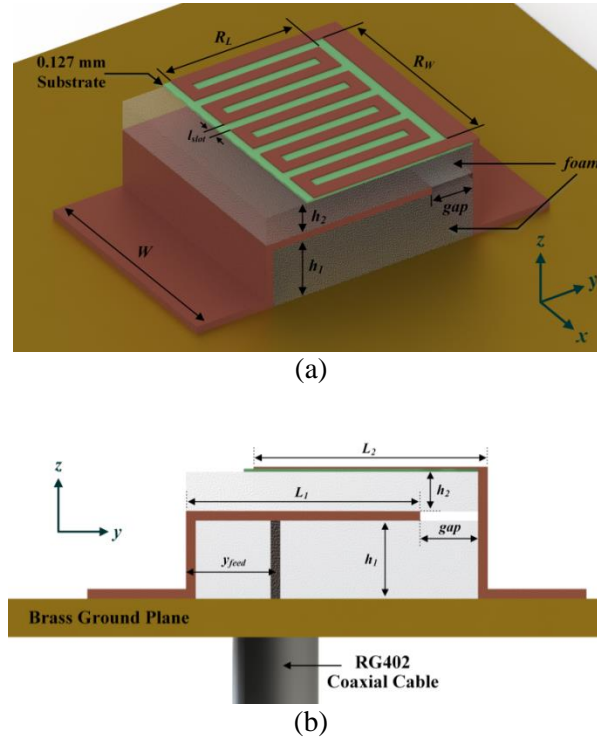


Figure 3.1. Configuration of the proposed antenna structure: (a) perspective and (b) side geometric views.

TABLE 3.1
ANTENNA GEOMETRY

Parameter	Optimized Value (mm)	Fabricated Value (mm)
L_1	9.50	9.50
L_2	9.50	9.50
W	12.48	12.70
gap	2.73	2.31
R_L	$0.80*L_2$	$0.80*L_2$
R_W	$0.87*W$	$0.87*W$
h_1	3.18	3.22
h_2	1.59	1.65
l_{slot}	0.60	0.60
y_{feed}	$0.34*L_1$	$0.34*L_1$

The values that were revised for the simulation model labeled “Fabricated Value (mm)” are bolded (blue).

3.2.1 Fabrication Consideration and Simulation Results

In order to ensure high fidelity prototype manufacturing, refinements were made to the proposed antenna design. First, the metal patch sections were easiest to bend and form without substrates. However, in order to provide structural support, a 4 lbs/ft³ 1/16-inch-thick polyethylene foam layer (modeled as $\epsilon_r = 1.07$) was inserted between patch layers. These layers, with thicknesses h_1 and h_2 , were then restricted to discrete multiples of available foam sheet thicknesses. Additionally, to create a precise interdigitated slot pattern, chemical etching was performed on a 0.127-mm-thick Rogers Duroid 5580 substrate. The number of meander turns was chosen to ensure a high fidelity pattern, based on limiting the patch width to $0.1\lambda_0$ at 2.4 GHz and the feature size capabilities of the chemical etching technique. A meander composed of five back-and-forth segments with traces approximately as wide as the spacing between the adjacent traces was adopted, providing a feature size of ~0.5 mm. Next, R_w was constrained to stretch nearly the width of the patch in order to achieve radiation patterns maximum at broadside [108].

Next, in order to maintain a compact total antenna footprint, a 0.062-inch-thick brass square ground plane only $0.3\lambda_0$ at 2.4 GHz (≈ 3.75 cm) on an edge was used. The affect of utilizing a small ground plane, namely strong diffraction contributing to the overall radiation properties [120], was investigated and will be presented in a Section 3.4. With these fabrication-inspired revisions implemented to the antenna geometry shown in Fig. 3.1, we employed the CMA-ES to fine-tune the critical dimensions of the antenna element for achieving impedance matching and maximum broadside gain at 2.4 GHz and 5.0 GHz. A high frequency structure solver (HFSS) was employed to calculate the input impedance and radiation properties of the antenna structure. The optimized geometry is given in Table 3.1, column 2. The fabricated device is shown in Fig. 3.2.



Figure 3.2. Fabricated antenna used for validation. (Left) shows a perspective view of antenna with foam inserts and (right) shows a side view of antenna without foam inserts.

Before presenting the predicted antenna input impedance and radiation patterns, it is instructive to more thoroughly consider how the interdigitated slot aids in miniaturizing the antenna element. To do this, the surface currents around the slot of the optimized design were analyzed at both operational modes. The resulting current distributions are shown in Fig. 3.3. When compared to those presented in [108] it is apparent that the current patterns of the two operational modes have swapped. That is, the currents circulating the interdigitated slot under TM_{10} operation resemble the currents around the conventional slot under TM_{30} operation.

Likewise, here the currents under TM_{30} operation instead resemble the circulating currents of TM_{10} of the conventional slotted patch antenna. Now, in [108] it was shown that the resonant condition of the TM_{30} is primarily dependent on the geometry of the slot and not, for example, the overall length of the patch. Conversely, the TM_{10} mode resonant condition did depend on the length of the patch, similar to a conventional patch antenna. As a result, the size of the slotted patch antenna was more-or-less fixed by the wavelength of the TM_{10} mode. In contrast, here the TM_{10} resonant condition is dependent primarily on the interdigitated slot geometry and because the interdigitated slot more efficiently uses the patch surface, there is a notable avenue for antenna miniaturization. It is worth pointing out that this analysis does not necessarily guarantee good radiation properties; hence, the following paragraph presents the predicted antenna input impedance and radiation characteristics.

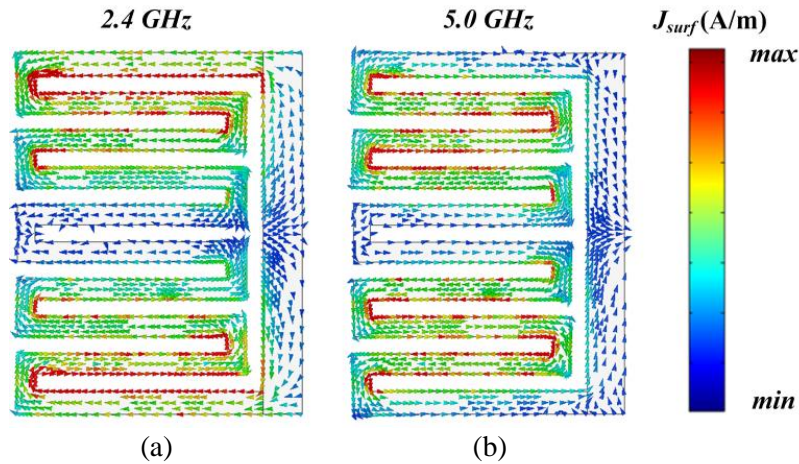


Figure 3.3. (a) Surface currents around the interdigitated slot at 2.4 GHz and (b) 5.0 GHz. The arrows' colors and direction represent the current magnitude and phase, respectively.

The simulated S_{11} is shown in Fig. 3.4. The -10 dB impedance bandwidths were predicted to be 25 MHz and 125 MHz at the 2.4 GHz and 5.0 GHz bands, respectively, which are sufficient for at least one WiFi channel in each band. Because we used a small ground plane, it was important to consider the impact of the long coaxial cable. The coax employed to feed the antenna

element was a 12.7-cm-long semi-rigid RG402 coaxial cable. This relatively long feed was not considered during optimization of the antenna element since it would dramatically increase the size of the simulation domain. Instead, the coaxial waveguide considered during optimization was only 3 mm long. It was found that when coupled with the small ground plane, differing coax lengths did not affect the input impedance of the antenna element. However, some change was predicted in the radiation pattern. The most significant differences were seen in the cross-polarization. The radiation patterns, with the long coax taken into consideration, were calculated and are shown in Fig. 3.5. The antenna broadside gain was predicted to be 3.3 dBi and 5.5 dBi at 2.4 GHz and 5.0 GHz, respectively.

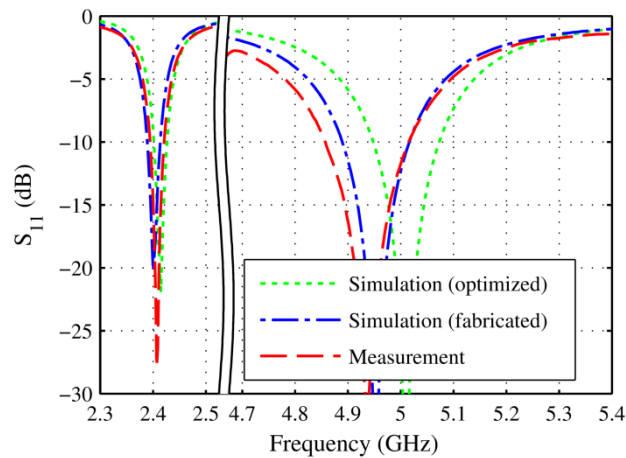


Figure 3.4. Simulated and measured S_{11} of the antenna.

3.2.2 Experiments

The antenna prototype fabricated to verify the design procedure and corresponding simulation predictions is shown in Fig. 3.2. The input impedance of the fabricated antenna was measured by an Agilent E8364B network analyzer. Figure 3.4 compares the simulated S_{11} with measurement. Although the initial comparison was sufficient, there was a slight frequency shift of about 70 MHz at 5.0 GHz. Hence, to further improve the agreement, the fabricated antenna

dimensions were measured and the simulation model was modified accordingly by properly changing the values of the parameters W , gap , h_1 , and h_2 to those given in Table 3.1, column 3. The largest fabrication error pertained to gap , which indeed was the most difficult feature to control when assembling the antenna by hand. Fortunately, as will be discussed in sub-section 3.3.1, this error in gap has a relatively small effect on the resulting antenna performance. The individual effects of each parameter are discussed in more detail in sub-section 3.3.1. Figure 3.4 displays the revised simulation model's reflection coefficient, showing improved agreement with measurements. Next, simulated and measured radiation patterns were compared, as shown in Fig. 3.5. Excellent agreement was found in both the co-polarized and cross-polarized patterns. Finally, the broadside realized gain was measured at 2.1 dBi and 5.3 dBi at 2.4 GHz and 5.0 GHz, respectively. Broadside realized gain measurements are compared with simulations in Fig. 3.6. Some of the gain discrepancies may be attributable to losses in the constitutive materials and solder, particularly for TM_{10} , where the interdigitated slot is resonating. Additional discrepancies may be due to non-ideal experiments, such as imperfect alignment of reference horns.

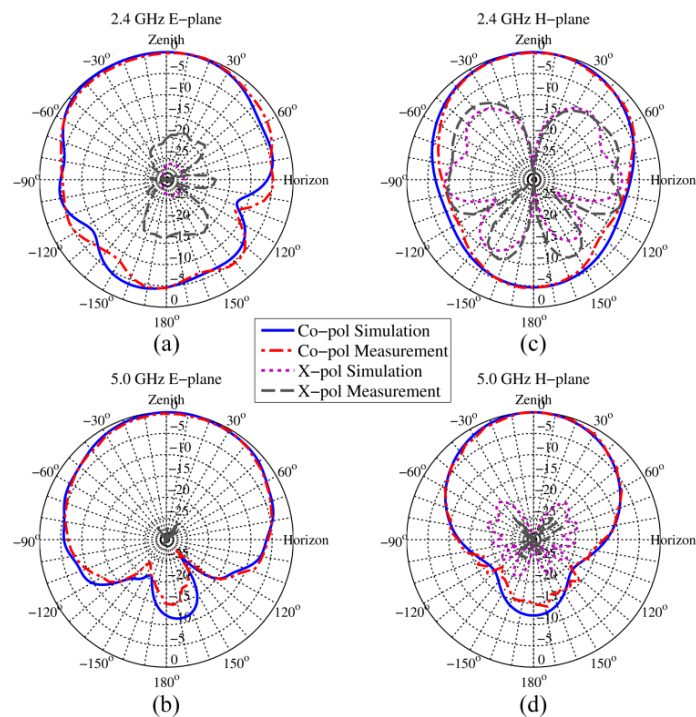


Figure 3.5. (a) Simulated and measured normalized radiation patterns of antenna element in the E -plane at 2.4 GHz and (b) 5.0 GHz. (c) Simulated and measured normalized radiation patterns of the antenna element in the H -plane at 2.4 GHz and (d) 5.0 GHz.

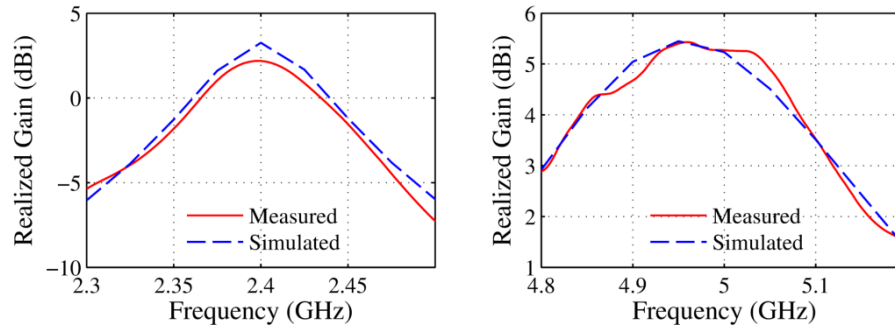


Figure 3.6. Simulated and measured broadside realized gains of antenna element.

3.3 Independent Band Control of the Interdigitated Slot Loading

3.3.1 Antenna Performance Sensitivity Analysis

A sensitivity analysis was performed on the antenna design in order to obtain a physical insight into the performance mechanism of the antenna element. This type of sensitivity analysis is also useful when considering manufacturing techniques where there may be trade-offs in fabrication precision and cost. The sensitivity investigation consisted of a sequence of parametric studies where the value of each geometric parameter was offset by $\pm 10\%$ from its nominal value while all other geometric parameters were fixed.

To begin, when the length of the folded antenna section L_f was varied, the relative frequency shift of TM_{30} was more profound than for TM_{10} , as is shown in Fig. 3.7(a). Figure 3.7(b) reveals that the opposite trend is true for a change in W . This corroborates the analysis in sub-section 3.2.1, where the interdigitated slot was shown to have switched the current

distributions with respect to the conventional slotted patch antenna, leading to flip-flopped dependencies on the antenna base and interdigitated slot geometries. Neither parameter change significantly affected the radiation properties of the antenna element. That is, less than a 0.5 dB change from nominal was exhibited in the broadside gain.

Next, when parameters l_{slot} , gap , and y_{feed} were altered by $\pm 10\%$, the resulting antenna performances were nearly unchanged from nominal. This trend for l_{slot} was also predicted in [108], provided that the width of the patch is an order of magnitude larger than the slot width. Under this constraint the slot width makes a weak contribution to the resonance conditions, and therefore a small change in the slot width will be inconsequential. The $\pm 10\%$ change in gap is smaller than $0.01\lambda_0$ at both frequencies. The corresponding frequency shifts were less than 1%. This trend is also supported when inspecting Table 3.1 and Fig. 3.4, where it was evident that the largest fabrication error, approximately 18%, pertained to gap and still the measured antenna performance agreed well with the optimized antenna simulations. The $\pm 10\%$ change in these three parameters also had negligible effects on the resulting radiation patterns.

Next, individual changes in h_1 and h_2 were considered. The results from these two individual parameter sweeps are shown in Fig. 3.8(a) and 3.8(b). Evidently, the two height parameters do not play similar roles in the resulting antenna performance. This is because a change in h_1 corresponds to a different characteristic impedance of the lower patch section, leading to the frequency shifting shown in Fig. 3.8(a). On the other hand, Fig. 3.8(b) suggests that a similar change in h_2 has a comparable, but opposite, shifting effect on the TM_{10} mode, but negligible effect on the TM_{30} mode. This is because h_2 is a property of the interdigitated slot, which, as has been shown, more strongly influences the resonant condition of TM_{10} and has a minor effect on TM_{30} . Less than a 0.5 dB change was exhibited in the broadside gain from nominal.

Finally, the nature of the interdigitated slot load was investigated by considering parameters R_W and R_L . To start, Fig. 3.9(a) shows the effect of varying R_L by $\pm 10\%$. When R_L is increased, the total path of the perimeter slot currents also increases, reducing the resonant frequencies at both bands. This is an important finding because it means that for a given patch length L_2 , R_L should be as large as possible in order to optimally miniaturize the antenna element. Next, R_W was varied and the corresponding antenna performance changes are shown in Fig. 3.9(b). Immediately, it can be noticed that this was the only parameter that distinctly alters the frequency ratio of the two operational bands. For example, increasing R_W shifts the TM_{10} mode down and the TM_{30} mode up whereas every other parameter either exhibited negligible frequency shifting or, with the exception of h_2 , shifted both resonant frequencies simultaneously either up or down. When considering the radiation patterns it was evident that these two parameters also had a substantial affect, particularly on the cross-polarization, which is likely due to the perpendicular currents generated by the meander pattern. The broadside gain of the TM_{10} mode became 3.4 dBi and 2.5 dBi for -10% and +10% changes in R_L , respectively. For the TM_{30} mode the broadside gain was 5.4 dBi and 5.9 dBi for -10% and +10% changes in R_L , respectively. The broadside gain of the TM_{10} mode became 3.4 dBi and 1.5 dBi for -10% and +10% changes in R_W , respectively. For the TM_{30} mode the broadside gain changed negligibly for -10% and +10% changes in R_W . Because of the substantial radiation contribution of the interdigitated slot region, the effect R_L and R_W have on the cross-polarization was also considered. It was found that the maximum cross-polarization of the TM_{10} mode was not significantly affected by the $\pm 10\%$ changes in either parameter. However, a discernible change in cross-polarization was predicted for TM_{30} . Nominally, the antenna design exhibited a maximum cross-polarization of -10.6 dBi. This changed to -13.7 dBi and -7.6 dBi for -10% and +10% changes in R_W , respectively. The change was oppositely trended for R_L ; -10% and +10% corresponded to -7.8 dBi and -12.7 dBi, respectively.

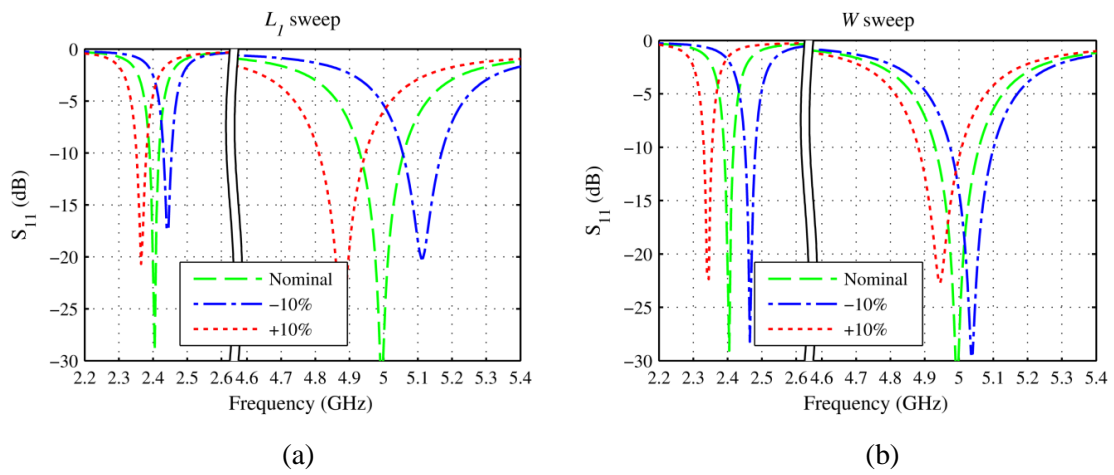


Figure 3.7. Simulated S_{11} of the antenna with varying (a) L_1 and (b) W .

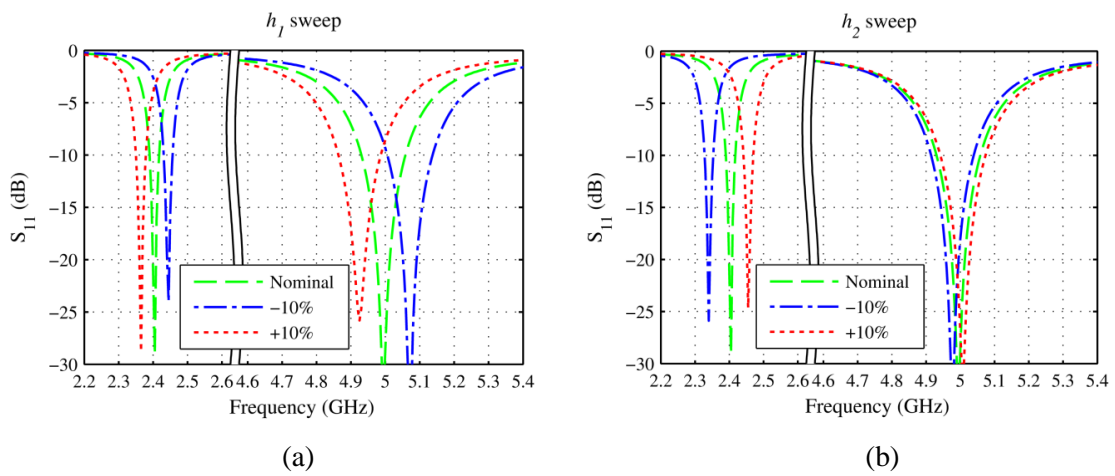


Figure 3.8. Simulated S_{11} of the antenna with varying (a) h_1 and (b) h_2 .

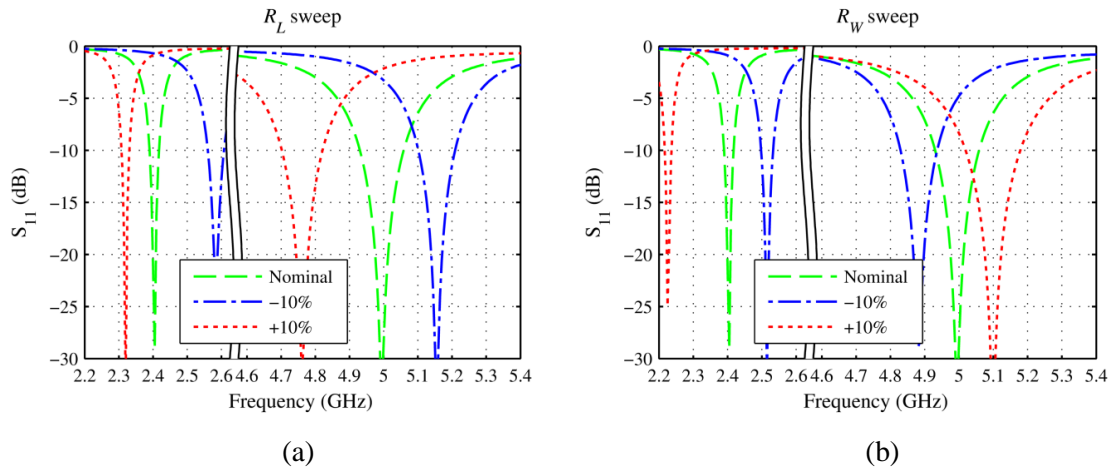


Figure 3.9. Simulated S_{11} of the antenna with varying (a) R_L and (b) R_W .

3.3.2 Independent Frequency-Band Control

This sequence of parametric studies was also inspired by the possibility of independently controlling the operating bands of the dual-frequency antenna design. In particular, the goal was to fix the lower operating band at 2.4 GHz while simultaneously allowing the upper band to independently shift to various different WiFi sub-bands near 5.0 GHz. Based on the previous parameter studies it was evident that this could be achieved by only modifying R_L and R_W , facilitating frequency shifting and variable frequency ratios, respectively. Additionally, restricting the design variability to these two parameters meant that only the interdigitated slot meander pattern would need to be modified for each antenna design; the same antenna base could be used for each design. For example, our fabrication techniques would require us to simply etch a new meander pattern and resolder.

Three additional designs were created, as shown in Fig. 3.10. Each design maintained the TM_{10} mode at 2.4 GHz, but targeted 4.8 GHz, 5.05 GHz, and 5.3 GHz for their respective TM_{30} operation. The resulting set of designs represents a -10 dB frequency range of about 12%. The interdigitated slot geometries corresponding to these three designs are given in the caption of Fig.

3.10. Based on the findings in Section 5.A, the cross-polarizations were also calculated. The maximum cross-polarizations were -6.6 dBi, -6.6 dBi, and -6.7 dBi at TM_{10} for designs 1, 2, and 3, respectively. The maximum cross-polarizations were -13.8 dBi, -8.7 dBi, and -6.2 dBi at TM_{30} for designs 1, 2, and 3, respectively.

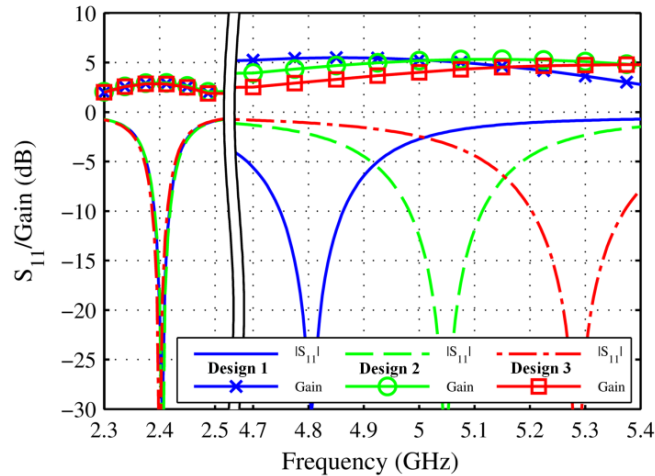


Figure 3.10. Simulated S_{11} and broadside gain of three antenna designs utilizing the same folded antenna base with different interdigitated slot loadings. The TM_{30} mode was independently shifted by up to 10%. Design 1 corresponds to interdigitated slot geometry of $R_W = 0.8328W$ and $R_L = 0.8485L_2$. Design 2 corresponds to $R_W = 0.8837W$ and $R_L = 0.7851L_2$. Design 3 corresponds to $R_W = 0.9584W$ and $R_L = 0.6711L_2$. All other antenna values are common to each design and are given in Table 1 column 2.

3.4 Considerations of Utilizing Small Ground Planes

The effect of the electrically small ground plane is considered in this sub-section. Small ground planes are attractive for use with electrically small radiators due to the reduced antenna footprint, which is critical for many mobile and wireless communication devices. However, there are often practical challenges associated with utilizing small ground planes [120]. Furthermore, many electrically small antennas are reported utilizing large ground planes, motivating a more

thorough investigation of employing electrically small ground planes and the effects they have on the radiation pattern. This is considered next.

The following analysis simulates how the ground plane size dictates the resulting radiation pattern. Specifically, the front-to-back ratio and the cross-polarization were considered. For this analysis, the design given in Table 3.1, column 2 was considered with square ground planes sized from $0.2\lambda_0$ to $1.0\lambda_0$ at 2.4 GHz. First, the resulting forwards and backwards gains at 2.4 GHz and 5.0 GHz are shown in Fig. 3.11, showing an overall increase in front-to-back ratio as the ground plane size is increased. Interestingly, after the ground plane size is increased beyond $0.5\lambda_0$, the forward gain at both resonant frequencies slightly decrease. When investigated in more detail, it was found that this was due to beam squinting at 2.4 GHz and beam splitting at 5.0 GHz. This finding highlights the strong diffraction effects of a small ground plane, underlying the need to include it in the overall antenna design procedure and corresponding simulations. Next, the forward gain and maximum cross-polarization are shown in Fig. 3.12. Evidently, the minimum cross-polarization occurs for the ground plane size employed (*i.e.* $0.3\lambda_0$), which was not a criteria in the antenna optimization, but apparently is an advantage of using a small ground plane in conjunction with the miniaturized element. The maximum cross-polarization at 2.4 GHz hits a maximum at $0.9\lambda_0$, increasing about 6 dBi from nominal. At 5.0 GHz the maximum cross-polarization also fluctuates, but remains small for the various ground plane sizes considered. Finally, the input impedance was nearly identical for all the ground plane sizes considered, but began to show small differences for a ground plane size of $0.2\lambda_0$, where the coupling with the coax-feed becomes significant. Therefore, additional investigation and fine-tuning may be required if an even smaller ground plane were desirable.

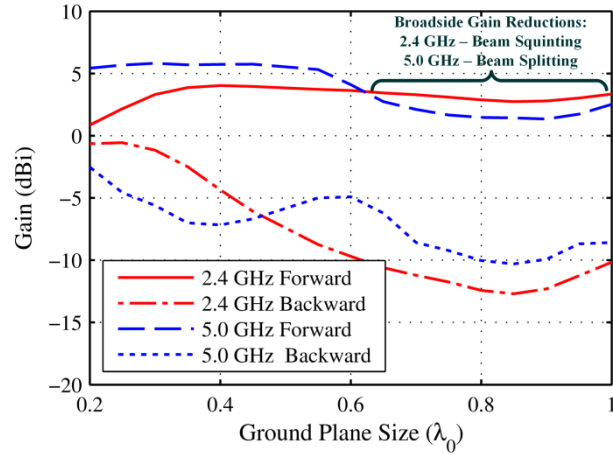


Figure 3.11. Simulated co-polarized forward and backward gains of antenna element.

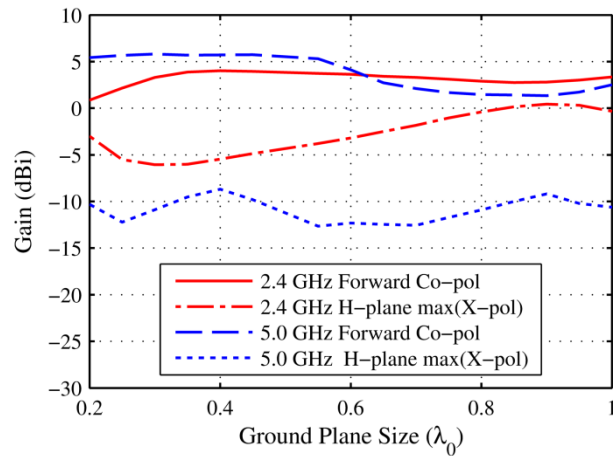


Figure 3.12. Simulated co-polarized forward gain and maximum cross-polarization in the H-plane.

3.5 Conclusions

In summary, this chapter presents the design, experiments, and analysis of an electrically-small dual-band slotted patch antenna with dimensions all smaller than $0.1\lambda_0$. Three techniques were employed to achieve the miniaturization including adding a shorting plane, subsequently folding the patch surface, and replacing the thin rectangular slots with an interdigitated slot.

When contrasted with the conventional slotted patch antenna, the interdigitated slot was shown to aid in the antenna miniaturization by properly controlling the current patterns circulating around the slot at each operational frequency band. The resulting design achieved -10 dB impedance matching bandwidths of 1.0% and 2.5% at 2.4 GHz and 5.0 GHz, respectively. The broadside gain of the optimized antenna element was predicted to be 3.3 dBi and 5.5 dBi at 2.4 GHz and 5.0 GHz, respectively, utilizing a square ground plane only $0.3\lambda_0$ -long on each side. An antenna prototype was built and tested, showing good overall agreement with simulated models. Additionally, key antenna geometry parameters were studied to determine the feasibility of independently controlling the TM_{10} and TM_{30} modes. Three additional designs were developed, demonstrating that the TM_{30} mode could be shifted by 10% while the TM_{10} mode could be left unaltered. The presented antenna design methodology provides a versatile approach of multi-frequency antenna design where antenna footprint miniaturization is a key criterion.

Chapter 4

Ultra-thin Radio Frequency Absorber Design using Circuit Approximations

4.1 Introduction

In this chapter, ultra-thin EM absorbers for RF applications are investigated. By developing equivalent circuit models, the absorber can be modularized and broken into different components for efficient optimization. First, the circuit models are used to optimize for thin profiles and wide bandwidth. Then, the circuit equations are used to isolate regions of the absorber, leading to less computationally demanding full-wave simulations, facilitating much faster optimization times. Two designs are proposed. First, a 2-layer design composed of HIS loaded by a FSS is considered. Next, the FSS-layer and capacitive layer of the HIS are consolidated into one FSS screen, allowing for a single-layer absorber design. The two designs are compared and it is found that for the same thickness, the single-layer design exhibits superior bandwidth.

4.2 Two-Layer Absorbers: Ultra-Thin Absorbers Comprised by Cascaded High-Impedance and Frequency Selective Surfaces

In this sub-section, we theoretically examine an absorber design methodology based on the well-known mushroom-type HIS [121,122]. Given that the admittance of this device can be approximated by a parallel LC circuit it is demonstrated that upon loading it with a series RLC circuit broadband absorption can be achieved while maintaining a thin absorber profile. Subsequently, a highly efficient optimization scheme is employed and a pixelized FSS is synthesized that exhibits the aforementioned series RLC circuit response. The resulting FSS is positioned a small but useful distance above of the HIS and broadband absorption is achieved. Contrary to similar approaches, our methodology separates the HIS design from the RLC load

design and predicts their combined effect based on transmission line equations. This procedure allows the individual and, consequently, highly efficient optimization of each subsystem. Alternatively, system-level optimization of an absorber is a considerably more demanding optimization problem with increased variability, leading to slower and less robust optimization procedures. In summary, the proposed methodology provides a compact modular approach towards the synthesis of any type of FSS or absorber configuration.

First, consider an HIS comprised of a metallic patch-based FSS layer cascaded by a shorted dielectric spacer. Provided that the length of the spacer as well as the size of the structure's unit cell are sub-wavelength, its input admittance can be represented by that of an equivalent parallel LC circuit, or

$$Y_{HIS} = j\omega C_1 + \frac{1}{jZ_0 \tan(\beta l)} \stackrel{|\beta l| \ll 1}{\approx} j\omega C_1 + \frac{1}{j\omega L_1} \quad (4.1)$$

where l is the thickness of the spacer. Z_0 and β are respectively the characteristic impedance and the wavenumber of the spacer material, where in this discussion it is assumed to be free space. Evidently, the patch-based FSS layer capacitively loads the inductive admittance of the PEC-backed spacer. As a result the compounded structure's input admittance zero-crossing shifts to a frequency lower than the corresponding $\lambda/4$ resonance of the shorted substrate. In this section, this property of the HIS is exploited in order to design electrically thin absorbers [123,124]. However, despite having low-profiles, HISs have the disadvantage that when either loading them across their metallic patches with resistors or when applying a uniform Ohmic sheet on their FSS layer, reasonable absorption can be achieved only for a very narrow frequency bandwidth, centered around the frequency where the susceptance in (4.1) goes to zero. If broader absorption is desired one needs to design broadband HISs. For example, in [125, 126] a broader absorption characteristic was demonstrated by loading the spacer with a magnetic material. Notwithstanding, an alternative and more promising approach would rely on loading the HIS with a suitable circuit

so that the system's total input admittance satisfies the following conditions over as wide of a frequency range as possible:

$$\operatorname{Re}\{Y_{Load} + Y_{HIS}\} = Y_0 \quad (4.2)$$

$$\operatorname{Im}\{Y_{Load} + Y_{HIS}\} = 0, \quad (4.3)$$

where Y_0 is the characteristic admittance of the surrounding/incident media, which in this case is free space. In order to identify what the characteristics of the load element should be, we first examine the monotonicity of the HIS's susceptance, provided again that for the frequency range of interest the thickness of the spacer is electrically small. From Eq. (4.1) it can be concluded that the susceptance of an HIS is a monotonically increasing function that exhibits a single zero crossing, which corresponds to the resonant frequency of the structure. Consequently, in order for the loaded HIS's susceptance to satisfy Eq. (4.3), the load should exhibit a complementary (*i.e.* equal and opposite) susceptance response. Hence, the susceptance should be either a monotonically or, when considered from a practical standpoint, locally decreasing function, with a zero crossing at the same frequency where the HIS's susceptance becomes zero. A cursory examination of candidate circuit topologies that are characterized by such a response reveals that the loading structure should be a series *RLC* circuit with an admittance given by

$$Y_{Load} = Z_{Load}^{-1} = \left(R_2 + j\omega L_2 + \frac{1}{j\omega C_2} \right)^{-1}. \quad (4.4)$$

Note here that when $R_2 = 0$ the admittance in (4.4) exhibits a Lorentzian response with an asymptote at $\omega_0 = (L_2 C_2)^{-1/2}$. However, when the resistance becomes non-zero, the sharp Lorentzian features smear out, and the susceptance becomes locally decreasing, around the aforementioned frequency. It is this characteristic of the *RLC* load's response that we want to exploit for the absorber design.

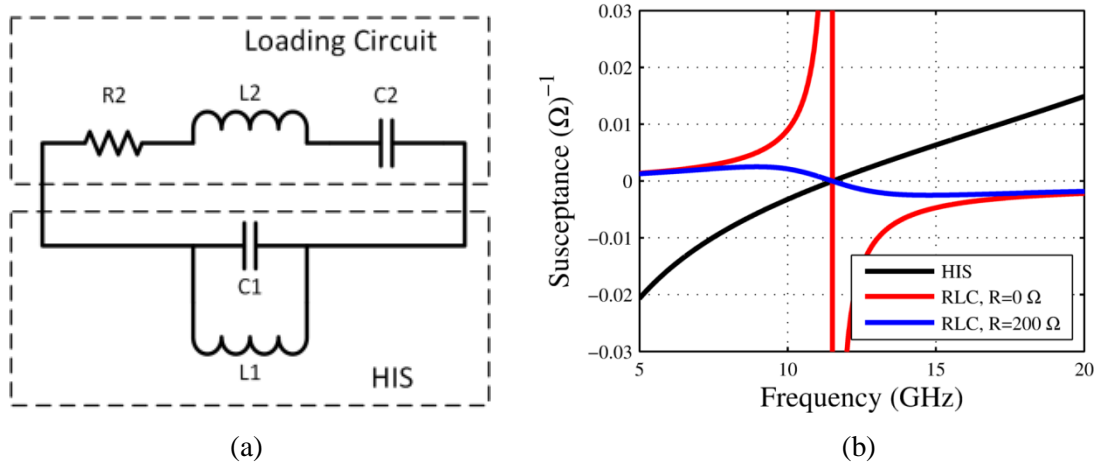


Figure 4.1. Equivalent circuit of an HIS loaded by a series RLC circuit. (b) HIS susceptance along with the susceptance of the RLC load for increasing values of $R_2 = 0 \Omega$ and $R_2 = 200 \Omega$.

The equivalent circuit schematic of this loading scheme is shown in Fig. 4.1(a). In order to demonstrate the performance of this absorber configuration let us examine the following example: we consider a HIS where the unit cell size is 8.5-by-8.5 mm². The metallic patches of the HIS are 8.1-by-8.1 mm². The constitution of the spacer is assumed to be free space and its thickness is set to 1 mm. The susceptance of this structure as computed by CST-MWS is shown with the solid line in Fig. 4.1(b). Note, the HIS under consideration exhibits its zero crossing around 11.5 GHz, which should be the targeted resonant frequency of the series RLC circuit load.

Now, it is well known that the resonance of an LC circuit is determined by the product of its inductor and capacitor values. However, there are an infinite number of inductor and capacitor combinations that result in the desired resonant frequency and only a small number of these pairs yield a suitable Lorentzian line shape capable of successfully loading the HIS under consideration, making it a good candidate for optimization. Through numerical experimentation it was concluded that the inductor and capacitor values for this particular HIS design should be $L_2 = 5.4724$ nH and $C_2 = 0.035$ pF, respectively. The susceptance of this lossless LC circuit is indicated in Fig. 4.1(b) by the dashed line. Additionally, in the same figure, the dash-dotted line

displays the corresponding susceptance after a $200\ \Omega$ resistor has been added in series with this circuit. As explained previously, the susceptance of the load now exhibits a smeared out Lorentzian response. The combined effect of the latter admittance when added to the HIS is plotted in Fig. 4.2(a). The imaginary part of the total admittance is close to zero around 11.5 GHz while at the same time its real part fluctuates around the free space characteristic admittance Y_0 , providing a good matching condition.

Additionally, in Fig. 4.2(b) the absorption performance for this loading scheme is demonstrated. In particular, the solid line corresponds to the semi-analytically computed reflection coefficient of the structure where its total input admittance is derived after adding the RLC admittance given by (4.4) to the numerically computed admittance of the HIS (solid curve in Fig. 4.1(b)). The dashed line in Fig. 4.2(b) corresponds to the loaded HIS's reflection coefficient when the total structure (HIS with RLC lumped ports) is modeled using CST-MWS.

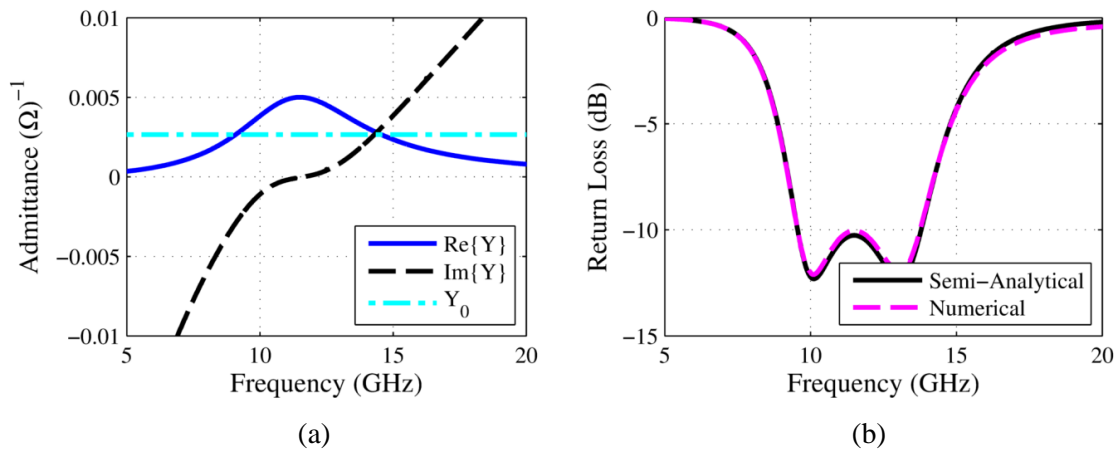


Figure 4.2. (a) Total admittance of the RLC loaded HIS. (b) Absorber reflection coefficient.

Evidently, the proposed loading scheme can successfully result in a wide enough absorption performance, where the reflection coefficient is below -10 dB from 9.5 GHz to 13.8 GHz, which corresponds to a 34% bandwidth. Despite the successful demonstration of the proposed absorber design methodology, from a practical standpoint its realization is not always

feasible due to the fact that the required capacitors and inductors may not be commercially available. So the objective becomes to design the load for a HIS, characterized by the response equivalent to that of a series RLC circuit.

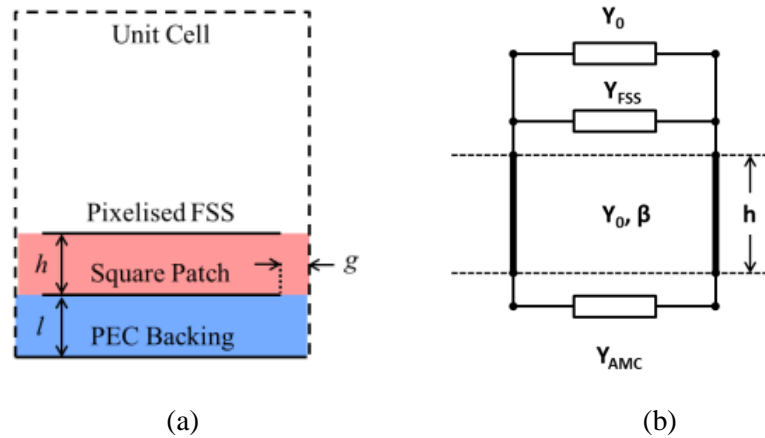


Figure 4.3. (a) Absorber unit cell side view. (b) Transmission line equivalent of the loading scheme.

The proposed alternative loading scheme is based on the design of an FSS that exhibits the input admittance of the aforementioned lossless series LC circuit. In contrast to the actual LC circuit, it is not feasible to directly attach the FSS to the HIS's patches since their metallic surfaces will make physical contact and detune one another. As an alternative, the FSS can be positioned at some small, useful distance above the HIS surface as shown in Figs. 4.3(a) and 4.3(b).

For the synthesis of this FSS layer we utilize a pixelized metallic surface whose pattern is determined through an optimization procedure that synergistically combines a method of moments (MoM) numerical solver with the CMA-ES. In particular, we consider an 8-by-8 mm² square PEC patch and we partition its area into 10-by-10 square pixels. Then, the random checkerboard pattern that yields the correct LC combination, and hence the desired FSS input admittance, is obtained by allowing the material constitution of these pixels to be either PEC or

free-space. Note here that the MoM solver was purposefully chosen for this problem since it excels in modeling all-metallic structures in terms of simulation time and numerical efficiency.

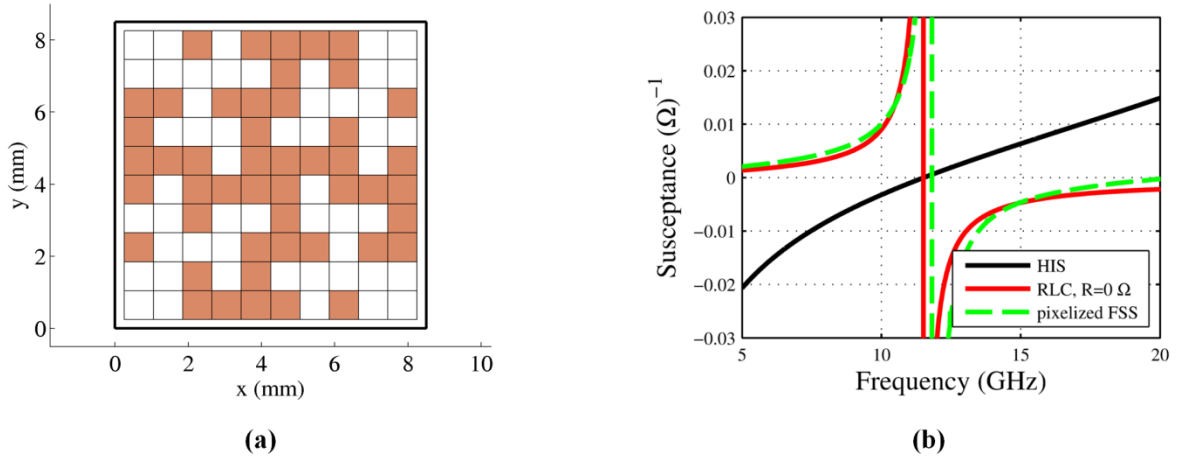


Figure 4.4. (a) Pixelized FSS. Copper corresponds to PEC and white to free space. (b) Input susceptance of the HIS, the targeted series lossless RLC circuit, and the pixelized FSS.

The objective of the optimization was the minimization of the cost function $\text{Cost} = |\Gamma_{\text{FSS}} - \Gamma_{\text{LC}}|$, where Γ_{FSS} is the numerically computed reflection coefficient of the FSS under optimization, and Γ_{LC} is the desired reflection coefficient, given by

$$\Gamma_{LC} = \frac{(Y_{Load} + Y_0)^{-1} - Z_0}{(Y_{Load} + Y_0)^{-1} + Z_0}. \quad (4.5)$$

Additionally, the optimization process was further accelerated by imposing two-fold symmetry to the random checkerboard pattern of the pixelized FSS. The resulting structure is shown in Fig. 4.4(a), and its susceptance response is depicted in Fig. 4.4(b), along with the desired susceptance, given by Eq. (4.4). Evidently, the targeted susceptance response is very well replicated by the optimized pixelized FSS.

As mentioned previously, if one could physically connect the pixelized FSS in parallel with the HIS, then it would be possible to replicate the absorption performance described in

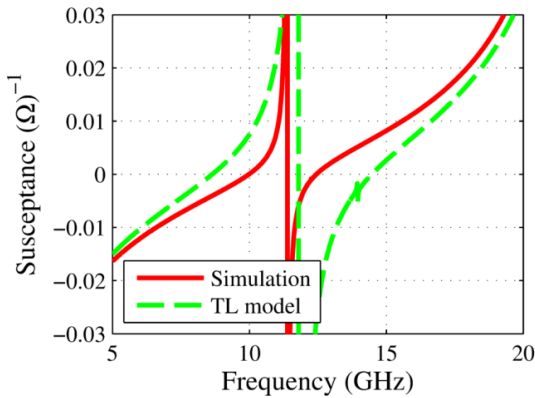
Section II. However, since this scenario is not practically feasible we examine whether a similar absorption performance can be realized by placing the pixelized FSS at some critical distance h above the HIS, as illustrated in Fig. 4.3(a).

As indicated in Fig. 4.3(b) we treat the space separating the FSS from the HIS as a transmission line segment with length h , and characteristic impedance Z_0 since its constitution is assumed to be free space. Consequently, the input admittance that the pixelized FSS layer sees is

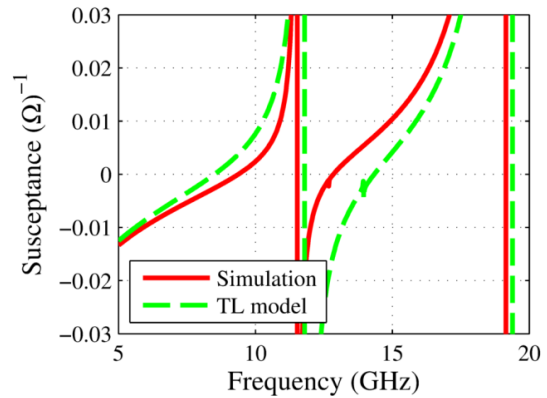
$$\tilde{Y}_{HIS} = Y_0 \frac{Y_{HIS} + jY_0 \tan(\beta h)}{Y_0 + jY_{HIS} \tan(\beta h)} \quad (4.6)$$

It can be easily verified that the translated input admittance given in (4.6) exhibits a zero crossing at a lower frequency than the one shown in Fig. 4(b). However, according to the methodology described in Section II this zero crossing needs to occur at the same frequency as the resonance of the loading RLC circuit. Therefore, we retune the translated HIS's admittance to 11.5 GHz by decreasing the size of its square patches, effectively increasing its $\lambda/4$ resonance.

In order to test the effectiveness of this loading scheme we examine four different spacing values between the pixelized FSS and the HIS. For each one the corresponding admittance was computed through (4.6), and then the zero of this admittance was retuned to 11.5 GHz by adjusting the HIS patch size. The patch dimensions along with the corresponding HIS/FSS spacing values are summarized in the first two columns of Table 4.1.



(a) $h = 0.25$ mm.



(b) $h = 0.50$ mm

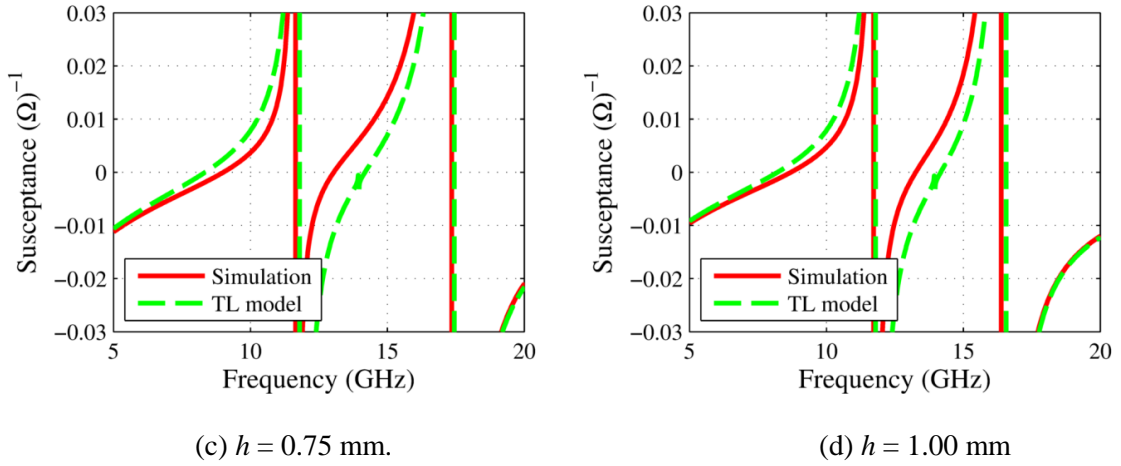


Figure 4.5. Comparison between the full-wave input susceptance of the HIS loaded by a lossless pixelized FSS, against the semi-analytical transmission line model for four different HIS/FSS separation distances.

Note that in all these designs we have maintained a constant HIS substrate thickness of $l = 1$ mm, while the material sandwiched between the two layers is free-space. Now, in Figs. 4.5(a)-(d) the solid line represents the input susceptance of the cascaded structure computed by CST-MWS, for each of the h values. The respective dashed line represents the structure's admittance derived after adding the admittance given in (6), to the numerically computed admittance of the pixelized FSS in free space.

TABLE 4.1
EVOLUTION OF THE ABSORBER PERFORMANCE FOR DIFFERENT DESIGN ITERATIONS.

Design	Geometrical Characteristics (mm)			FSS Resistivity (Ohms/Sq)	BW
	($2 \times g$)	(h)	(l)		
#1	2×0.24	0.25	1	1.5	18%
#2	2×0.26	0.50	1	3.5	29%
#3	2×0.27	0.75	1	5.0	36%
#4	2×0.30	1.00	1	7.0	41%

First, we observe that the structure's admittance exhibits a second Lorentzian resonance

that shifts to lower frequencies as the spacing value h increases. This corresponds to the first resonance of the translated HIS's admittance. Additionally, we observe that for small values of h , or when the pixelized FSS and the HIS are in close proximity, the two structures interact in such way that the 11.5 GHz total admittance resonance becomes sharper, subsequently decreasing absorption bandwidth. This destructive coupling results in the poor correlation observed between the two responses reported in Fig. 4.5(a). However, as h increases this coupling progressively becomes less pronounced and better correlation with the transmission line model is observed.

From the previous analysis it can be concluded that by sufficiently increasing the HIS/FSS spacing the interference between the two structures can be reduced. However the utility of this remedy is subjected to the following limitations: first, the spacing cannot be arbitrarily wide since it is desirable for the absorber to be as electrically thin as possible. Second, if we increase the HIS/FSS distance, as demonstrated in Fig. 4.5, the first zero impedance resonance of the HIS is shifted towards the frequency range of interest. Consequently, for the design of such types of absorbing structures the choice of the spacing should be a balance between the two competing design constraints.

It should be emphasized here that the comparison against the transmission line model reveals the coupling mechanism between the pixelized FSS and the HIS, but it also illustrates the manifestation of this effect; that is, the sharpening of the resonance at 11.5 GHz. In other words, the transmission line model is a measure of what the total admittance of the structure should ideally look like in order to achieve broadband absorption. By inspection of the susceptance plots in Fig. 4.5 it is expected that the fourth design will result in the most broadband absorption, albeit with the largest profile.

Finally, after the FSS was designed and combined with the HIS a second series of simulations were performed to derive the resistivity required for application to the pixelized FSS. In the last column of Table 4.1 we include the optimal resistivity value for each of the designs

under consideration. The corresponding absorption performance is summarized in Fig. 4.6. It can be seen that by increasing the distance between the FSS and the HIS, while at the same time decreasing the patch size, we can achieve broadband absorption similar to what would be expected in the ideal case of an HIS loaded with a series *RLC* circuit. It should be noted that even for the widest spacing value the total absorber thickness is only 2 mm, utilizing free space substrates, which renders an ultra-thin broadband design for the targeted frequency range. Furthermore, the reason for choosing a total thickness of 2 mm was to limit the profile of the absorber to be as sub-wavelength as possible, while at the same time keeping the coupling between the HIS and the FSS to a manageable level.

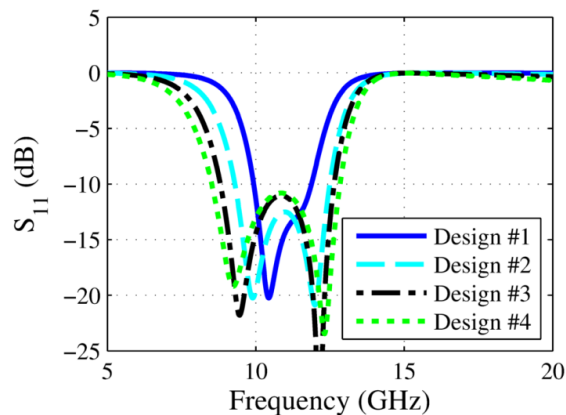


Figure 4.6. Reflection coefficient corresponding to the four absorber designs.

It should be noted that the four designs demonstrate how by progressively increasing the spacing between the HIS and the FSS, while at the same time slightly increasing the patch gap size, it is possible to recover the intended, theoretically expected absorption performance shown in Figure 4.2(b). This is further confirmed by the monotonically increasing absorption bandwidth (BW) reported in the last column of Table 4.1.

Also, Table I documented in Ref. [8] provides a list of specifications for several state of the art FSS-based absorbers. We note that our design achieves a 41% bandwidth, which is smaller

than any of the designs considered in [127]. However, the thickness of our design is only 0.057λ at the highest frequency (~ 12.83 GHz) and 0.086λ at the lowest frequency (~ 8.5 GHz) of the absorption band (-10 dB). This is by far the thinnest design compared to what is listed in Table I of Ref. [8]. This provides further substantiation of the proposed concept for reducing the thickness by capacitively loading the shorted substrate.

Additionally, several of the designs listed in [127] use FSSs consisting of double and triple loops, which means that their admittances were characterized by multiple resonances (two and three, respectively). This immediately provides greater flexibility to engineer the resistance and therefore customize the FSS admittance response as desired. As a result, the FSS admittance cancels out the substrate input admittance over a wider frequency range, which naturally results in broader bandwidth absorption. The pixelized FSS employed in our absorber was designed to resonate at a single frequency. However, the approach demonstrated here may be easily generalized to multi-resonant pixelized FSSs which could achieve absorption performance over a wider frequency range.

4.3 Single Layer FSS Design for Further and Path for Thickness Reduction

Naturally, the next step was to take the absorber theory presented in the previous section and apply it to a single FSS layer. This is preferred from a manufacturing perspective, where a single circuit board could be used (*i.e.* print the FSS on one surface and use the homogeneous PEC-backing on the opposite surface). Additionally, there may be performance advantages to a single-layer design. For example, in the previous 2-layer design the FSS load needed to be very close to, and ideally coplanar with, the array of patches in order to best represent the proposed circuit model. However, it was found that there was a coupling effect associated with the close positioning of the FSS load. To mitigate this coupling effect, extra spacing was imposed between

the FSS screen and the patches, which not only increased the overall absorber thickness, but also introduced an additional detuning of the desired input admittance. This detuning was subsequently compensated by changing the patch sizes. This process clearly complicated the overall design procedure, but it also may have diminished the resulting bandwidth of the absorber. Hence, a single-layer design was sought after.

The first step in designing a single layer absorber was to reconsider the absorber circuit approximation, which is shown in Fig 4.7a. As with the 2-layer design, the absorber loss (R_s) can be implemented independently after the correct input susceptance has been achieved. Furthermore, the admittance contribution of the thin PEC-backed substrate (L_p) cannot be varied once the thickness has been fixed, which for purposes of comparison with the 2-layer design was designated to be 2mm. Once these two contributions have been removed from the circuit model, the resulting circuit model for the desired FSS screen is what is shown in Fig. 4.7b. This represents the response the new FSS design must achieve. The overall design procedure, then, goes as follows:

1. Determine an FSS screen that has the response depicted in Fig. 4.7b.
 - a. Determine the approximate ranges available for C_s , L_s , and C_p .
2. Optimize the circuit model for maximum bandwidth.
3. Design an FSS to match the optimal circuit response from step 2.
4. Add the thin PEC-backed substrate and verify the circuit model.
5. Add loss and verify the net absorption.

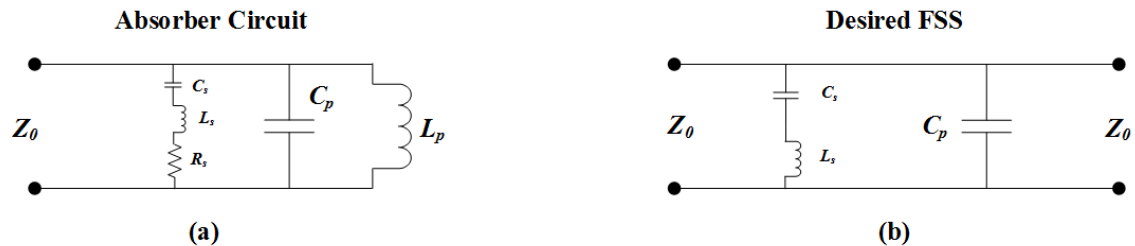


Figure 4.7. Circuit models for the (a) absorber and the (b) fss with PEC-backed substrate and loss removed.

First, we started by revisiting the mushroom-type patch array to determine the

capacitances that can be achieved. A 6.5mm unit cell was chosen as a starting point, from which a parametric study on the gap between metallic patches (which also changes the patch length for a fixed unit cell) was performed. The described geometry is shown in Fig. 4.8a, which was rendered from CST Microwave Studio. The assumed circuit model for this structure is shown in Fig. 4.8b. Figure 4.8c, which compares this circuit model to the full-wave simulation results for various gap values shows excellent agreement. As expected, the largest discrepancies are experienced at the higher frequencies, where the circuit approximation becomes less accurate.

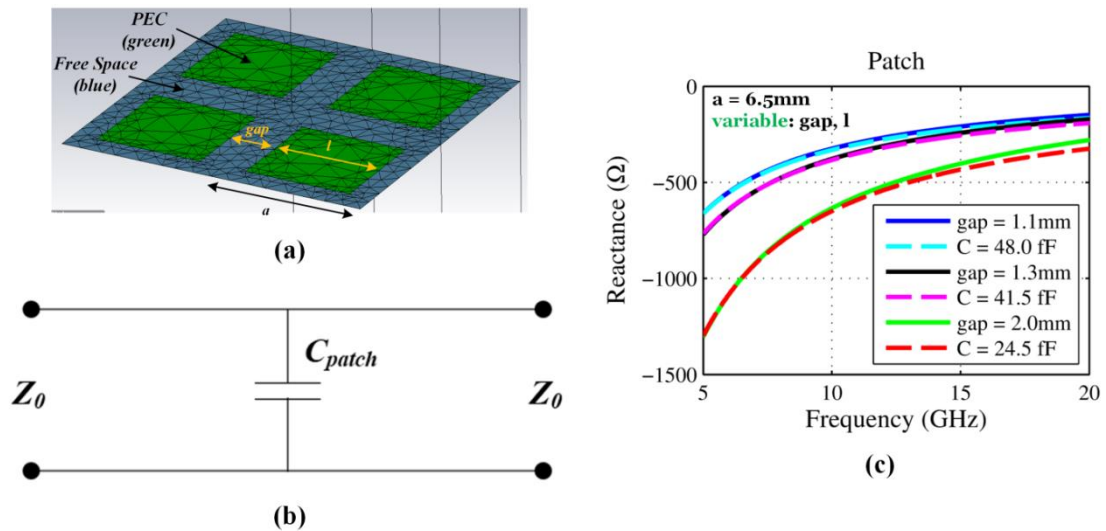


Figure 4.8. Array of patches (a) 2D geometry and simulation model, (b) circuit model, and (c) input reactance.

Next, a similar analysis was performed on the complementary structure often referred to as a wire mesh or fishnet, which is shown in Fig. 4.9a. Applying Babinet's principle to the geometry of Fig. 4.8a, the circuit approximation for this structure is expected to be inductive [128], as depicted in Fig. 4.9b. This was also verified by simulation, again varying the “gap”, which is now the PEC trace width of the fishnet structure. Excellent agreement was found with the circuit model approximation.

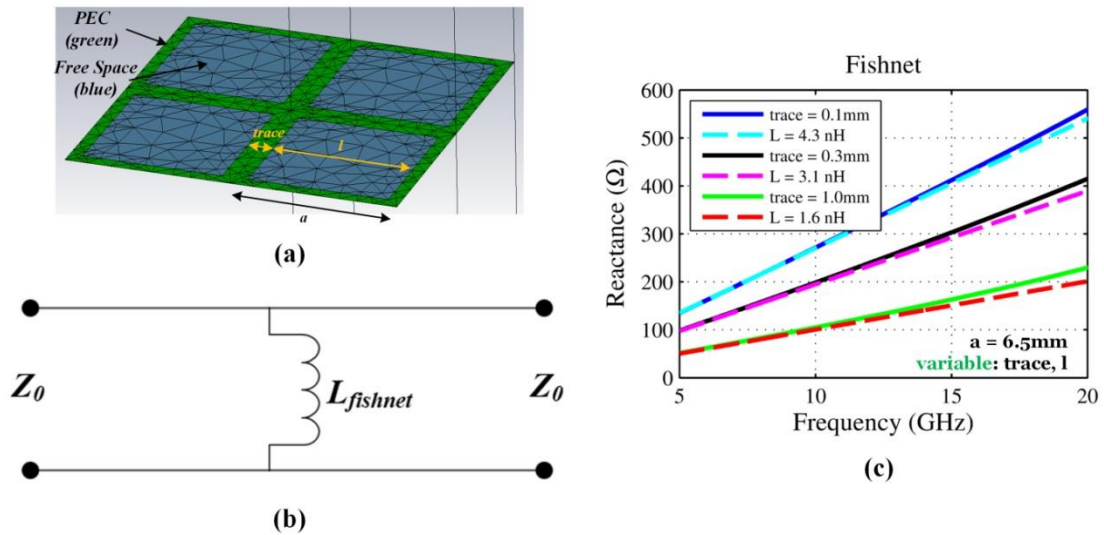


Figure 4.9. Fishnet (a) 2D geometry and simulation model, (b) circuit model, and (c) input reactance.

Next, the two previously discussed structures were positioned within the same plane, as shown in Fig. 4.10a. This structure can be approximated as a parallel LC circuit, which is shown in Fig. 4.10b, and verified in Fig. 4.10c.

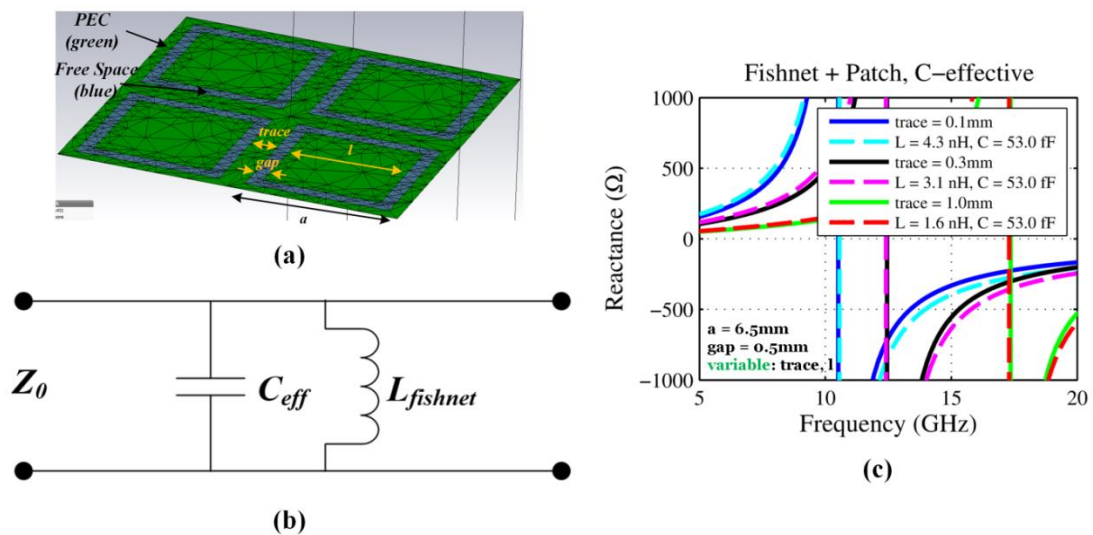


Figure 4.10. Parallel patch-fishnet configuration (a) 2D geometry and simulation model, (b)

circuit model, and (c) input reactance.

With the FSS from Fig. 4.10, all that remained was to find a capacitance to place in series with $L_{fishnet}$. The Jerusalem cross [129] is a well-known series-LC resonator, so that was employed and placed in parallel with the metallic patch. The edges of the patch needed to be cut-out to make room for the capacitive region of the Jerusalem cross, resulting in the geometry shown in Fig. 4.11a. The predicted circuit approximation for this structure is shown in Fig. 4.11b, and is precisely the desired circuit model from Fig. 4.7b. The FSS response was simulated and compared with the circuit model in Fig. 4.11c. Although the impedance resonances are slightly shifted, likely due to parasitic coupling between the elements in the FSS design, the agreement is quite good, particularly over the frequency range of interest.

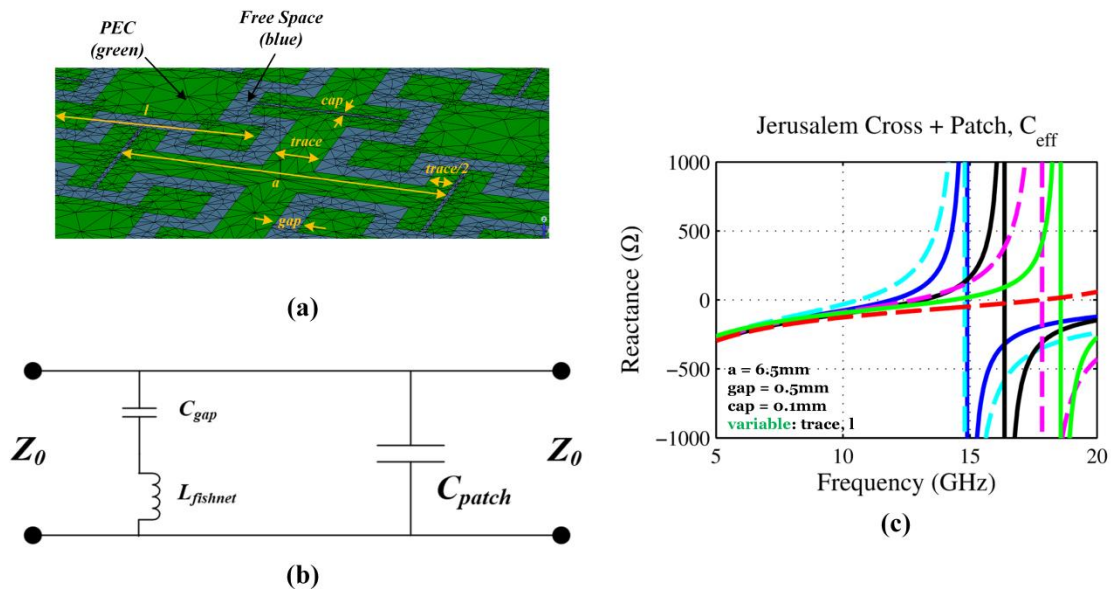


Figure 4.11. Parallel patch-Jerusalem cross configuration (a) 2D geometry and simulation model, (b) circuit model, and (c) input reactance with C_{patch} (C_{eff}) and $L_{fishnet}$ values given in the legend of Fig. 4.10c and $C_{gap} = 50$ fF.

The previous studies and resulting FSS were used as a basis for a circuit-based

optimization aimed at maximizing absorption bandwidth, using $S_{11} = -10$ dB as the criteria. Table 4.2 shows the initial ranges used for each circuit component of the FSS, which were extended slightly outside of the values calculated in Figs. 4.8 through 4.11. The optimal values for C_s , L_s , C_p , and R_s are giving in the last column of Table 4.2. Fig. 4.12 shows the resulting absorption of the circuit model. The predicted absorption bandwidth of the circuit model is notably wider than the 2-mm-thick 2-layer absorber's bandwidth shown in Fig. 4.6, indicating a potential advantage of employing a single-layer design.

TABLE 4.2
CIRCUIT-MODEL OPTIMIZATION

Circuit Component	Minimum	Maximum	Optimal Value
L_s	0.5 nH	10 nH	3.7 nH
C_s	10 fF	200 fF	60 fF
C_p	20 fF	300 fF	89 fF
R_s	10 Ω	1000 Ω	203 Ω

Minimum and maximum values based on parametric studies presented in Figs. 4.8 through 4.11.

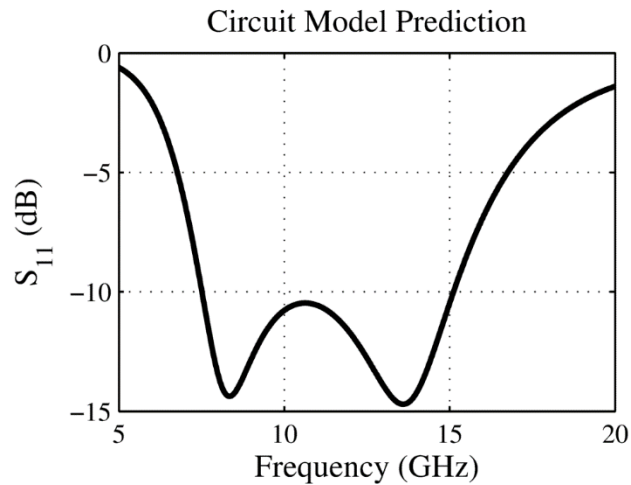


Figure 4.12. Predicted S_{11} of circuit model optimization.

Next, the FSS proposed in Fig. 4.11 was fine-tuned to provide the response of the optimal circuit elements from Table 4.2. The resulting FSS geometry is shown in Fig. 4.13a with

geometric values given in the caption. Fig. 4.13c shows the complex reflection coefficient of the fine-tuned FSS compared with the optimized circuit model given in Fig. 4.13b. Excellent agreement was found between the desired circuit reflection coefficient and that of the FSS screen. At this point, the only thing left to do was add the thin PEC-backed substrate and the loss mechanism.

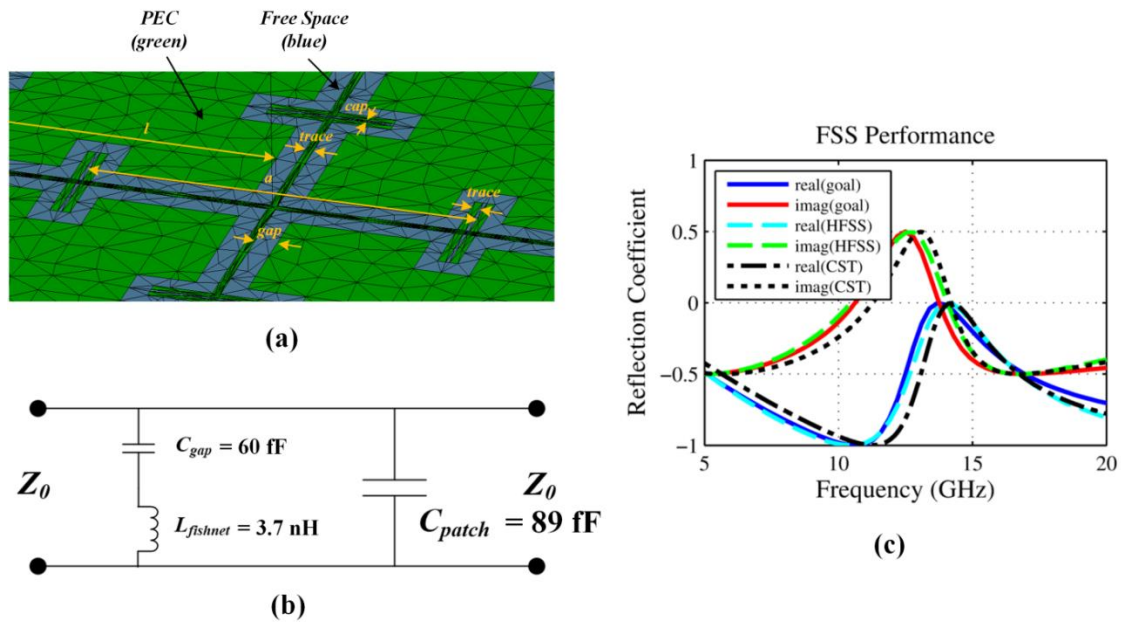


Figure 4.13. (a) Optimized FSS geometry and simulation model, where $a = 6.546\text{mm}$, $trace = 0.139\text{mm}$, $gap = 0.067\text{mm}$, and $gap = 0.364\text{mm}$. (b) Optimized circuit model. (c) Complex reflection coefficient of simulated FSS compared with circuit model.

Adding the 2-mm-thick PEC-backed substrate resulted in the geometry depicted in Fig. 4.14a. The equivalent circuit model is given in Fig. 4.14b and the resulting complex reflection coefficient comparison is given in Fig 4.14c. Again, excellent agreement was found. This verifies that the circuit model for the thin substrate is accurate and, most importantly, that the coupling between the FSS screen and the ground plane is insignificant.

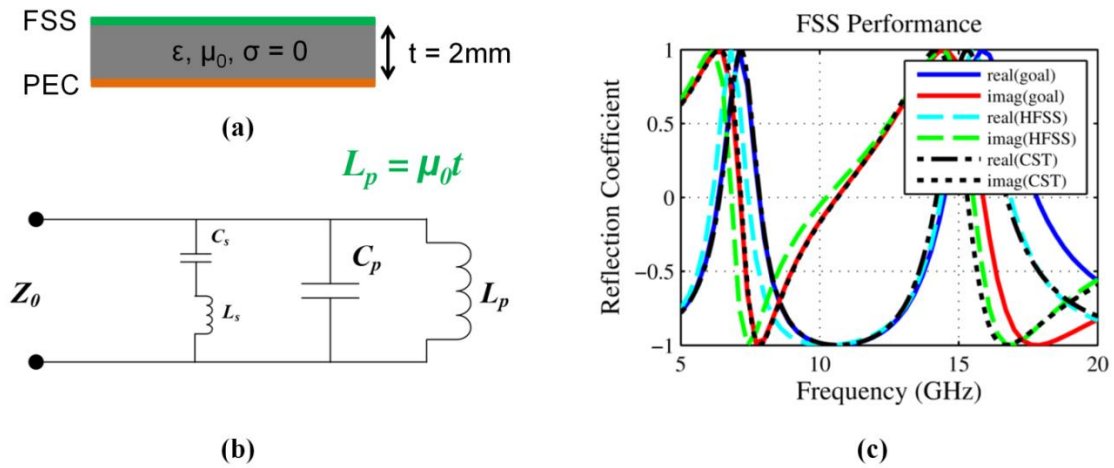


Figure 4.14. Optimized FSS with PEC-backing (a) geometry and simulation model, (b) circuit model, and (c) complex reflection coefficient comparison.

Finally, a resistive film was added to the FSS layer. The resistive value was studied parametrically until an equivalent resistance of 203Ω was achieved, which corresponded to $4 \Omega/\text{sq}$. The resulting S_{11} of the absorber is shown in Fig. 15, which was simulated in both HFSS and CST and is compared with the original absorber circuit model. The comparison matched well, with only a slight decrease in bandwidth compared to the circuit model. In particular, bandwidth has been substantially increased from 43% to 63% compared to the 2-layer absorber design.

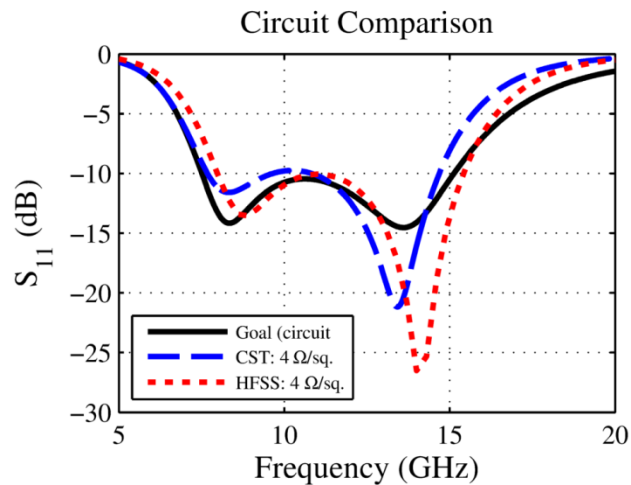


Figure 4.15. Absorber S_{11} comparison.

4.4 Conclusions

In summary, an ultra-thin absorber design methodology was proposed based on an approximate circuit model. The use of the circuit representation allows for efficient design and optimization of the absorbers. A 2-layer and single-layer design were proposed and verified through simulation. It was found that the single-layer design facilitated 50% (relative) broader bandwidth while simultaneously being easier to manufacture.

Chapter 5

Optimization of Optical Lens Systems Using Transformation Optics and a Custom Ray Tracer for Arbitrary 3-Dimensional Gradient-Index Profiles

5.1 Introduction

TO allows nearly arbitrary control over electromagnetic waves within the transformed space by requiring unconstrained control over the anisotropic, inhomogeneous refractive index. Hence, a typical TO design will require esoteric material parameters (very large, negative, near-zero, or sub-unity refractive indices, in addition to strong anisotropy) that are not found in natural materials, and may only be modeled via software simulation tools or, potentially, implemented as a metamaterial device. Although metamaterials have been considered to potentially fill this role, there are currently notable drawbacks; these include high absorption and scattering loss as well as high dispersion and narrow bandwidth, which severely limit their allowable applications, particularly in optical systems. Several extensions and approximations to the general TO technique have been suggested to reduce the dependence on or the effects of the esoteric material parameters. One such method, known as quasi-conformal mapping (qTO) [9, 130], aims to minimize material anisotropy, effectively producing material maps that may be implemented as (relatively) simple all-dielectric gradient-index (GRIN) profiles [10, 17, 131-133].

5.2 Spherical Aberration Correction by Applying Asphere-to-Sphere Transformations

GRIN lenses are known to provide aberration correction and offer superior performance to their geometrically equal homogenous counterparts. For example, utilizing axial gradients in spherically-shaped lenses was initially introduced as a means of correcting spherical aberrations [134, 135]. These and additional gradient profile types [136-138], including radial and spherical,

are now known to correct additional Seidel aberrations. Hence, it is inevitable that optical lenses with GRIN material compositions will eventually play a significant role in the design and optimization of optical systems, particularly if material systems continue to evolve and provide the capability of larger material gradients (Δn), larger maximum change in index (Δn), and lower losses (k). Typically the modeling challenge with GRIN lenses is that the optical behavior can be determined analytically for only the simplest gradients, and therefore the ray paths through truly arbitrary GRINs must be solved numerically with ray tracing software. Because of this, it is difficult to fully leverage, or optimize, the potential of three-dimensional GRINs for a variety of applications. In this section, we outline an approach that can mitigate this design obstacle.

In addition to GRIN lenses, another well-known classical method for reducing the spherical aberrations of a single spherical lens is to introduce aspherical surface perturbations [139, 140]. Therefore, we propose, through TO, to bridge the gap between the geometric and material remedies for correcting spherical aberrations. By employing qTO to map from aspherical to spherical contours, we are able to design spherical-aberration-corrected GRIN lenses possessing conventional (*i.e.* spherical/convex, flat, convex-plano, meniscus, *etc.*) geometries [141]. In practice, the contour transformations and corresponding GRIN are determined by first specifying an aspherical surface in a virtual domain. An asphere is any contour that is not spherical, and hence can be defined in a variety of ways. For this work, the asphere contours were defined by a leading spherical term plus a radial-coordinate-based polynomial perturbation series, given by

$$z(r) = \frac{r^2}{R \left(1 + \sqrt{1 - \left(\frac{r}{R} \right)^2} \right)} + \alpha_1 r^2 + \alpha_2 r^4 + \dots + \alpha_n r^{2n} \quad (5.1)$$

where α_i are the aspheric coefficients, r is the distance from the optical axis, z is the coordinate parallel with the optical axis, and R is the radius of curvature of the spherical surface in the

resulting physical domain. This is shown conceptually in Fig. 5.1. Note that the spherical surface of the physical domain can be obtained by taking the surface contours of the virtual domain and setting the aspheric (α_i) terms to zero. Hence, an aspherical perturbation is completely defined by the α_i terms. After transformation from the virtual to the physical domain, the resulting GRIN profiles are necessarily two-dimensional, but may be extended along the perpendicular axis or, more commonly, rotated about the axis of symmetry (optical axis) to yield cylindrically-symmetric lenses.

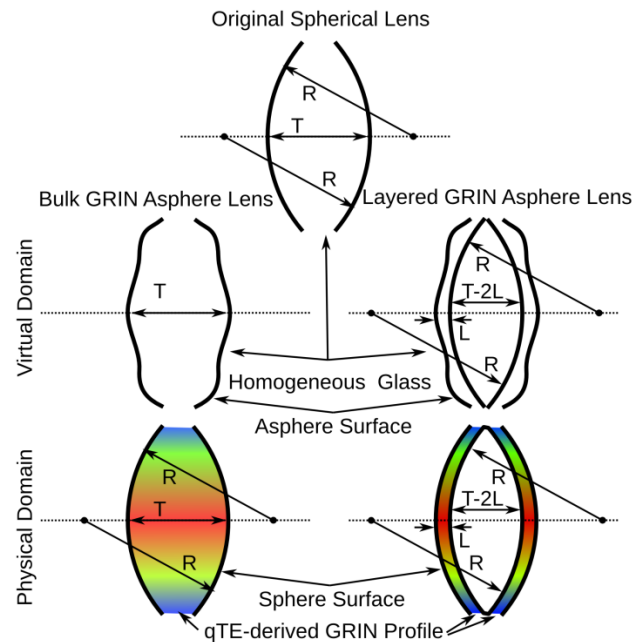


Figure 5.1. Illustration of bulk and layered qTO geometries for the GRIN asphere lenses.

Restricting the inputs of the TO procedure to only those transformations that may be expressed as quasi-conformal mappings does limit the complexity of the achievable ray or wave behavior. In particular, a qTO design is completely specified by the virtual and physical domain perimeter contours – there is no explicit control over the transformation behavior (and thus the resulting index gradients) within the interior. This simplified transformation behavior together with the high-performance requirements of diffraction limited optics means that optimizations are

required in order to select and fine-tune the correct virtual domain contours that will produce a desired output. Hence, we have successfully applied the CMA-ES to qTO design problems by parameterizing the virtual domain according to some physically meaningful system and subsequently mapping these contours into the physical domain containing the more preferable lens geometry. For example, in order to design an aberration-correcting GRIN lens, in the following examples an aspherical surface profile is selected in the virtual domain and then mapped to a spherical surface using qTO, where the aspherical perturbation coefficients in Eq. (5.1) are selected by the optimizer. The CMA-ES has the capability and was chosen to automatically parameterize itself based on the number of optimization variables, specifying key characteristics such as population size, mutation protocols, and convergence criteria. A custom in-house GRIN ray-tracer was developed and employed to evaluate the cost function of each candidate design.

The remainder of this section will consider single lens optimizations targeted for improving on-axis focusing performance using the outlined asphere-to-sphere transformation. As a starting point, we first optimized a single $f/2.5$ (“f-number 2.5”, which is the ratio of the focal distance to the entrance pupil diameter; $f/2.5$ is in the range of typical lens specifications) homogeneous spherical lens, with entrance pupil 10 mm, for minimal spot size at 4 μm wavelength. This minimization goal can be represented by the simple cost function $f_{cost} = RMS_{4\mu m}$, where RMS stands for root-mean-square spot size in the focal plane. The conventional lens is composed of silicon with $n = 3.425$. The front and back surface curvatures were equated and used as the sole optimization variable. The lens thickness was fixed to 2 mm in order to maintain an aspect ratio suitable for mechanical strength. As a result, an on-axis RMS spot size of 44.48 μm was achieved by only tuning the surface curvatures, which were optimized to $R = 124.3$ mm. With this lens as a starting point, two different ways to apply the outlined asphere-to-sphere mappings, and resulting GRIN compositions, were considered: bulk GRIN and layered GRIN.

These two general design approaches are illustrated in Fig. 1. Furthermore, we considered two layered GRIN designs with different layer thickness: 1) thick (500 μm) layers and 2) thin (200 μm) layers. All designs, both bulk and the layered, were compared in terms of RMS spot size, GRIN thickness, and the optimized GRIN profile's Δn . The motivation for these different methods, beyond spherical aberration correction, was driven by manufacturability. That is, various materials systems may be limited in terms of the Δn and GRIN layer thickness they can achieve. With that being said, this method not only provides an intuitive methodology for GRIN lens design, conversely it also offers insight into the type of material properties required for a desired optical performance within a given set of constraints, such as GRIN layer thickness. Finally, the homogeneous spherical lens and the three GRIN designs were compared with a comparable homogeneous lens with optimized aspherical surface profile.

The first example demonstrating our design approach considered a bulk GRIN. ‘Bulk’ here means that the perimeter of the virtual domain (i.e. asphere) is mapped to the perimeter of the physical domain (i.e. previously optimized spherically-shaped lens), resulting in GRIN properties throughout the entire volume. The asphere-to-sphere mapping optimization was performed by allowing for up to third-order aspheric terms (i.e. α_1 , α_2 , and α_3 in Eq. (5.1)). Identical aspherical contour definitions were used on both sides of the virtual lens in order to maintain symmetry and, in particular, reduce the number of optimization variables. Note that the asphere order should be large enough to allow for enough degrees of freedom, capable of achieving the desired performance, but not so large as to introduce an excessive number of variables, leading to an inefficient optimization routine. For this problem we found third-order to be a sufficient compromise. After optimization, the resulting spot size achieved was significantly reduced to 0.75 μm , which is diffraction limited at 4 μm wavelength. The optimized GRIN profile is shown in Fig. 5.2, showing that the notable performance improvement comes with a required Δn of only 0.002. Also note that the resulting index profile is not simply an axial or radial

gradient and is in fact truly 2-dimensional with respect to the axis of rotation.

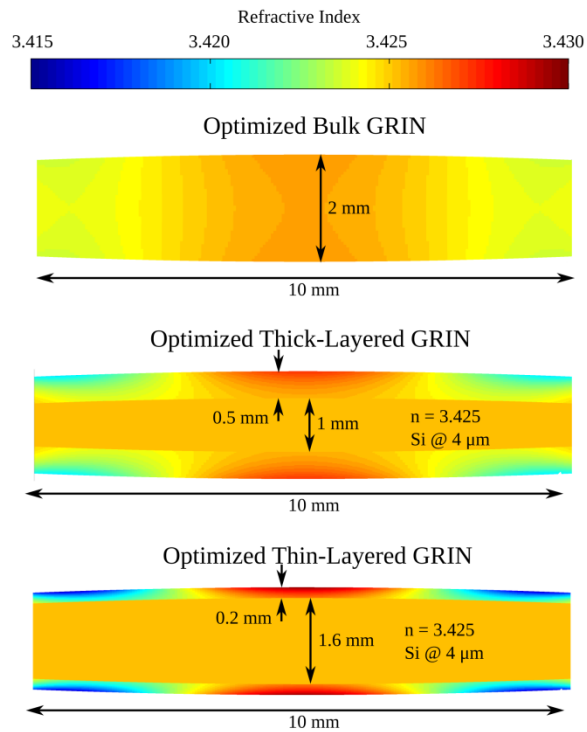


Figure 5.2. qTO-optimized GRIN profiles for the bulk and layered GRIN $f/2.5$ asphere lenses with 10 mm entrance pupil diameter. (Top) Bulk GRIN lens. (Center) Thick-layered GRIN lens. (Bottom) Thin-layered GRIN lens.

TABLE 5.1
OPTIMIZED LENS PERFORMANCES

Lens Design	RMS Spot Size	Δn	GRIN Thickness
Homogeneous Spherical	44.48 μm	0	N/A
Homogeneous Aspherical	< 0.1 μm	0	N/A
Bulk GRIN	0.75 μm	0.002	2 mm
Thick-layered GRIN	0.41 μm	0.006	500 μm
Thin-layered GRIN	0.87 μm	0.013	200 μm

Focusing performance comparison of $f/2.5$ singlet with 10 mm aperture diameter using RMS spot size calculations. Note, all GRIN lenses are spherically surfaced.

The next two design examples considered laminar GRIN layers on the surface with an

interior region composed of the same bulk silicon used to design the original homogeneous spherical lens. This is adopted with the line of reasoning that the base (untreated) material used for the GRIN layers could also serve as the bulk material of the lens interior. Nonetheless, silicon was considered solely based on its popularity at 4 μm ; this design approach can be equally extended to any materials system. The layered designs, designated as “thick” and “thin” layered GRIN lenses, were assigned layer thickness of 500 μm and 200 μm , respectively. Note that two layers, each 200 μm thick, equates to the GRIN thickness being 20% of the total lens thickness along the optical axis. Similarly, the 500 μm layered GRIN lens contains layers that total to 50% of the lens thickness. Again, in both designs the optimization variables were α_1 , α_2 , and α_3 . The optimized thick-layered and thin-layered GRIN lenses provided spot sizes of 0.41 μm and 0.87 μm , respectively, which are also diffraction limited at the targeted design wavelength. The corresponding values of Δn for each design were 0.006 and 0.013, respectively. The optimized GRIN layer profiles are provided in Fig. 5.2 and, like their bulk counterpart, are also fully 2-dimensional.

The final design considered a homogeneous lens with aspherical surfaces as a means for comparison with our TO-enabled GRIN designs. Again, starting from the original homogeneous spherical lens optimization, three asphere coefficients were then optimized for minimal spot size. The resulting homogeneous aspherical lens provided a spot size of less than 0.1 μm .

A summary of the five lens designs discussed in this section is presented in Table 5.1. For each lens the RMS spot size, Δn , and GRIN thickness are listed for comparison. To start, all attempts to correct spherical aberrations of a spherical lens resulted in diffraction limited performance at the design wavelength of 4 μm . In the case of the GRIN designs, there was a distinct trade-off between Δn and thickness of the GRIN material. Specifically, when thinner GRIN regions were employed, increased Δn was required for comparable performance, a result of increasingly localizing the spherical aberration correction to the surface regions of the composite

lens. This trade-off is visualized in Fig. 5.2, which plots the GRIN profiles of the three lens designs on common spatial (up/down, left/right) and refractive index (color) scales. What is particularly compelling about this comparison is that it demonstrates the flexibility for an optical engineer to use TO to design multiple lenses with varying GRIN characteristics, analyze and compare them, and subsequently mate the designs with capable materials systems, facilitating more streamlined design-to-fabrication; all of this without sacrifice in performance. An alternative way to analyze the required Δn for a given GRIN thickness is to consider the optimized asphere coefficients, which are listed in Table 5.2. That is, thinner GRIN regions called for larger asphere coefficients, which upon transformation to a spherical contour translated to larger Δn . Also note the consistency between the optimized asphere coefficients of the GRIN lens designs and the homogeneous geometrical asphere. The only term with a different trend was α_3 of the homogeneous asphere; however, it can be noted that the relative magnitude of this term with its companion α_1 and α_2 is very small, indicating that it was significantly less important than in the GRIN designs. The dominant terms of the geometric asphere, on the other hand, clearly have the same trends as the GRIN designs. The data presented in Table 5.2 is also organized graphically in various forms in Fig 5.3. First, surface contours of all designs are plotted by inserting the coefficients listed in Table 5.2 into Eq. (1) with $R = 124.3$ mm. Of course, in the case of the GRIN lenses the surface contours correspond to the virtual domain. It is apparent that the asphere contours generally vary little from that of the sphere, yet differs largest in the case of the thin-layered GRIN lens. This is no surprise because in order to obtain the same aberration correction as the bulk GRIN lens there must be an increase in Δn and ∇n within the thin laminar GRIN layers. In the virtual domain this corresponds to larger contour deviations from the sphere. Next, to more closely examine the asphere contours the center plot in Fig. 5.3 displays the contours with the spherical contribution subtracted, according to

$$y = z_{asphere} - z_{sphere} \quad (5.2)$$

From this it is evident that as the layer thickness decreases the asphere contribution becomes stronger in the virtual domain, creating more extreme material definitions in the physical domain and further demonstrating the trade-off between GRIN layer thickness and Δn . Lastly, in the bottom plot the asphere contours are normalized by

$$y = \frac{z_{\text{asphere}} - z_{\text{sphere}}}{\max(z_{\text{asphere}} - z_{\text{sphere}})} \quad (5.3)$$

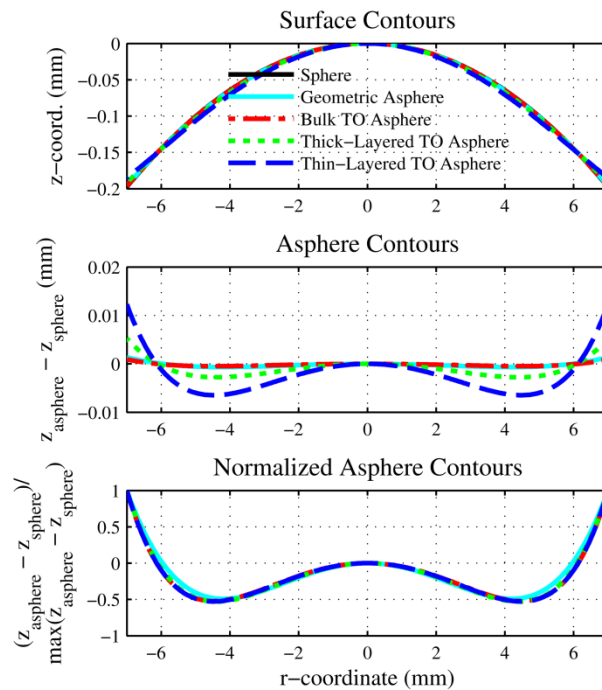


Figure 5.3. (Top) Surface contours of each lens design. Note that the surface contours of the GRIN lenses correspond to the virtual domain definition. (Center) Asphere contours. (Bottom) Normalized asphere contours.

Immediately we see that the GRIN contour definitions, although having magnitudes inversely proportional to the GRIN layer thickness, have nearly identical profiles. This result could be leveraged since only one optimization would be required for multiple lenses with various GRIN layer thicknesses. Lastly, it is seen again that the geometric asphere is similar but not identical to the GRIN lens contour definitions. In particular, we see the effect of the negligible

third order term, showing largest contour deviations furthest from the origin.

TABLE 5.2
ASPHERE COEFFICIENTS OF LENS DESIGNS

Lens Design	α_1	α_2	α_3
Homogeneous Spherical	0	0	0
Homogeneous Aspherical	7.67e-5	-2.24e-6	2.06e-9
Bulk GRIN	4.42e-5	-8.00e-7	-9.96e-9
Thick-layered GRIN	2.75e-4	-6.13e-6	-3.41e-8
Thin-layered GRIN	5.99e-4	-1.12e-5	-1.25e-7

This sub-section demonstrates several variations of a new, intuitive approach for the design of aberration-corrected GRIN lenses using TO. Specifically, we have employed qTO to map between aspherical and spherical contours as a means to correct spherical aberrations of a single lens. We believe this design approach can be broadly extended to deliver on other performance goals, such as improved chromatic aberration correction or improved aberration-corrected field of view when implementing multi-lens systems. Furthermore, we have considered bulk and layered GRIN approaches to accommodate varying restrictions due to current and emerging fabrication technologies.

The fabrication techniques required to realize the arbitrary three-dimensional index gradients of any of the presented designs were not the focus of this section, but were an underlying motivation for comparing the bulk and layered GRIN implementations. Certainly, the materials development will be crucial for the realization of GRIN lenses and the benefits we have outlined in this work. There are several general approaches that are currently under investigation and development to produce optical-quality GRIN devices, including those based on additive (3D-printing) and subtractive manufacturing, those based on material mixing rules for small embedded scatterers, and those based on controlled doping of a bulk media to alter the surrounding index.

The design and optimization techniques presented here represent a strong separation from the assumptions and practice of conventional optical design and manufacturing. Rather than approach aberration-correction with either geometric or GRIN remedies, we have bridged the gap between the two, as enabled by TO. With this design approach, the possibility of creating completely arbitrary GRIN profiles based on TO is expected to be a powerful tool for the creation of new and more flexible RF and optical devices.

5.3 Achromatic Gradient-Index Lens Design using Transformation Optics

TO has matured into a field responsible for many new optical devices and design methodologies. Simultaneously, metamaterials have advanced, in part, to construct the devices predicted by TO, which often require esoteric material properties. Metamaterials frequently rely on resonant phenomena, leading them to have narrow bandwidth and, therefore, limited applications. qTO was introduced as a mitigating method, by allowing near-isotropic non-magnetic material distributions, thus facilitating all dielectric gradient-index (GRIN) devices. Other attempts have been made to apply TO in such a way as to avoid near-resonant frequency operation [142]. However, transformation optics has not yet been exploited directly for dispersion correction. In this section, it is shown that TO can be applied to correct for dispersive effects by replacing a single coordinate transformation with a set of transformations, each corresponding to different frequencies. Finally, an instructive example is considered for demonstration and analyzed for effectiveness.

Consider the lens maker's equation for a focusing lens composed of a homogeneous refractive index:

$$\frac{1}{f} = (n - 1) \left[\frac{1}{R_1} - \frac{1}{R_2} + \frac{(n-1)d}{nR_1R_2} \right] \quad (5.4)$$

where f is the focal length, n is the lens' refractive index, R_1 and R_2 are the surface radii, and d is the thickness of the lens. The thin lens equation, where $d \ll R_{1,2}$, can be obtained by setting d equal to zero. From (5.4), it is evident that the focal length, or power, of the lens highly depends on the refractive index, which is generally frequency dependent. Therefore, different colors have different focal points, a phenomenon known as focal drift, $\delta f = \max(f) - \min(f)$, causing white light to *blur* along the optical axis. In classical lens design, this phenomenon is often minimized or corrected for by introducing additional lens elements composed of materials with significantly different dispersions. These lens systems are known as achromats and aprochromats [139, 140].

An alternative approach to dispersion-correction can be hypothesized by imagining if the geometric properties in (5.4), namely R_1 and R_2 , could also vary with frequency. Restricting this thought experiment to thin lenses with $R_1 = -R_2$ (symmetric biconvex), the condition for $\delta f = 0$ occurs when

$$R(\omega) = 2f[n(\omega) - 1] \quad (5.5)$$

Unfortunately, it is not possible for a lens to simultaneously have multiple geometries and, thus, this procedure will not work for broadband applications. However, TO allows for geometric mappings to be interpreted as GRIN material compositions. Therefore, $R(\omega)$ can be calculated for a given dispersive material and subsequently mapped to a common lens geometry. This process is illustrated in Fig. 5.4, where a hypothetical material with a monotonically increasing refractive index is considered. At lower frequencies (f_1) the refractive index is smaller, requiring increased surface curvature for a given focusing power. Conversely, at higher frequencies (f_3), where the refractive index is larger, decreased surface curvature is necessary. In this example, the three lenses were mapped to the lens geometry with surface curvature corresponding to the desired behavior at f_2 . In each case, the unique GRIN profiles, which are nearly radial, contribute to the overall power of the lens [143]. The GRIN profile is diverging

when the lens is stretched to have more curvature (f_3) and converging when the lens is flattened to have less curvature (f_1). Hence, as the frequency increases, the focal drift associated with the lens geometry must be corrected with an equal and opposite dispersion associated with the GRIN. That is, with increasing refractive index, the lens geometry pushes the focal plane towards the lens. Hence, a GRIN that becomes increasingly diverging is required to compensate. This result corroborates previous work on GRIN color-correction [144-148].

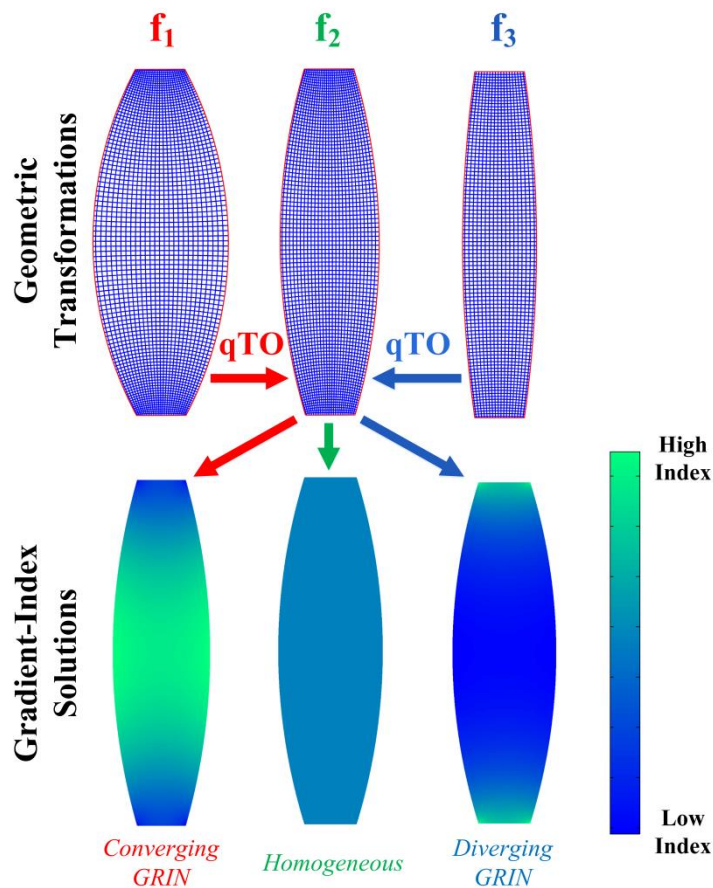


Figure 5.4. Example coordinate transformation used for dispersion correction.

In order to analyze the effectiveness of the proposed method, an example was considered for color correction. The lens was assigned an illumination aperture of 10 mm, a thickness of 2 mm, and a desired focal length of 60 mm. A hypothetical GRIN material was proposed that has

an average refractive index of 3.3, 3.6, and 3.9 at f_1 , f_2 , and f_3 , respectively. Here, “average” index is related to the surface dispersion, or n in Eq. (5.4). Then, applying Eq. (5.5), the corresponding surface radii are 276 mm, 312 mm, and 348 mm. Next, all cases were mapped to a lens with 312 mm radii and a thickness of 2 mm. The resulting GRIN profiles are similar to those shown in Fig. 5.4, specifically with minimum and maximum refractive indices of [3.287, 3.321], [3.600, 3.600], and [3.880, 3.912] at f_1 , f_2 , and f_3 , respectively. This type of GRIN material could be realized, for example with the mixing of two metamaterials, where $n_{Mix} = pn_1 + (1 - p)n_2$. Here, n_1 and n_2 refer to Material 1 and Material 2, respectively. This idea is visualized in Fig. 5.5, which shows the dispersion curves of the two materials and the lens’ filling factor p with respect to Material 1.

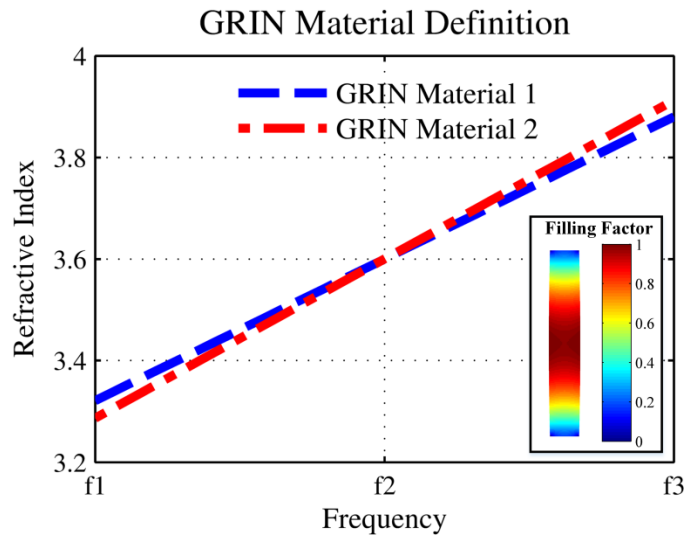


Figure 5.5. GRIN material requirement for dispersion-correction.

The resulting dispersion-corrected lens was simulated using a ray-tracer and the focal location at each frequency was calculated. For comparison, the focal location of a homogeneous lens using the same material system with $R = 312$ mm was also calculated and is shown in Fig. 5.6. The focal drift of the GRIN is about 3x better with respect to the homogeneous lens. In fact,

the GRIN not only corrects the dispersion of the lens geometry, it over-corrects it. This is likely due to the embedded nature of the transformation [149], where the free space boundaries, which are also transformed, are ignored. It's also worth noting that, due to over-correction, this lens has a negative Abbe number, producing a focal drift opposite to classical optics. This could be of particular interest in multi-lens systems where color-correction is desired.

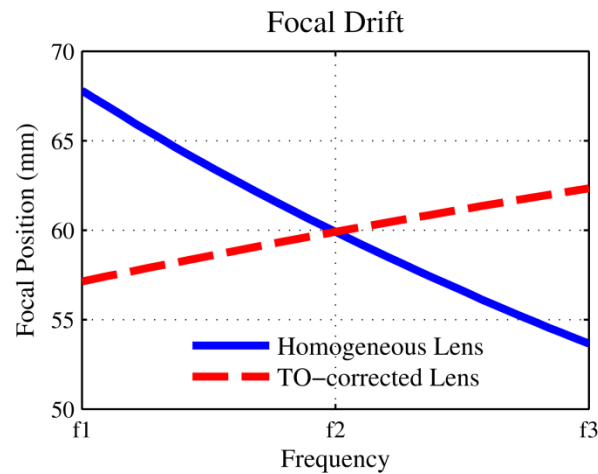


Figure 5.6. Focal drift of a standard homogeneous and TO-corrected GRIN lens.

Moving forward, it will be important to correct for the embedded nature of the transformation, which if accomplished will lead to further improvement of the TO dispersion-correction technique. Also, the ultimate goal is to perform this process inversely. That is, given a material system, determine the correct GRIN profile and geometry.

5.4 Transformation Optics-Inspired Achromatic Gradient-Index Lens Design

In the previous section, a set of TO mappings was found in order to obtain color-correction within in a single lens. The resulting lenses contained a GRIN profile that was close to radial; however, the resulting material definitions were not practical when compared to many of the known GRIN systems. Hence, in this section we take the findings from the previous study and

apply them to design achromatic radial-GRIN singlets using existing material systems. Specifically, a GRIN focusing singlet lens composed of a Ge-Si mixture is compared with homogeneous singlets made of Ge and Si as well as a homogeneous Ge-Si doublet, which is known to have significantly improved color-correction capabilities [139, 140]. Both the monochromatic and chromatic performances of these lenses are compared.

5.4.1 Axial Chromatic Aberration of Classic Lenses

To demonstrate the color-correcting capabilities of GRIN lenses, we first consider a focusing lens with an object at infinity. The focal point of such a lens is a function of the lens thickness, surface curvatures, and refractive index. The refractive index of a typical lens glass is dispersive, which causes the focal point to vary with the wavelength resulting in axial chromatic aberrations. Physically this can often be seen in a separation of primary colors in the focal plane.

Now suppose we consider the task of designing an $f/5.0$ focusing lens with a pupil diameter of 12mm for $3\mu\text{m}$ to $5\mu\text{m}$ operation. Two popular materials for these wavelengths were considered: Ge and Si, which have refractive indices of 4.044, 4.025, 4.016 and 3.432, 3.425, 3.422, respectively, at wavelengths of $3\mu\text{m}$, $4\mu\text{m}$, and $5\mu\text{m}$. Note then that these values define the refractive index bounds on the GRIN materials system, providing a maximum change in refractive index (Δn) of 0.612, 0.600, and 0.594 at $3\mu\text{m}$, $4\mu\text{m}$, and $5\mu\text{m}$, respectively. The lens thicknesses were fixed to 3mm and only the front (R_f) and back (R_b) surface curvatures were tuned for optimal performance. The optimization goal was to minimize the root-mean-square (RMS) spot size diameters at each design wavelength as well as the defocusing of the lens $f/\delta f$, which is the ratio of the focal point f and focal drift δf , and is a measure of the chromatic performance of the lens. The resulting geometries are given in Table 5.3 and focusing performance metrics are summarized in Table 5.4. The full lens geometries and resulting ray tracing diagrams are shown in Fig. 5.7a and

Fig. 5.7b for Ge and Si, respectively. It is evident that a small spot size can only be achieved at one wavelength for a homogeneous singlet. The defocusing is smaller (worse) for the Ge singlet than the Si singlet, a result of Ge being more dispersive from 3 μm to 5 μm .

In classic lens design, detrimental dispersive effects must be corrected by introducing additional lens elements made of a material with differing dispersion. For example, typically a diverging lens composed of a more dispersive material (*i.e.* flint glass) is mated with a converging lens made of a less dispersive material (*i.e.* crown glass). When their optical properties are combined, the resulting system has an overall focusing characteristic that is less sensitive to dispersion because the dispersive effects of the diverging lens and the converging lens are opposing in nature. This type of system is referred to as an achromatic doublet. For comparative purposes, a Ge-Si achromatic doublet was also designed for minimal spot size at each wavelength and minimum focal drift. The doublet was assumed to be cemented and therefore contained three unique surface curvatures. The thickness of each region was fixed to be 1.5mm, resulting in a total thickness equal to the previously discussed homogeneous singlets. The front and back surface curvatures of each region are given in Table 5.3. The full lens geometry, refractive indices, and ray trace diagram are given in Fig 5.7c. Table 5.3 lists the resulting spot sizes at each design wavelength, which are all diffraction limited, as well as the defocusing which shows significant improvement over the homogeneous singlets composed of either Ge or Si.

5.4.2 Axial Chromatic Aberration of a Ge-Si GRIN Singlet

Next, the dispersion of a GRIN system generated by mixing Ge and Si is considered. The refractive index of the Ge-Si mixture is defined by $n_{Ge-Si} = (1-p)n_{Ge} + pn_{Si}$ where p is the filling fraction of Si in the Ge host. As will be demonstrated next, a GRIN lens constructed by mixing two materials with differing dispersions can be designed to have two opposing focal drift

characteristics, analogous to what happens with a properly designed homogeneous achromatic doublet. Because the refractive indices of each base material in a Ge-Si mixture both decrease with wavelength, the resulting focal drift will be similar to that of a Ge or Si homogeneous singlet. Specifically, with a decrease in refractive index the focal plane will drift away from the lens. However, imagine a GRIN profile that simultaneously has opposing dispersive effects. Thus, for this example the GRIN should move the focal plane in towards the lens. Next, recall that the difference in index between Ge and Si decreases with increasing wavelength and consequently, the power of the GRIN decreases. Therefore, if we design a GRIN to have a diverging effect, the focal plane of the GRIN lens will move towards the lens with increasing wavelength. The diverging GRIN was defined by a second-order radial profile, given by

$$n_{GRIN} = n_0 + c_1 r^2 + c_2 r^4 \quad (5.6)$$

where c_1 and c_2 are optimization variables in addition to the lens surface curvatures and thickness. The resulting geometric properties are given in Table 5.3. The optimized lens geometry, GRIN profile, and resulting ray diagram are provided in Fig. 5.7d. The chromatic performance of the GRIN singlet is given in Table 5.4, showing diffraction limited performance at each design wavelength as well as near-zero focal drift.

TABLE 5.3
GEOMETRY OF SINGLETS

Lens Design	Geometric Lengths		
	R_f	R_b	t
Homogeneous Ge Singlet	63.8	93.2	3
Homogeneous Si Singlet	61.4	99.9	3
Homogeneous Ge-Si Doublet	59.7, 213	213, 107	1.5, 1.5
GRIN Ge-Si Singlet	40.1	55.3	2.66

TABLE 5.4
CHROMATIC PERFORMANCE OF SINGLETs

Lens Design	Focal Plane On-Axis RMS Spot Sizes (μm) and Defocusing			
	$3\ \mu\text{m}$	$4\ \mu\text{m}$	$5\ \mu\text{m}$	$f/\delta f$
Homogeneous Ge Singlet	54.2	2.59	24.6	104.8
Homogeneous Si Singlet	24.6	3.20	11.8	230.7
Homogeneous Ge-Si Doublet	2.59	2.61	2.62	30,630
GRIN Ge-Si Singlet	2.16	2.27	2.23	78,480

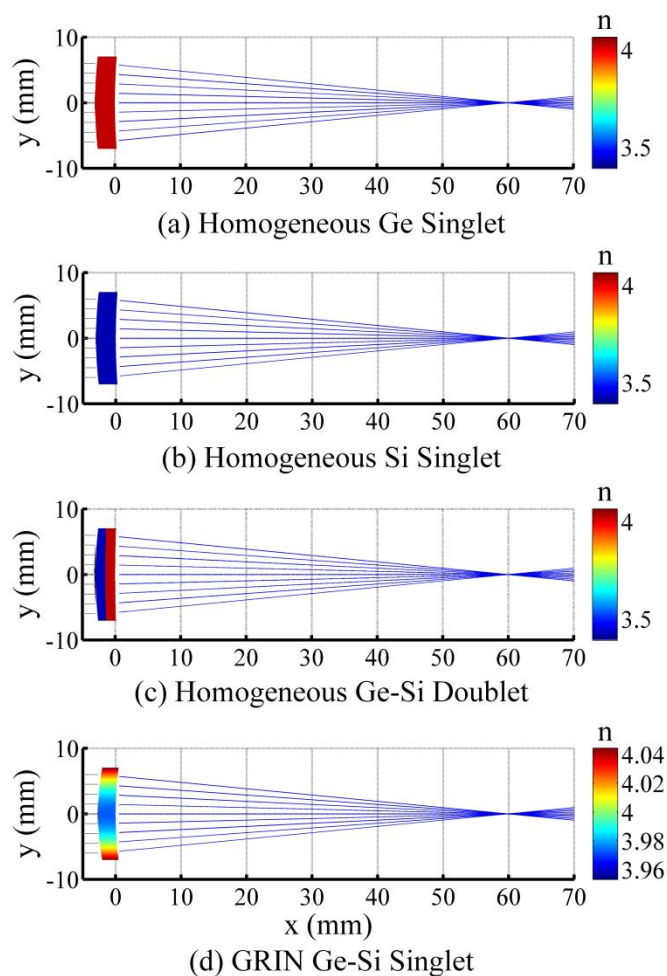


Figure 5.7. Ray trace diagrams and refractive index distributions of the (a) Germanium singlet, (b) Silicon singlet, (c) Germanium-Silicon doublet, and (d) Germanium-Silicon GRIN singlet.

In this section, a method to design color-corrected GRIN lenses is presented. An example using a mixture of Ge and Si is presented and compared with both homogeneous singlets and a Ge-Si achromatic doublet. This design methodology and the general understanding of chromatic aberration correction will be crucial for optical designs as GRIN material technologies continue to mature.

5.5 Dispersion Corrected Dispersive Metamaterial Lenses using Ray Tracing Equations

In this next section, color-correction techniques using ray-tracing equations are applied to lens made of metamaterials, which usually exhibit very high levels of dispersion. Metamaterials that operate away from resonance have been investigated as a way to mitigating bandwidth and loss issues [142]. Certainly, for applications such as lenses, standard dielectrics can also be used to improve bandwidth [150]. Yet, even traditional dielectrics suffer from dispersion, which is particularly problematic in optical systems where the operating wavelength is very small. Finally, reconfigurable [151] and tunable [152] metamaterials can provide an avenue for dispersion-correction, but these structures have limitations in their own right due to the extra challenges involved with their complex active circuitry. In this section, an analytical method based on paraxial ray-tracing equations is proposed for passive dispersion-correction in metamaterial lens design. Rather than avoiding dispersive materials to prevent focal drift, this technique corrects for materials dispersion by compensating it with dispersion arising from the lens geometry itself. Analogous to optical achromatic doublets, the two sources of focal drift can be used to cancel one another, facilitating dispersion-corrected lens design.

First, consider a lens with a GRIN profile defined as

$$n(r, z) = n_0 + \alpha_z \left(\frac{z}{T} \right) + \alpha_r \left(\frac{r}{D/2} \right)^2 \quad (5.7)$$

where r is the radial position of the rotationally symmetric lens, z is the axial position, D is the diameter or aperture of the lens, T is the on- z -axis thickness of the lens, n_0 is a constant and α_r and α_z are the radial and axial GRIN coefficients. The only imposed constraint is that $|\alpha_r| + |\alpha_z| = \Delta n$, which is the total range of refractive index provided by a given metamaterial system. Front and back surface indices are evaluated at axial distances $z = -T, 0$, respectively, and at a radial location $\sqrt{1/3} D/2$ while their corresponding Abbe #'s are given by $\nu_{f,b} = (n_{f,b_2} - 1)/(n_{f,b_3} - n_{f,b_1})$. The set of equations defining the focusing power and dispersive nature of the lens are given by

$$\begin{aligned}\phi_f + \phi_b + \phi_G &= \phi_T \\ \frac{\phi_f}{\nu_f} + \frac{\phi_b}{\nu_b} + \frac{\phi_G}{\nu_G} &= \delta\phi_T\end{aligned}\tag{5.8}$$

where $\phi_{f,b} = \pm(n_{f,b_2} - 1)/R_{f,b}$ are the paraxial thin lens powers associated with the front and back surfaces, respectively. The plus sign in the equation corresponds to R_f and the negative to R_b . The paraxial GRIN power $\phi_G = -2\alpha_r T/(D/2)^2$, while ϕ_T is the total lens power. The GRIN Abbe # $\nu_G = \Delta n_2/(\Delta n_3 - \Delta n_1)$. The change in lens power $\delta\phi_T \rightarrow \pm 0$ in the dispersion-corrected limit, which leads to

$$\begin{aligned}\phi_f &= \left(\frac{\nu_f}{\nu_f - \nu_b}\right)(\phi_T - \phi_G) + \left(\frac{\nu_f \nu_b}{\nu_f - \nu_b}\right)\frac{\phi_G}{\nu_G} \\ \phi_b &= \left(\frac{\nu_b}{\nu_b - \nu_f}\right)(\phi_T - \phi_G) + \left(\frac{\nu_f \nu_b}{\nu_b - \nu_f}\right)\frac{\phi_G}{\nu_G}\end{aligned}\tag{5.9}$$

Next, solving for expressions of the surface radii yields

$$\begin{aligned}R_f &= \left(\frac{n_{f_2} - 1}{\phi_T + (\nu_b/\nu_G - 1)\phi_G}\right)\left(\frac{\nu_f - \nu_b}{\nu_f}\right) \\ R_b &= \left(\frac{1 - n_{b_2}}{\phi_T + (\nu_f/\nu_G - 1)\phi_G}\right)\left(\frac{\nu_b - \nu_f}{\nu_b}\right)\end{aligned}\tag{5.10}$$

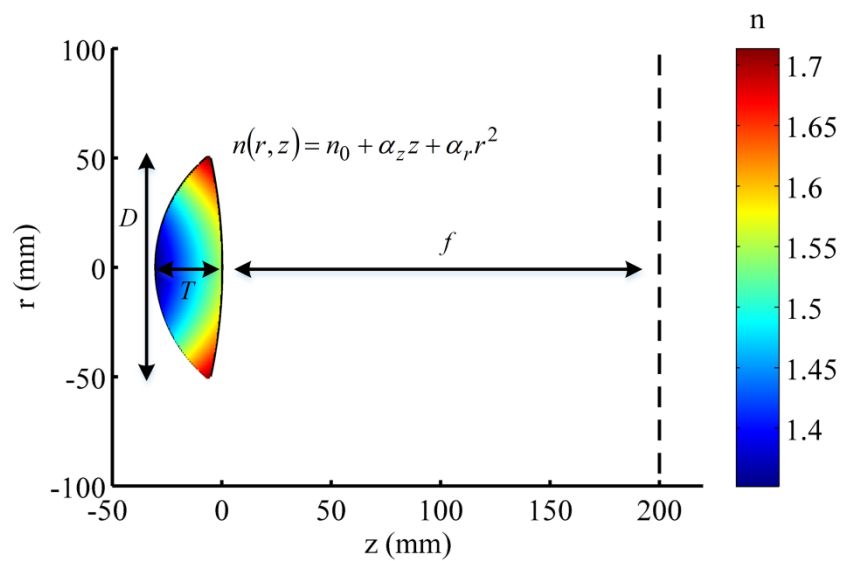
which can be solved for directly once T and the GRIN ratio α_r/α_z are set. Finally, analytical-based corrections thoroughly outlined in [148] were also applied to consider rear principle plane shift and surface sag.

To demonstrate the proposed analytical method, a metamaterial lens with a 100 mm aperture and back focal length of 200 mm, as shown in Fig. 5.8a, was considered. Next, a material system based on [5] was defined in Fig. 5.8b. Material 1 and Material 2 correspond to the low- and high-index components of a potential volume-filling-fraction mixture represented by $n_{Mix} = pn_2 + (1 - p)n_1$, where p is the filling fraction. For comparative purposes, a flat metamaterial lens with a parabolic gradient profile was first considered. The full range of Δn , as defined by Fig. 5.8b, was utilized by adjusting the thickness of the lens, which ended up being 15 mm, until the desired focal length was exhibited for the center frequency f_2 . Simulations for the lowest (f_1), center (f_2), and highest (f_3) frequencies were executed in COMSOL Multiphysics 2D domain. To isolate the dispersive effects associated with the material, the electrical and geometric sizes of the lens were held constant to eliminate any dispersion associated with the aperture. While electrical size of the aperture is large (25λ) and minimal dispersion from the aperture is expected, this phenomenon warrants future considerations. This was done to provide a stronger correlation between the proposed method and resulting dispersion-correction. The simulation results are shown in Fig. 5.9a, indicating that the flat metamaterial lens has a focal drift of about 65%. The focal drift of the flat lens is plotted in Fig. 5.11.

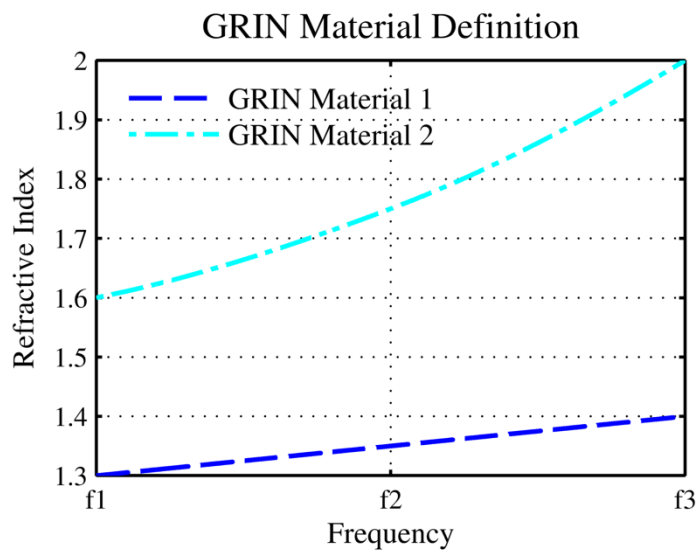
Next, a 2D sweep of lens thickness and α_r/α_z ratios was performed to identify feasible solutions for dispersion-corrected metamaterial lenses. The results from this parametric study are summarized in Fig. 5.10. Upon inspection, a good solution was found corresponding to $T = 30$ mm and $\alpha_r/\alpha_z = -0.5$. The resulting GRIN profile (at f_2) and lens geometry are given in Fig 5.8a. Again, COMSOL was employed to analyze the focal drift of the lens. The small difference between desired and realized focal length and drift is likely due to the small focal length and non-

ideal geometry of the dispersion-corrected metamaterial lens, leading to inaccuracies corresponding to paraxial equations employed. Amongst other techniques, an iterative correction could be applied to adjust the focal length to the desired location. Nevertheless, the uncorrected system demonstrates the design methodology and exhibited a focal drift of only 20%, providing a 3.4x improvement over the flat metamaterial lens.

Finally, intensity plots are provided in Fig. 5.11, comparing the flat metamaterial lens to the dispersion-corrected metamaterial lens and showing that indeed the focal drift is greatly decreased when the proposed method is applied. Fig. 11a corresponds to the 25-lambda aperture lens considered in the above. It is also noticed that unwanted spherical aberrations (*i.e.* oscillations leading up to the peak energy concentration) are introduced when the dispersion correction method. However, this should be easily corrected by applying the asphere-to-sphere technique outlined in section 5.1 or other well-known spherical-aberration correction techniques such as introducing an r^4 -GRIN dependence or aspherical surfaces. Fig. 11b provides the comparison when the same design methodology was applied to a smaller, 5-lambda aperture lens. Due to the reduced size of the lens, larger inaccuracies were found in the focal positions, as well as a reduced dispersion-correction effect. Moving forward, it will be important to determine the effectiveness of the proposed analytical method for reduced aperture sizes where ray-tracing equations may become less accurate. For example, it might be possible to develop a relationship for the focal drift associated with the finite aperture size, which could be included in the achromatic theory and subsequently eliminated. Also, full-wave simulations of lenses composed of real metamaterial structures will be important for further validation.



(a)



(b)

Figure 5.8. (a) Geometry and GRIN profile of metamaterial lens at the center frequency f_2 and (b) dispersive properties of metamaterial.

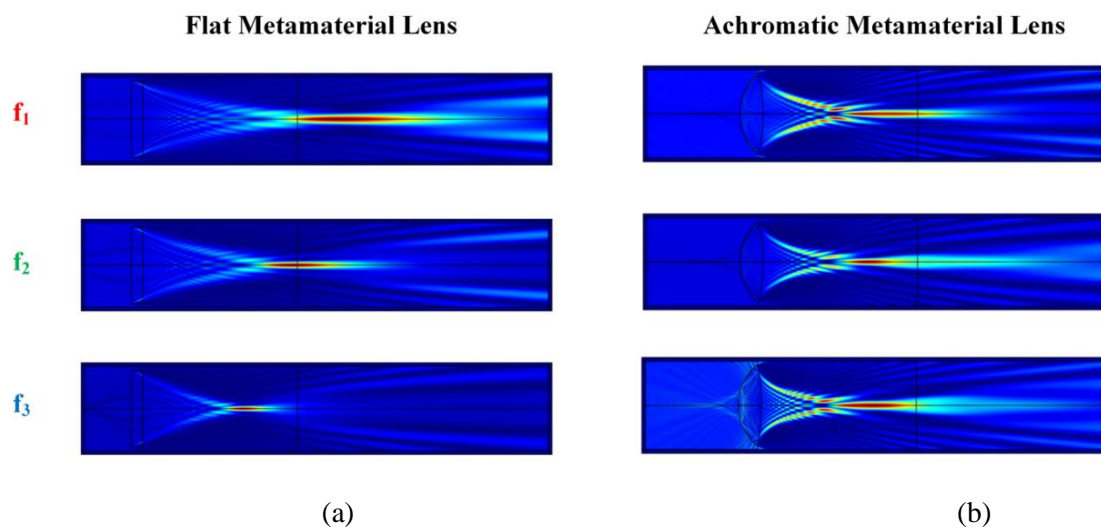


Figure 5.9. (a) COMSOL simulations showing focal drift of flat and (b) dispersion-corrected metamaterial lenses. The black vertical lines mark the targeted focus.

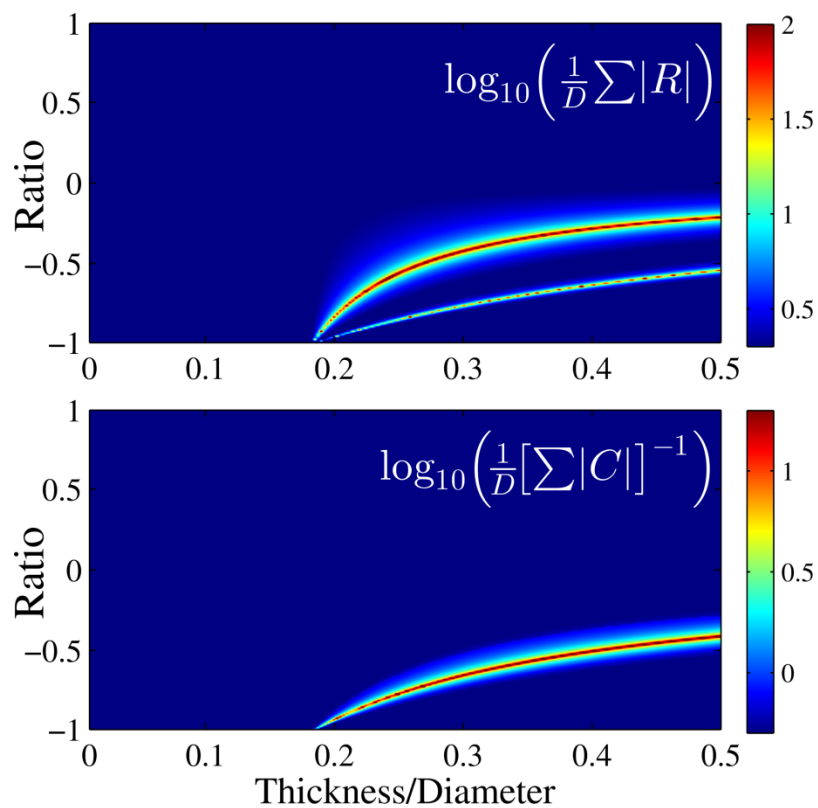


Figure 5.10. Lens surface curvature as a function of GRIN ratio and lens thickness for $f/2.0$ singlet: (top) total surface radii and (bottom) total surface curvature.

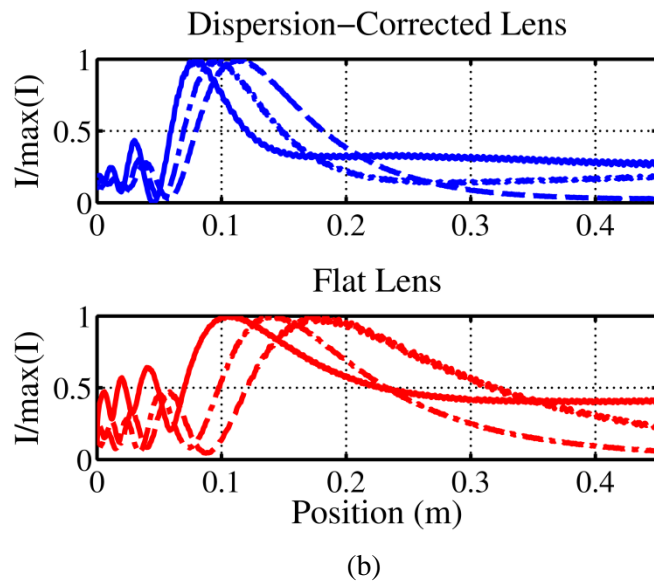
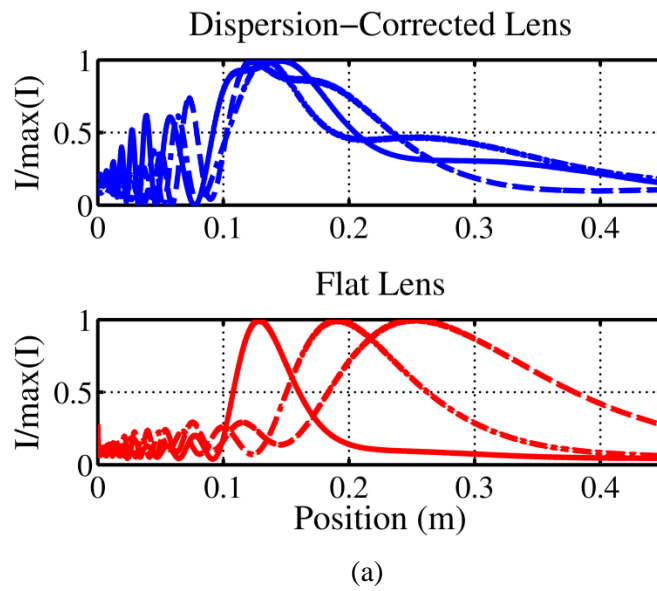


Figure 5.11. Normalized intensity profiles for flat and dispersion-corrected metamaterial lenses with (a) 25-lambda and (b) 5-lambda apertures. Dashed, dash-dot, and solid lines correspond to frequencies 1, 2, and 3, respectively. The plots show a reduced focal drift for the dispersion-corrected lenses.

5.6 Field-of-View Enhancement of Gradient-Index Lenses Inspired by Transformation Optics

So far in this chapter, we have investigated the polychromatic performance of GRIN lenses as well as the monochromatic performance on axis (*i.e.* spherical aberrations). In this subsection, we investigate the oblique incidence performance of GRIN lenses. To motivate this analysis, first consider a GRIN lens known for its superior performance over a large FOV: the Luneburg lens. Moreover, we will consider the version of the Luneburg lens that has been flattened using qTO [39], since flat lenses are typically preferred both from a manufacturing and implementation standpoint. Furthermore, the flattened Luneburg provides a flat focal plane, eliminating field curvature and astigmatism, which are two of the 3rd-order Seidel aberrations. When the qTO routine is applied to flatten the Luneburg lens, the GRIN profile shown in Fig. 5.10a is obtained. Fig. 5.10b shows the result of ray-tracing the flattened Luneburg lens. With an input aperture of 0.25 mm, incidence angles of 0, 15, and 30 degrees all lead to focused RMS spot sizes equal to or less than 10 μm . In classical optics, using homogenous lenses, such performance over such a wide FOV is typically only achieved through the use of multiple lenses, such as in the case of a Cooke triplet.

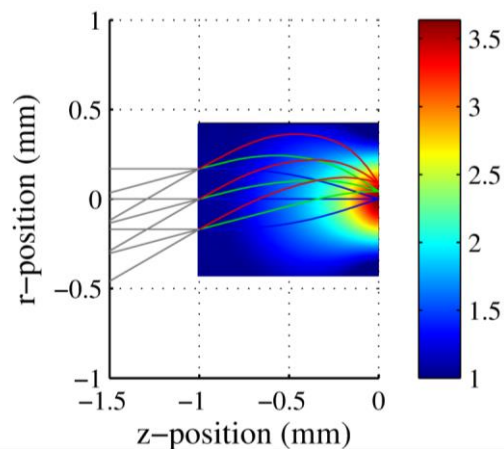


Figure 5.12. Flattened Luneburg lens GRIN profile and ray trace at 0 degrees (blue), 15 degrees (green), and 30 degrees (red).

Now, although the flattened Luneburg is a high performance singlet with extreme FOV, little physical insight has been given into exactly how this is accomplished. In other words, it is not clear how to extend this performance to other lens systems; for example, a lens with a back-focal-length (BFL) greater than zero. Furthermore, the Δn required for the flattened Luneburg is quite large. Is it possible to reduce Δn ? In order to provide a better physical insight, we considered decomposing the flattened Luneburg using a polynomial basis due to the wealth of literature in this area [138]. The general expression for a polynomial GRIN profile is given by

$$\begin{aligned}
 n(r, z) = & (c_{00} + c_{10}r^2 + c_{20}r^4 + c_{30}r^6 + \dots c_{N0}r^{2N}) + \\
 & (c_{01} + c_{11}r^2 + c_{21}r^4 + c_{31}r^6 + \dots c_{N1}r^{2N})z + \\
 & (c_{02} + c_{12}r^2 + c_{22}r^4 + c_{32}r^6 + \dots c_{N2}r^{2N})z^2 + \quad (5.11) \\
 & \vdots \\
 & (c_{0M} + c_{1M}r^2 + c_{2M}r^4 + c_{3M}r^6 + \dots c_{NM}r^{2N})z^M
 \end{aligned}$$

where c_{ij} are the GRIN coefficients and $2N$ and M are the order of the GRIN polynomial with respect to the radial and axial coordinates, respectively. Historically, investigations of GRIN profiles have typically been restricted to purely axial [134, 135, 145, 148] or radial [37, 136, 143, 145, 147, 148, 153], where only the first row and column of GRIN coefficients in (5.11) are nonzero. These basic GRIN profiles can be readily analyzed under thin lens and/or paraxial ray approximations, providing key physical insight into the design of such GRIN lenses. A composition of both axial and radial profiles can be considered, to first order, as a spherical gradient profile and their respective contributions to the overall lens performance can be considered by superposition, where the radial and axial GRIN contributions do not affect the other [148]. This 2-dimensional GRIN profile provides additional degrees of freedom for aberration control, but particularly for a single lens, it is not sufficient to minimize all aberrations. The rest of the terms in (5.11), which will be referred to as “cross-terms”, since that their mixed partial derivatives are generally non-zero.

The flattened Luneburg was first decomposed using simple polynomials; that is, those without cross-terms. The resulting decompositions and resulting ray traces for polynomials up to order 12 are given in Fig. 5.13. More details of this analysis are given in Fig. 5.14, where Fig. 5.14a shows the error in refractive index that the polynomial fitting routine resulted in, Fig. 5.14b shows the foci in the x-y plane, and Fig. 5.14c gives the resulting RMS spot sizes. Clearly, the Luneburg cannot be reproduced with only these simple terms.

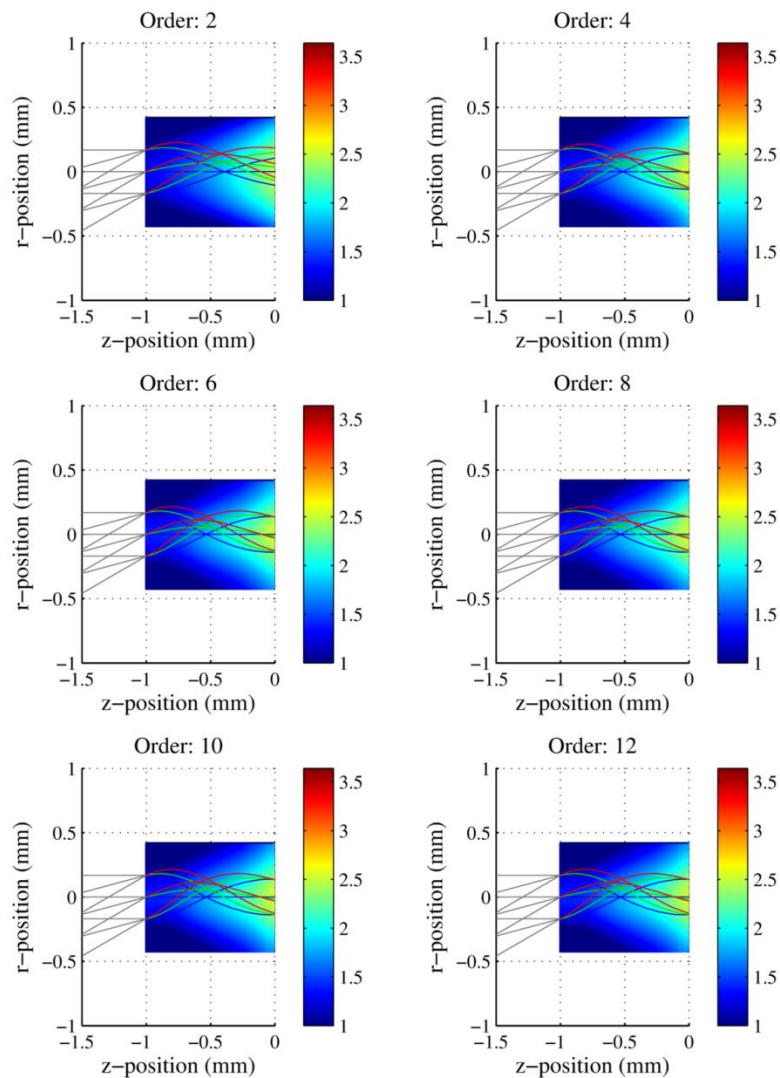


Figure 5.13. Polynomial fitting of flattened Luneburg lens without the use of cross-terms. The order of the polynomial was varied from 2 to 12. Without cross-terms, the polynomial fitting routine cannot reproduce the characteristics of the Luneburg.

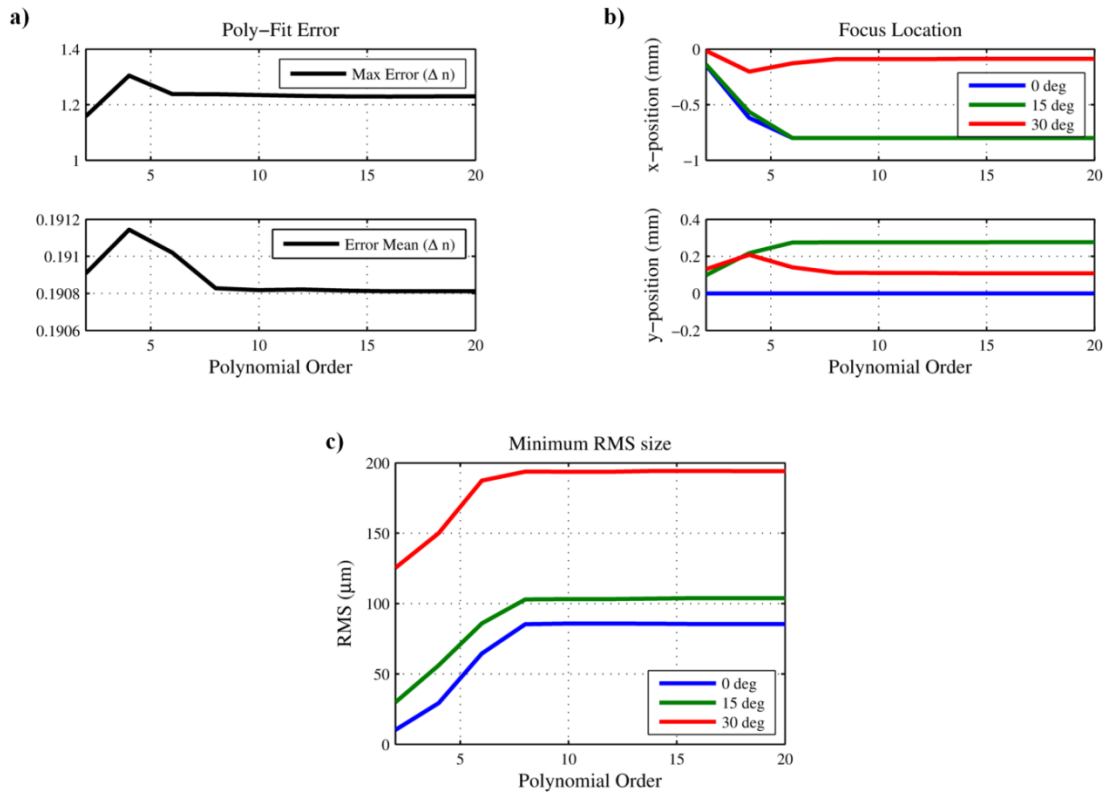


Figure 5.14. Polynomial fitting analysis with no cross-terms: (a) Polynomial fitting maximum and mean error, (b) foci location in the x-y plane at 0, 15, and 30 degrees, and (c) minimum RMS spot size at 0, 15, and 30 degrees. Analyses are functions of polynomial order.

Next, the flattened Luneburg was fitted using polynomials that included cross-terms. This analysis is shown in Figs. 5.15 and 5.16. The resulting polynomial fitting and ray trace show that the cross-terms were necessary to capture the performance of the Luneburg lens. Fig. 5.15 indicates that a polynomial of order 10 to 12 was required for near-exact representation.

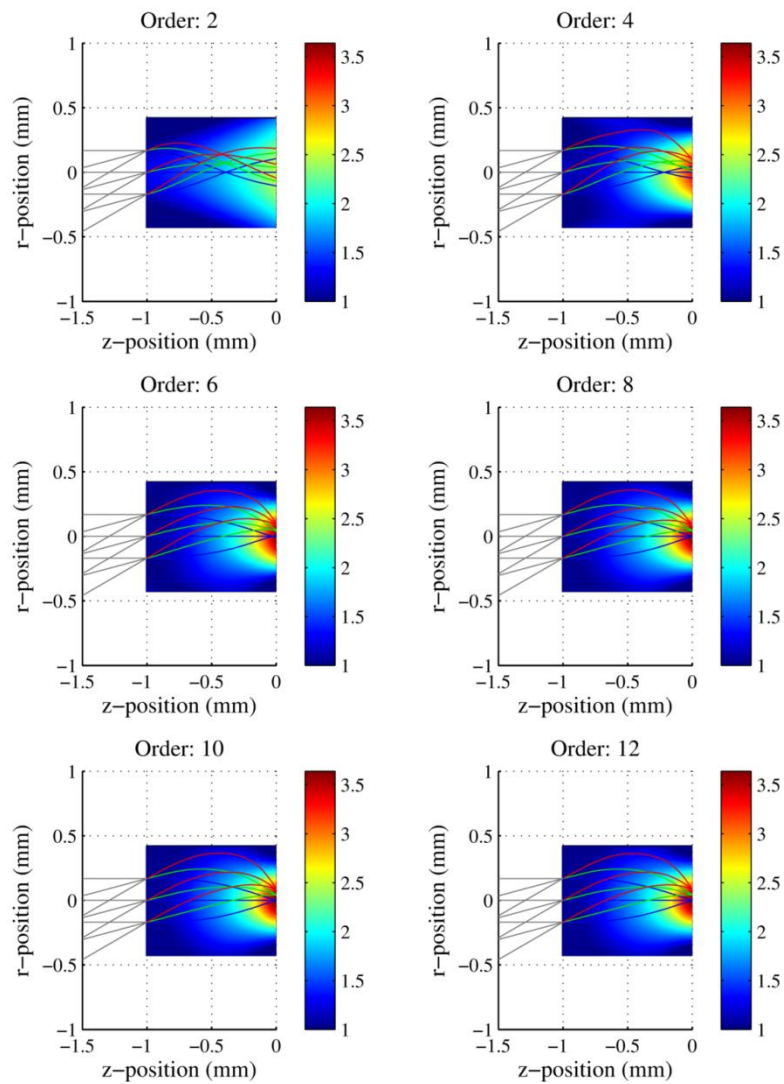


Figure 5.15. Polynomial fitting of flatted Luneburg lens with the use of cross-terms. The order of the polynomial was varied from 2 to 12. The polynomial fitting routine successfully reproduces the characteristics of the Luneburg once cross-terms are introduced.

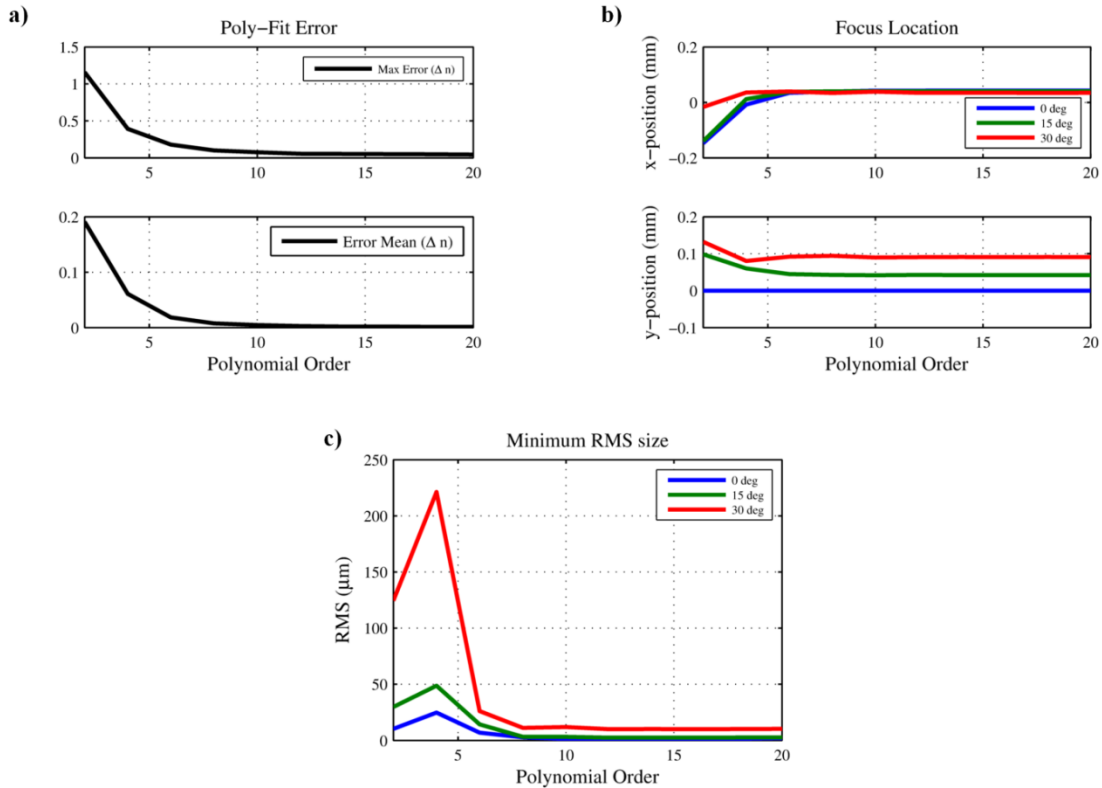


Figure 5.16. Polynomial fitting analysis including cross-terms: (a) Polynomial fitting maximum and mean error, (b) foci location in the x-y plane at 0, 15, and 30 degrees, and (c) minimum RMS spot size at 0, 15, and 30 degrees. Analyses are functions of polynomial order. The polynomial-fitted Luneburg lens converges to diffraction limited performance at approximately order 12.

At this point, the question becomes does the flattened Luneburg, which has good FOV performance, coincidentally also contains a GRIN profile containing cross-terms, *or* is there something fundamentally superior about GRINs with cross-terms? A simple lens system was considered to determine the answer to this question. A single lens system with a 10 mm input aperture, 24 mm BFL, and 10 degree FOV is considered. Multiple lens designs were considered, but fall into the following three general categories: 1) homogeneous, 2) GRIN without cross-terms, and 3) GRIN with cross-terms. The CMA-ES was employed to optimize each lens design using the cost function defined by

$$cost = \sum_{\emptyset} RMS \quad (5.12)$$

where \emptyset are the angles of incidence chosen to be 0, 2, and 5 degrees, representing a 10-degree FOV and RMS is the RMS spot size evaluated at a 24 mm BFL. Fig. 5.17 shows the results from

this study, showing that the GRIN lenses with cross-terms have marginal improvement over the FOV considered.

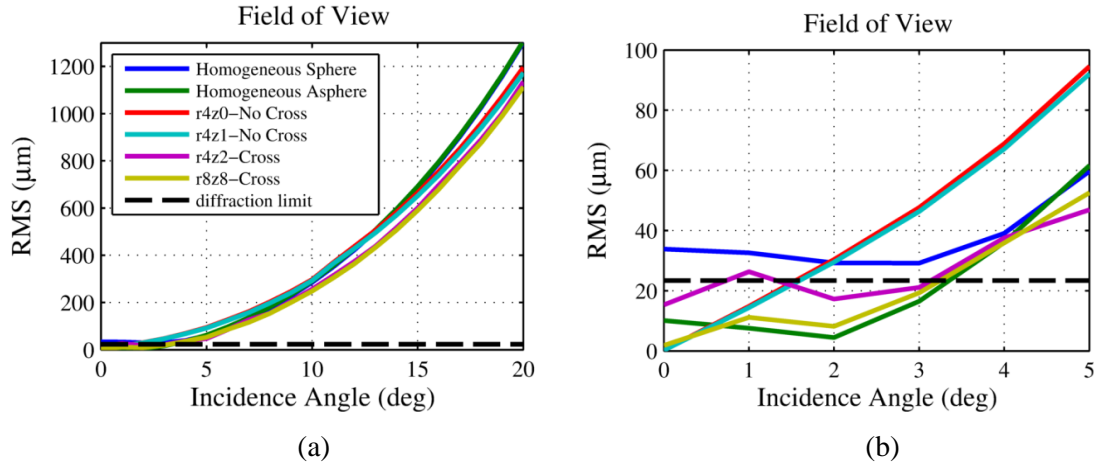


Figure 5.17. Comparison of various lens types over a (a) 20 degree half-FOV and (b) 5 degree half-FOV.

The performance benefits of cross-term GRINs become especially apparent when the optical stop is shifted away from the front of the lens. The effect of doing this translates the entrance and exit pupils of the lens system, and in practice allows the different beams (*i.e.* incident angles) to see slightly different parts of the lens. For this study the same BFL was targeted as before. Several initial studies were performed, which have been left out, but resulted in allocating increased thickness to the GRIN optics; this was done to keep Δn reduced. The thickness of the lens was increased to 10 mm. Also, the aperture size was increased to 25 mm in order to accommodate the shifted stop and, therefore, offset obliquely incident beams. Furthermore, the targeted FOV was increased to 30 degrees. An example of the resulting system geometry is shown in Fig. 5.18a, which shows the chief and marginal ray trajectories for an 8-term radial GRIN that minimized the sum of RMS spots at 0, 5, 10, and 15 degrees. Figure 5.18b shows a zoomed-in perspective of the focal plane, showing strong aberrations, contributing to large spot sizes at the oblique angles. The resulting RMS spot sizes were calculated to be 110, 165, 328, and 518 μm at 0, 5, 10, and 15 degrees, respectively. Next, the same system was optimized when including axial GRIN terms; however, still no cross-terms were introduced. The resulting ray trace is shown in Fig. 5.19 with its GRIN profile. The corresponding spot sizes were calculated to be 108, 154, 328, and 540 μm at 0, 5, 10, and 15 degrees, respectively. That is, no

improvement was demonstrated by the introduction of axial terms. Finally, an 8-cross-term GRIN profile, defined in Fig. 5.20, was optimized over the 30-degree FOV. The resulting GRIN profile had an increased Δn approximately equal to one, but the performance improvement was significant. The spot sizes were calculated to be 26, 46, 65, and 77 μm , which represents almost 4-7x improvement over the FOV considered. Inspection of the focal plane rays in Fig. 5.20b shows that, despite the presence of oblique aberrations, Petzval field curvature and astigmatism have been nearly eliminated.

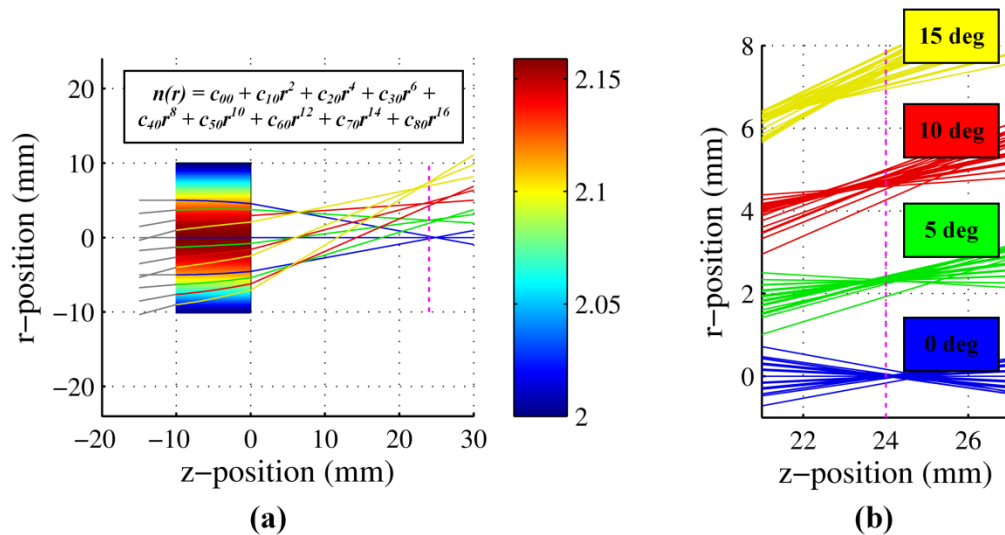


Figure 5.18. Eight-term radial GRIN with significantly improved 30-degree FOV. (a) Ray trace of chief and marginal rays for 0, 5, 10, and 15 degrees incidence. (b) Zoom of 51-ray trace focal plane. Spot sizes were calculated to be 110, 165, 328, and 518 μm at 0, 5, 10, and 15 degrees, respectively.

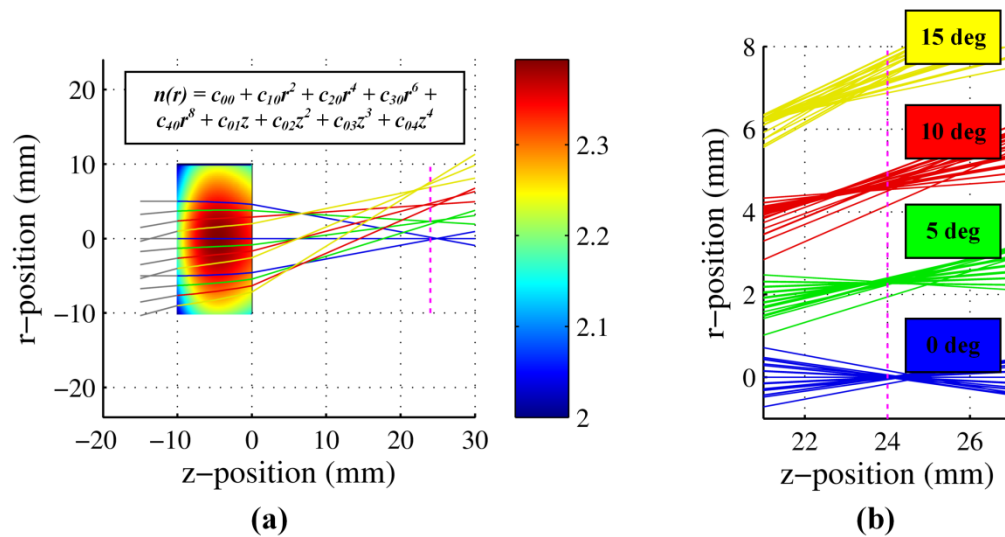


Figure 5.19. Eight-term axial-radial GRIN with significantly improved 30-degree FOV. (a) Ray trace of chief and marginal rays for 0, 5, 10, and 15 degrees incidence. (b) Zoom of 51-ray trace focal plane. Spot sizes were calculated to be 108, 154, 328, and 540 μm at 0, 5, 10, and 15 degrees, respectively.

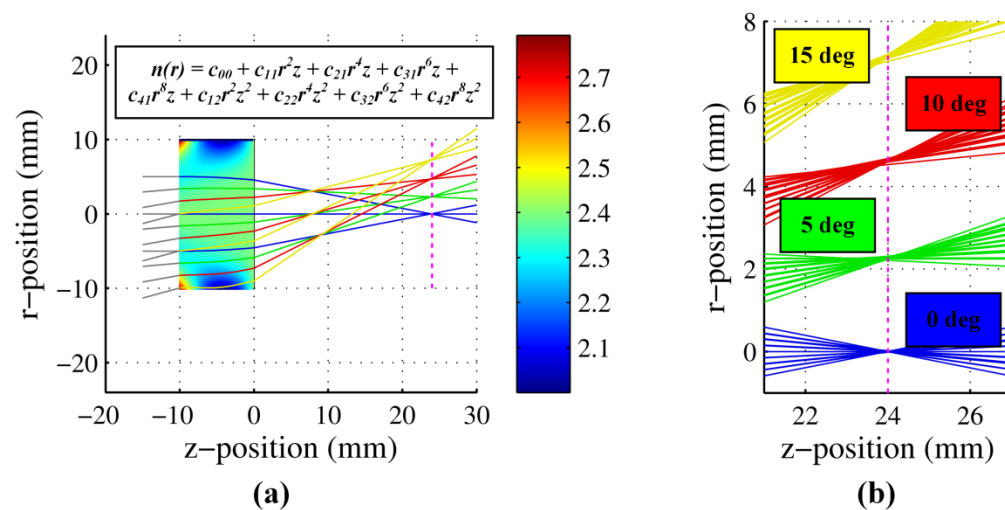


Figure 5.20. Eight-cross-term GRIN with significantly improved 30-degree FOV. (a) Ray trace of chief and marginal rays for 0, 5, 10, and 15 degrees incidence. (b) Zoom of 51-ray trace focal plane. Spot sizes were calculated to be 26, 46, 65, and 77 μm at 0, 5, 10, and 15 degrees, respectively.

Finally, it is worth noting that this section focused on reducing oblique monochromatic aberrations and did not consider polychromatic aberrations. Previous sections in this dissertation have noted that flat geometries may not facilitate color-correction, depending on the GRIN abbe number of the material system used. Color-correction could be an extension of this work for the future.

Chapter 6

Summary and Suggestions for Future Work

6.1 Summary

In this research, methods to facilitate efficient optimization of RF and optical devices were investigated. First, MF propagation in coal mines was modeled using full-wave methods in conjunction with transmission line equations, facilitating a fast and simultaneously accurate modeling tool for electrically large communication networks. This hybrid method was used to propose and optimize a communication network for emergency response applications. Next, a miniaturized dual-band WiFi patch antenna was proposed. The antenna element was subsequently fabricated and characterized, showing excellent agreement with predictions. Furthermore, it was shown that the interdigitated slot loading providing the dual-band nature could be manipulated to independently control the operational frequencies. This and related antenna designs could be utilized in several antenna applications where it is beneficial to exhibit dual-band operation with a miniaturized footprint.

Then, an ultra-thin RF absorber model based on circuit equations was developed. Initially a 2-layer design composed of a HIS loaded by an FSS was developed. An equivalent circuit model was proposed in order to determine the desired frequency response of the FSS. Furthermore, TL equations were applied in order to cascade the FSS and HIS and predict the net absorption. Extremely thin absorbers were found to exhibit coupling between layers that were not accounted for in the basic circuit model. Subsequently, a single-layer design using the same circuit model was developed that decreased the level of parasitic coupling and, as a result, increased the resulting bandwidth for a given absorber thickness. The resulting absorbers

exhibited extremely thin profiles with broad bandwidth while depending only on one structural resonance.

Finally, advanced GRIN lenses were designed via applications of TO, leading to many new exciting lens designs with superior mono- and poly-chromatic characteristics. Asphere-to-sphere transformations were applied to minimize on-axis spherical aberrations with spherically shaped GRIN lenses. Also, a set of TO mappings was proposed to inspire color-corrected GRIN lens design. Lastly, the TO-flattened Luneburg lens was used to inspire flat GRIN lenses with superior FOV performance. The GRIN lens theory developed in this dissertation will provide optical engineers with blueprints for advanced lens design as GRIN materials systems continue to develop and come to fruition.

6.2 Suggestions for Future Work

The research presented in this dissertation can be extended as follows. First, in addition to the TL models utilized in the hybrid approach, more efficient coupling models could be developed to further improve the simulation speed of large communication networks. These approaches could be used to develop robust systems for emergency response applications. For the absorber investigations, an amended circuit model accounting for the coupling between ground plane and FSS would facilitate further thickness reductions. It would also provide an accurate, efficient, and insightful means to analyze the trade-offs between competing performance characteristics, such as bandwidth and thickness. Finally, related to the GRIN lens investigations presented in this dissertation, it is desirable to unify all topics into a single methodology. For example, the extreme-FOV cross-term GRIN lenses were designed at one operational wavelength. The next step would be to combine this theory with the achromatic theory also

discussed. When doing so, there may be limitations and corresponding trade-offs between mono- and poly-chromatic aberration correction that could be analyzed.

Bibliography

- [1] V. G. Veselago, "The electrodynamics of substances with simultaneously negative values of ϵ and μ ," *Sov. Phys. U.*, vol. 10, no. 4, pp. 509-514, Jan. 1968.
- [2] J. B. Pendry, "Negative refraction makes a perfect lens," *Phys. Rev. Lett.*, vol. 85, no. 18, pp. 3966-3969, Oct. 2000.
- [3] R. A. Shelby, D. R. Smith, and S. Schultz, "Experimental verification of a negative index of refraction," *Science*, vol. 292, no. 5514, pp. 77-79, Apr. 2001.
- [4] Capolino, Filippo, *Theory and Phenomena of Metamaterials*, CRC Press, Boca Raton, FL, United States, 2002.
- [5] U. Leonhardt, "Optical conformal mapping," *Science*, vol. 312, no. 5781, pp. 1777-1780, May 2006.
- [6] J. B. Pendry, D. Schurig, and D. R. Smith, "Controlling electromagnetic fields," *Science*, vol. 312, no. 5781, pp. 1780-1782, Jun. 2006.
- [7] D.-H. Kwon and D. H. Werner, "Transformation optical designs for wave collimators, flat lenses and right-angle bends," *New J. Phys.*, vol. 10, pp. 115023(1)-(13), Nov. 2008.
- [8] Schurig, D. et al. "Metamaterial electromagnetic cloak at microwave frequencies," *Science*, vol. 314, no. 5801, pp. 977-980, Nov. 2006.
- [9] J. Li and J. B. Pendry, "Hiding under the carpet: A new strategy for cloaking," *Physical Review Letters*, vol. 101, pp. 203901(1)-(4), Nov. 2008.
- [10] R. Liu, C. Ji, J. J. Mock, J. Y. Chin, T. J. Cui, and D. R. Smith, "Broadband ground-plane cloak," *Science*, vol. 323, no. 5912, pp. 366-369, Jan. 2009.
- [11] M. Rahm, D. Schurig, D. A. Roberts, S. A. Cummer, D. R. Smith, and J. B. Pendry, "Design of electromagnetic cloaks and concentrators using form-invariant coordinate transformations of Maxwell's equations," *Photon. and Nanostruct. – Fundam. and Appl.*, vol. 6, no. 87, pp. 87-95, Apr. 2008.
- [12] E. E. Narimanov and A. V. Kildishev, "Optical black hole: broadband omnidirectional light absorber," *Appl. Phys. Lett.*, vol. 95, 041106(1)-(4), 2009.
- [13] M. Rahm, D. A. Roberts, J. B. Pendry, and D. R. Smith, "Transformation-optical design of adaptive beam bends and beam expanders," *Opt. Express*, vol. 16, no. 15, pp. 11555-11567, Jul. 2008.
- [14] D.-H. Kwon and D. H. Werner, "Polarization splitter and polarization rotator designs based on transformation optics," *Opt. Express*, vol. 16, no. 23, pp. 18731-18738, Nov. 2008.
- [15] D.-H. Kwon and D. H. Werner, "Transformation-optical designs for wave collimators, flat lenses, and right-angle bends," *New J. Phys.*, vol. 10, pp. 115023(1)-(13), 2008.
- [16] W. Tang, C. Argyropoulos, E. Kallos, W. Song, and Y. Hao, "Discrete coordinate transformation for designing all-dielectric flat antennas," *IEEE Trans. Antennas and Propagat.*, vol. 58, no. 12, pp. 3795-3804, Dec. 2010.
- [17] B. Arigong, J. Shao, H. Ren, G. Zheng, J. Lutkenhaus, H. S. Kim, Y. Lin, and H. Zhang, "Reconfigurable surface plasmon polariton wave adapter designed by transformation optics," *Opt. Express*, vol. 20, no. 13, pp. 13789-13797, Jun. 2012.
- [18] J. H. Holland, "Genetic algorithms and the optimal allocation of trials," *SIAM J. Comput.*, vol. 2, no. 2, Jun. 1973.
- [19] D. S. Weile and E. Michielssen, "Genetic algorithm optimization applied to electromagnetics: A review," *IEEE Trans. Antennas Propagat.*, vol. 45, pp. 343-353, Mar. 1997.

- [20] R. L. Haupt and D. H. Werner, *Genetic Algorithms in Electromagnetics*. Hoboken, NJ: Wiley, 2007.
- [21] J. Kennedy and R. Eberhart, "Particle swarm optimization," in *Proc. 9th Int. Conf. on Neural Networks*, vol. 4, pp. 1942–1948, Nov. 1995.
- [22] R. Eberhart and J. Kennedy, "A new optimizer using particle swarm theory," in *IEEE Proc. 6th Int. Symp. on Micro Machine and Human Science*, pp. 39–43, Oct. 1995.
- [23] J. Robinson and Y. Rahmat-Samii, "Particle swarm optimization in electromagnetics," *IEEE Trans. Antennas Propagat.*, vol. 52, pp. 397–407, Feb. 2004.
- [24] R. Storn and K. Price, "Differential evolution—A simple and efficient heuristic for global optimization over continuous spaces," *J. Global Opt.*, vol. 11, no. 4, pp. 341–359, Dec. 1997.
- [25] K. V. Price, R. M. Storn, and J. A. Lampinen, *Differential Evolution: A Practical Approach to Global Optimization*, in *Natural Computing*. Heidelberg: Springer-Verlag, 2005.
- [26] N. Hansen and A. Ostermeier, "Completely derandomized self-adaptation in evolutionary strategies," *Evol. Comput.*, vol. 9, no. 2, pp. 196–195, 2001.
- [27] N. Hansen, S. D. Müller, and P. Koumoutsakos, "Reducing the time complexity of the derandomized evolution strategy with covariance matrix adaptation (CMA-ES)," *Evol. Comput.*, vol. 11, no. 1, pp. 1–18, 2003.
- [28] M. D. Gregory, Z. Bayraktar, and D. H. Werner, "Fast optimization of electromagnetic design problems using the covariance matrix adaptation evolutionary strategy," *IEEE Trans. on Antennas and Propag.*, vol. 59, no. 4, pp. 1275-1285, Apr. 2001.
- [29] D. E. Brocker, P. E. Sieber, J. A. Waynert, J. Li, P. L. Werner, and D. H. Werner, "A hybrid approach for efficient modeling of medium-frequency propagation in coal mines," *IEEE Ant. Propag. Mag.*, vol. 57, no. 1, pp. 164-176, Feb. 2015.
- [30] Nicholas Damiano, Jingcheng Li, Chenming Zhou, Donovan E. Brocker, Yifeng Qin, Douglas H. Werner, and Pingjuan L. Werner, "Simulation and measurement of medium frequency signals coupling from a line to a loop antenna," Accepted for publication in *IEEE Trans. Ind.*
- [31] D. E. Brocker, P. L. Werner, D. H. Werner, J. Waynert, J. Li, N. W. Damiano, "Characterization of medium frequency propagation on a twin-lead transmission line with earth return," *Proc. IEEE Antennas Propag. Soc. Int. Symp.*, pp. 1-2, Jul. 2012.
- [32] D. E. Brocker, D. H. Werner, and P. L. Werner, "Dual-band shorted patch antenna with significant size reduction using a meander slot," *Proc. IEEE Antennas Propag. Soc. Int. Symp.*, pp. 1-2, Jul. 2014.
- [33] D. E. Brocker, Z. H. Jiang, M. D. Gregory, and D. H. Werner, "Miniaturized dual-band folded patch antenna with independent band control utilizing an interdigitated slot loading," submitted to *IEEE Trans. on Antennas Propagat.*
- [34] A. H. Panaretos, D. E. Brocker, and D. H. Werner, "Ultra-thin absorbers comprised by cascaded high-impedance and frequency selective surfaces," *IEEE Antennas Wireless Propagat. Lett.*, vol. 14, pp. 1089-1092, Jan. 2015.
- [35] D. E. Brocker, J. P. Turpin, P. L. Werner, and D. H. Werner, "Optimization of gradient index lenses using quasi-conformal contour transformations," *IEEE Antennas Wireless Propagat. Lett.*, vol. 13, pp. 1787-1791, Jan. 2014.
- [36] D. E. Brocker, S. D. Campbell, J. Nagar, and D. H. Werner, "Transformation optics-inspired dispersion-corrected gradient-index lens design," *Proc. IEEE Antennas Propag. Soc. Int. Symp.*, pp. 1-2, Jun./Jul. 2016.

- [37] D. E. Brocker, S. D. Campbell, and D. H. Werner, "Color-correcting gradient-index infrared singlet based on silicon and germanium mixing," *Proc. IEEE Antennas Propag. Soc. Int. Symp.*, pp. 1-2, Jul. 2015.
- [38] D. E. Brocker, S. D. Campbell, D. H. Werner, and P. L. Werner, "An analytical design methodology for dispersion-corrected metamaterial lenses," *Proc. IEEE Antennas Propag. Soc. Int. Symp.*, pp. 1-2, Jun./Jul. 2016.
- [39] N. Kundtz and D. R. Smith, "Extreme-angle broadband metamaterial lens," *Nat. Mat.*, vol. 9, no. 12, pp. 129-132, Dec. 2009.
- [40] J. N. Murphy and H. E. Parkinson, "Underground mine communications," *Proc. IEEE*, vol. 66, 1, pp. 26-50, Jan. 1978.
- [41] L. K. Bandyopadhyay, S. K. Chaulya, P. K. Mishra, *Wireless Communication in Underground Mines: RFID-based Sensor Networking*, New York, Springer, 2009.
- [42] W. H. Schiffbauer and J. F. Brune, "Coal mine communications," *American Longwall Magazine*, pp. 24-25, 2006.
- [43] A. E. Forooshani, S. Bashir, D. G. Michelson, and S. Noghianian, "A survey of wireless communications and propagation modeling in underground mines," *IEEE Comm. Surv. Tut.*, vol. 15, no. 4, pp. 1524-1545, Fourth Quarter 2013.
- [44] S. Yarkan, S. Guzelgoz, H. Arslan, and R. R. Murphy, "Underground mine communications: a survey," *IEEE Comm. Surv. Tut.*, vol. 11, no. 3, pp. 135-142, Third Quarter 2009.
- [45] D. G. Dudley, M. Lienard, S. F. Mahmoud, and P. Degauque, "Wireless propagation in yunnels," *IEEE Antennas Propag. Mag.*, vol. 49, no. 2, pp. 11-26, Apr. 2007.
- [46] A. G. Emslie, R. L. Lagace, and P. F. Strong, "Theory of the propagation of UHF radio waves in coal mines tunnels," *IEEE Trans. Antennas Propagat.*, vol. 23, no. 2, pp. 192-205, Mar. 1975.
- [47] P. Delogne, "EM propagation in tunnels," *IEEE Trans. Antennas Propagat.*, vol. 39, no. 3, pp. 401-406, Mar. 1991.
- [48] Y. P. Zhang, G. X. Zheng, and J. H. Sheng, "Radio propagation at 900 MHz in underground coal mines," *IEEE Trans. Antennas Propagat.*, vol. 49, no. 5, pp. 757-762, May 2001.
- [49] Y. P. Zhang, "Novel model for propagation loss prediction in tunnels," *IEEE Trans. on Veh. Techn.*, vol. 52, no. 5, pp. 1308-1314, Sept. 2003.
- [50] M. Boutin, A. Benzakour, C. L. Despins, and S. Affes, "Radio wave characterization and modeling in underground mine tunnels," *IEEE Trans. Antennas Propagat.*, vol. 56, no. 2, pp. 540-549, Feb. 2008.
- [51] S. F. Mahmoud, "Modal propagation of high frequency electromagnetic waves in Straight and curved tunnels within the earth," *J. Electromag. Waves Appl.*, vol. 19, no. 12, pp. 1611-1627, Apr. 2005.
- [52] Z. Sun and I. Akyildiz, "Channel modeling and analysis for wireless networks in underground mines and road tunnels," *IEEE Trans. Comm.*, vol. 58, no. 6, pp. 1758-1768, Jun. 2010.
- [53] C. L. Holloway, D. A. Hill, R. A. Dalke, and G. A. Hufford, "Radio wave propagation characteristics in lossy circular waveguides such as yunnels, mine shafts and boreholes," *IEEE Trans. Antennas Propagat.*, vol. 48, no. 9, pp. 1354-1366, Sep. 2000.
- [54] D. G. Dudley and S. F. Mahmoud, "Linear source in a circular tunnel," *IEEE Trans. Antennas Propagat.*, vol. 54, no. 7, pp. 2034-2047, Jul. 2006.
- [55] D. A. Hill and J. R. Wait, "Theoretical noise and propagation models for through-the-earth communications," U.S. Bureau of Mines, Contract No. J0113058, May 1982.

- [56] J. A. Durkin, "Apparent earth conductivity over coal mines as estimated from through-the-earth electromagnetic transmission tests," U.S. Bureau of Mines, Report of Investigations 8869 NTIS PB84-213792, 1984.
- [57] W. Pittman, R. Church, and J. T. McLendon, "Through-the-earth electromagnetic trapped miner location systems: a review," U.S. Bureau of Mines, 1985.
- [58] T. D. Barkand, N. W. Damiano, and W. A. Shumaker, "Through-the-earth, two-way, mine emergency, voice communication system," *IEEE Ind. Appl. Conf.*, pp. 955-958, Oct. 2006.
- [59] L. Yan, J. A. Waynert, and C. Sunderman, "Measurements and modeling of through-the-earth communications for coal mines," *IEEE Trans. Ind. Appl.*, vol. 49, no. 5, pp. 1979-1983, Sep./Oct. 2013.
- [60] T. S. Cory, "Antenna design and coupling studies at medium frequency for improved coal mine communications," U.S. Bureau of Mines, Purchase Order No. PO382223, Dec. 1978.
- [61] H. K. Sacks, and R. L. Chufo, "Medium-frequency propagation in coal mines," *4th WVU Conf. Coal Mine Electrotech.*, pp. 27(1)-(12), Aug. 1978.
- [62] R. L. Chufo, "Medium frequency mine communications," *28th IEEE Veh. Tech. Conf.*, pp. 261-266, Mar. 1978.
- [63] L. G. Stolarczyk, "A medium frequency wireless communication system for underground mines," U.S. Bureau of Mines, Contract No. H0308004, Sep. 1984.
- [64] R. L. Lagace, D. A. Curtis, J. D. Foulkes, and J. L. Rothery, "Transmit antennas for portable VLF to MF wireless mine communications," U.S. Bureau of Mines, Contract No. H0346045, May 1977.
- [65] H. H. Dobroski, and L. G. Stolarczyk, "Whole-mine medium-frequency radio communication system," *6th WVU Conf. Coal Mine Electrotech.*, pp. 124-136, Jul. 1982.
- [66] R. L. Lagace, A. G. Emslie, M. A. Grossman, and A. D. Little Inc., "Modeling and data analysis of 50 to 5000 kHz radio wave propagation in coal mines," U.S. Bureau of Mines, Contract No. H0346045, Feb. 1980.
- [67] T. S. Cory, "Propagation of EM signal in underground mines," U.S. Bureau of Mines, Contract No. H0366028, Aug. 1977.
- [68] T. S. Cory, "Electromagnetic propagation in low coal mines at medium frequencies," U.S. Bureau of Mines, Contract No. H0377053, Jun. 1978.
- [69] L. G. Stolarczyk, "Emergency and operational low and medium frequency band radio communications system for underground mines," *IEEE Trans. Ind. Appl.*, vol. 27, no. 4, pp. 780-790, Jul./Aug. 1991.
- [70] A. G. Emslie, and R. L. Lagace, "Propagation of low and medium frequency radio waves in a coal seam," *Radio Sci.*, vol. 11, no. 4, pp. 253-261, Apr. 1976.
- [71] D. A. Hill, "Electromagnetic Wave propagation in an asymmetrical coal seam," *IEEE Trans. Antennas Propagat.*, vol. 34, no. 2, pp. 244-247, Feb. 1986.
- [72] T. Novak, D. P. Snyder, and J. L. Kohler, "Postaccident mine communications and tracking systems," *IEEE Trans. Ind. Appl.*, vol. 46, no. 2, pp. 712-719, Mar./Apr. 2010.
- [73] D. E. Brocker, P. L. Werner, D. H. Werner, J. Waynert, J. Li, and N. W. Damiano, "Characterization of medium frequency propagation on a twin-lead line with earth return," *Proc. IEEE Antennas Propag. Soc. Int. Symp.*, pp. 1-2, Jul. 2012.
- [74] D. E. Brocker, J. Waynert, J. Li, N. W. Damiano, D. H. Werner, and P. L. Werner, "Modeling of medium frequency propagation experiments at the NIOSH safety research coal mine," *ACES Int. Rev. Prog. Appl. Comput. Electromag.*, pp. 1-6, Mar. 2013.

- [75] J. Li, J. A. Waynert, and B. G. Whisner, "An introduction to a medium frequency propagation characteristic measurement method of a transmission line in under-ground coal mines," *Prog. Electromag. Research B*, vol. 55, pp. 131-149, Sep. 2013.
- [76] J. Li, B. Whisner, and J. A. Waynert, "Measurements of medium frequency propagation characteristics of a transmission line in an underground coal mine," *IEEE Ind. Appl. Soc. An. Meeting*, pp. 1-8, Oct. 2012.
- [77] J. A. Brandao Faria, "Approximate evaluation of the wave propagation parameters of MF TL communication systems for mine tunnels using image theory," *J. Electromag. Waves Appl.*, vol. 28, no. 4, pp. 515-530, Jan. 2014.
- [78] J. A. Brandao Faria, "Accurate electromagnetic analysis of MF TL backup communications in cylindrical tunnels," *IEEE Trans. Antennas Propagat.*, vol. 63, no. 5, pp. 2032-2040, May 2015.
- [79] D. A. Hill, and J. R. Wait, "Excitation of monofilar and bifilar modes on a transmission line in a circular tunnel," *J. Appl. Phys.*, vol. 45, no. 8, pp. 3402-3406, August 1974.
- [80] S. F. Mahmoud, "On the attenuation of monofilar and bifilar modes in mine tunnels," *IEEE Trans. Microw. Theory Tech.*, vol. 22, no. 9, pp. 845-847, Sept. 1974.
- [81] S. F. Mahmoud, and J. R. Wait, "Calculated channel characteristics of a braided coaxial cable in a mine tunnel," *IEEE Trans. Comm.*, vol. 24, no. 1, pp. 82-87, Jan. 1976.
- [82] C. R. Paul, *Analysis of Multiconductor Transmission Lines*, 2nd ed., New York, John Wiley, 2007.
- [83] M. D'Amore, and M. S. Sarto, "Simulation models of a dissipative transmission line above a lossy ground for a wide-frequency range—part II: multiconductor configuration," *IEEE Trans. Elec. Compat.*, vol. 38, no. 2, pp. 139-149, May 1996.
- [84] A. Dounavis, R. Achar, and M. Nakhla, "A general class of passive macromodels for lossy multiconductor transmission lines," *IEEE Trans. Microw. Theory Tech.*, vol. 49, no. 10, pp. 1686-1696, Oct. 2001.
- [85] S. F. Mahmoud, and J. R. Wait, "Theory of wave propagation along a thin wire inside a rectangular waveguide," *Radio Sci.*, vol. 9, no. 3, pp. 417-420, Mar. 1974.
- [86] J. R. Wait, "Theory of wave propagation along a thin wire parallel to an interface," *Radio Sci.*, vol. 7, no. 6, pp. 675-679, Jun. 1972.
- [87] D. M. Pozar, *Microwave engineering*, 2nd ed., New York, John Wiley, 1998.
- [88] M. D'Amore, and M. S. Sarto, "Simulation models of a dissipative transmission line above a lossy ground for a wide-frequency range—part I: single conductor configuration," *IEEE Trans. Electro. Compat.*, vol. 38, no. 2, pp. 127-138, May 1996.
- [89] J. R. Carson, "Wave propagation in overhead wires with a ground return," *Bell System Tech. J.*, vol. 5, pp. 539-554, Oct. 1926.
- [90] R. L. King, H. W. Hill, Jr., R. R. Bafanna, and W. L. Cooley. "Guide for the construction of driven-rod ground belts," U.S. Bureau of Mines, Information Circular 8767, 1978.
- [91] J. L. Volakis, C.-C. Chen, and K. Fujimoto, *Small antennas: miniaturization techniques and applications*, 1st ed., New York: McGraw-Hill, 2010.
- [92] K. Fujimoto and J. R. James, Eds., *Mobile antenna systems handbook*, 2nd ed., Boston, MA: Artech House, 2001.
- [93] K. F. Lee and K. M. Luk, *Microstrip patch antennas*, 1st ed., London, UK: Imperial College Press, 2010.
- [94] K. M. Luk, R. Chair, and K. F. Lee, "Small rectangular patch antenna," *Electron. Lett.*, vol. 34, no. 25, pp. 2366-2367, Dec. 1998.
- [95] K. L. Wang and K. P. Yang, "Modified planar inverted F antenna," *Electron. Lett.*, vol. 34, no. 1, pp. 7-8, Jan. 1998.

- [96] H. K. Kan and R. B. Waterhouse, "Size reduction technique for shorted patches," *Electron. Lett.*, vol. 35, pp. 948–949, Jun. 1999.
- [97] R. Waterhouse, "Small microstrip patch antenna," *Electron. Lett.*, vol. 31, no. 8, pp. 604–605, Apr. 1995.
- [98] R. Li, G. DeJean, M. M. Tentzeris, and J. Laskar, "Development and analysis of a folded shorted-patch antenna with reduced size," *IEEE Trans. Antennas Propagat.*, vol. 52, pp. 555–562, Feb. 2004.
- [99] A. Holub and M. Polivka, "Vertically meander-folded, shorted-patch antennas," *Microw. Opt. Technol. Lett.*, vol. 51, no. 12, pp. 2938–2942, Dec. 2009.
- [100] X.-X. Zhang and F. Yang, "Study of a slit cut on a microstrip antenna and its applications," *Micro. and Opt. Tech. Lett.*, vol. 18, no. 4, pp. 297–300, Jul. 1998.
- [101] Y. Hwang, Y. P. Zhang, G. X. Zheng, and T. K. C. Lo, "Planar inverted F antenna with high permittivity material," *Electron. Lett.*, vol. 31, no. 20, pp. 1710–1712, Sept. 1995.
- [102] S. N. Das and S. K. Chowdhury, "Rectangular microstrip antenna on a ferrite substrate," *IEEE Trans. Antennas Propagat.*, vol. AP-30, no. 3, pp. 499–502, May 1982.
- [103] A. D. Brown and J. L. Volakis, "Patch antennas on ferromagnetic substrate," *IEEE Trans. Antennas Propagat.*, vol. 47, no. 1, pp. 26–32, Jan. 1999.
- [104] K. Buell, H. Mosallaei, and K. Sarabandi, "A substrate for small patch antennas providing tunable miniaturization factors," *IEEE Trans. on Microw. Theory Tech.*, vol. 54, no. 1, pp. 135–146, Jan. 2006.
- [105] A. Alu, F. Bilotti, N. Engheta, and L. Vegni, "Subwavelength, compact, resonant patch antennas loaded with metamaterials," *IEEE Trans. Antennas Propagat.*, vol. 55, no. 1, pp. 13–25, Jan. 2007.
- [106] Y. Dong, H. Toyao, and T. Itoh, "Compact circularly-polarized patch antenna loaded with metamaterial structures," *IEEE Trans. Antennas Propagat.*, vol. 59, no. 11, pp. 4329–4333, Nov. 2011.
- [107] S. A. Long and W. D. Walton, "A dual-frequency stacked microstrip circular-disc antenna," *IEEE Trans. Antennas Propagat.*, vol. 27, no. 2, pp. 270–273, Mar. 1979.
- [108] S. Maci, G. Biffi Gentili, P. Piazzesi, and C. Salvador, "Dual-band slot-loaded patch antenna," *Proc. Inst. Elect. Eng. Microw. Antennas Propagat.*, vol. 142, no. 3, pp. 225–232, Jun. 1995.
- [109] K. F. Lee, K. M. Luk, K. F. Tong, S. M. Shwn, T. Huynh, and R. Q. Lee, "Experimental and simulation studies of the coaxially fed U-slot rectangular patch antenna," *Proc. Inst. Elect. Eng. Microw. Antennas Propagat.*, vol. 144, no. 5, pp. 354–358, Oct. 1997.
- [110] K-F. Liew, S. L. S. Yang, and A. A. Kishk, "Dual- and multiband U-slot patch antennas," *IEEE Antennas Wireless Propag. Lett.*, vol. 7, pp. 645–647, 2008.
- [111] J. Ollikainen, M. Fischer, and P. Vainikainen, "Thin dual-resonant stacked shorted patch antenna for mobile communications," *Electron. Lett.*, vol. 35, no. 6, pp. 437–438, Mar. 1999.
- [112] Y. X. Guo, K. M. Luk, and K. F. Lee, "Dual-band slot-loaded short-circuited patch antenna," *Electron. Lett.*, vol. 36, no. 4, pp. 289–291, Feb. 2000.
- [113] K. L. Lau, K. C. Kong, and K. M. Luk, "A miniature folded shorted patch antenna for dual-band operation," *IEEE Trans. Antennas Propagat.*, vol. 55, no. 8, pp. 2391–2398, Aug. 2007.

- [114] C. Y. Chiu, C. H. Chan, and K. M. Luk, "Small dual-band antenna with folded-patch technique," *IEEE Antennas Wireless Propagat. Lett.*, vol. 3, pp. 108-110, 2004.
- [115] J.-H. Lu and K. L. Wong, "Slot-loaded, meandered rectangular microstrip antenna with compact dual-frequency operation," *Electron. Lett.*, vol. 34, no. 11, pp. 1048-1050, May 1998.
- [116] W. C. Liu and W. R. Chen, "CPW-fed compact meandered patch antenna for dual-band operation," *Electron. Lett.*, vol. 40, no. 18, pp. 1094-1095, Sep. 2004.
- [117] H. T. Chen, K. L. Wong, and T. W. Chio, "PIFA with a meandered and folded patch for the dual-band mobile phone application," *IEEE Trans. Antennas Propagat.*, vol. 51, no. 9, pp. 2468-2471, Sep. 2003.
- [118] P. Ciaia, R. Staraj, G. Kossivas, and C. Luxey, "Design of an internal quad-band antenna for mobile phones," *IEEE Microw. Wireless Comp. Lett.*, vol. 14, no. 4, pp. 148-150, Apr. 2004.
- [119] D. E. Brocker, D. H. Werner, and P. Werner, "Dual-band shorted patch antenna with significant size reduction using a meander slot," *Proc. IEEE Antennas Propag. Soc. Int. Symp.*, pp. 1-2, Jul. 2014.
- [120] J. Oh and K. Sarabandi, "Low profile, miniaturized, inductively coupled capacitively loaded monopole antenna," *IEEE Trans. Antennas Propagat.*, vol. 60, no. 3, pp. 1206-1213, Mar. 2012.
- [121] D. J. Kern, D. H. Werner, A. Monorchio, L. Lanuzza, and M. J. Wilhelm, "The design synthesis of multi-band artificial magnetic conductors using high impedance frequency selective surfaces," *IEEE Trans. Antennas Propagat.*, vol. 53, no. 1, pp. 8-17, Jan. 2005.
- [122] F. Yang, and R. Rahmat-Samii, *Electromagnetic band gap structures in antenna engineering*, Cambridge University Press, 2009.
- [123] N. Engheta, "Thin absorbing screens using metamaterial surfaces," *Proc. IEEE Antennas Propag. Soc. Int. Symp.*, vol. 2, pp. 392-395, 2002.
- [124] D. J. Kern, and D. H. Werner, "A genetic algorithm approach to the design of ultra-thin electromagnetic bandgap absorbers," *Microw. Opt. Techn. Lett.*, vol. 38, no. 1, pp. 61-64, Jul. 2003.
- [125] R. E. Diaz, V. Sanchez, E. Caswell, and A. Miller, "Magnetic loading of artificial magnetic conductors for bandwidth enhancement," *Proc. IEEE Antennas Propag. Soc. Int. Symp.*, vol. 2, pp. 431-434, Jun. 2003.
- [126] D. J. Kern, and D. H. Werner, "Magnetic loading of EBG AMC ground planes and ultra-thin absorbers for improved bandwidth performance and reduced size," *Microw. Opt. Techn. Lett.*, vol. 48, no. 12, pp. 2468-2471, Dec. 2006.
- [127] M. Li, S. Xiao, Y.-Y. Bai, and B.-Z. Wang, "An ultrathin and broadband radar absorber using resistive FSS," *IEEE Antennas Wireless Propagat. Lett.*, vol. 11, pp. 748-751, 2012.
- [128] R. Ulrich, "Far-infrared properties of metallic mesh and its complementary structure," *Infrared Phys.*, vol. 7, pp. 37-55, 1967.
- [129] J. A. Arnaud and F. A. Pelow, "Resonant-grid quasi-optical diplexers," *The Bell Sys. Tech. J.*, vol. 54, no. 2, pp. 263-283, Feb. 1975.
- [130] J. F. Thompson, B. K. Soni, and N. P. Weatherill, *Handbook of grid generation*, CRC Press, 1999.
- [131] Q. Wu, J. P. Turpin, and D. H. Werner, "Integrated photonic systems based on transformation optics enabled gradient index devices," *Light: Sci. and Appl.*, vol. 1, no. e38, Nov. 2012.

- [132] N. Kundtz and D. R. Smith, "Extreme-angle broadband metamaterial lens," *Nat. Mat.*, vol. 9, no. 129, Dec. 2009.
- [133] H. F. Ma and T. J. Cui, "Three-dimensional broadband and broad-angle transformation-optics lens," *Nat. Comm.*, vol. 1, no. 124, Nov. 2010.
- [134] P. J. Sands, "Third-order aberrations of inhomogeneous lenses," *J. Opt. Soc. Am.*, vol. 60, no. 11, pp. 1436-1443, Nov. 1970.
- [135] D. T. Moore, "Catadioptric system with a gradient-index corrector plate," *J. Opt. Soc. Am.*, vol. 67, no. 9, pp. 1143-1146, Sep. 1977.
- [136] D. T. Moore, "Design of singlets with continuously varying indices of refraction," *J. Opt. Soc. Am.*, vol. 61, no. 7, pp. 886-894, Jul. 1971.
- [137] D. T. Moore, "Gradient-index optics: a review," *Appl. Opt.*, vol. 19, no. 7, pp. 1035-1038, Apr. 1980.
- [138] E. W. Marchand, *Gradient index optics*, Academic Press, 1978.
- [139] R. E. Fischer, B. Tadic-Galeb, P. R. Yoder, and R. Galeb, *Optical system design*, 2nd ed. McGraw-Hill Professional, 2008.
- [140] W. J. Smith, *Modern lens design*, McGraw-Hill, 2005.
- [141] D. H. Werner, J. P. Turpin, D. E. Brocker, X. Wang, Z. H. Jiang, and P. L. Werner, "Gradient-index lens design with quasi-conformal transformation optics for energy concentration," *Proc. SPIE*, 88340F, 2013.
- [142] Z. H. Jiang, M. Gregory, and D. H. Werner, "Experimental demonstration of a broadband transformation optics lens for highly directive multibeam emission," *Phys. Rev. B*, vol. 84, pp. 165 111(1)-(6), Oct. 2011.
- [143] R. W. Wood, *Physical optics*, Macmillan, 1905.
- [144] P. J. Sands, "Inhomogeneous lenses, II. chromatic paraxial aberrations," *J. Opt. Soc. Am.*, vol. 61, no. 6, pp. 777-783, Jun. 1971.
- [145] P. J. Sands, "Inhomogeneous lenses, V. chromatic paraxial aberrations of lenses with axial or cylindrical index distributions," *J. Opt. Soc. Am.*, vol. 61, no. 11, pp. 1495-1500, Jun. 1971.
- [146] J. Corsetti, P. McCarthy and D. Moore, "Color correction in the infrared using gradient-index materials," *Opt. Eng.*, vol. 52, no. 11, pp. 112109, Nov. 2013.
- [147] R. Flynn, E. Fleet, G. Beadie and J. Shirk, "Chromatic analysis and design of a first-order radial GRIN lens," *Opt. Express*, vol. 23, no. 17, pp. 22069, Aug. 2015.
- [148] S. D. Campbell, D. E. Brocker, J. Nagar, and D. H. Werner, "SWaP reduction regimes in achromatic GRIN singlets," *Appl. Opt.*, vol. 66, no. 13, pp. 3594-3598, May 2016.
- [149] M. Rahm, S. A. Cummer, D. Schurig, J. B. Pendry, and D. R. Smith, "Optical design of reflectionless complex media by finite embedded coordinate transformation," *Phys. Rev. Lett.*, vol. 21, pp. 063903(1)-(4), Feb. 2008.
- [150] Q. Wu, Z. H. Jiang, O. Quevedo-Teruel, J. P. Turpin, W. Tang, Y. Hao, and D. H. Werner, "Transformation optics inspired multibeam lens antennas for broadband directive radiation," *IEEE Trans. Antennas and Propag.*, vol. 61, no. 12, pp. 5910-5922, Dec. 2013.
- [151] J. P. Turpin, J. A. Bossard, K. L. Morgan, D. H. Werner, and P. L. Werner, "Reconfigurable and tunable metamaterials: A review of the theory and applications," *Inter. J. of Antennas and Propag.*, vol. 2014, no. 429837, pp. 1-18, May 2014.
- [152] X. Q. Lin, T. J. Cui, J. Y. Chin, X. M. Yang, Q. Cheng, and R. Lui, "Controlling electromagnetic waves using tunable gradient dielectric metamaterial lens," *Appl. Phys. Lett.*, no. 92, pp. 131904(1)-(3), Apr. 2008.

VITA
Donovan E. Brocker

Education

The Pennsylvania State University, University Park, PA
Ph.D. in Electrical Engineering, (8/10-8/16).

University of Wisconsin-Milwaukee, Milwaukee, WI
B.S. in Electrical Engineering, (9/03-5/10).

Selected Journal Publications

1. **D. E. Brocker**, Z. H. Jiang, M. D. Gregory, and D. H. Werner, submitted to *IEEE Trans. Antennas Propagat.*
2. **D. E. Brocker**, P. E. Sieber, J. A. Waynert, J. Li, P. L. Werner, and D. H. Werner, *IEEE Antennas Propag. Mag.*, **57**, 164-176, (2015).
3. **D. E. Brocker**, J. P. Turpin, P. L. Werner, and D. H. Werner, *IEEE Antennas and Wireless Propagat. Lett.*, **13**, 1787-1791, (2014).
4. S. D. Campbell, **D. E. Brocker**, J. Nagar, and D. H. Werner, *Applied Optics*, **55**, 3594-3598, (2016).
5. J. Nagar, **D. E. Brocker**, S. D. Campbell, J. A. Easum, and D. H. Werner, *Optics Express*, **24**, 9359-9368, (2016).
6. S. D. Campbell, J. Nagar, **D. E. Brocker**, and D. H. Werner, *Journal of Optics*, **18**, 044019(1)-(8), (2016).
7. K. L. Morgan, **D. E. Brocker**, S. D. Campbell, D. H. Werner, and P. L. Werner, *Optics Letters*, **40**, 2521-2524, (2015).
8. A. H. Panaretos, **D. E. Brocker**, and D. H. Werner, *IEEE Antennas and Wireless Propagat. Lett.*, **14**, 1089-1092, (2015).
9. N. Damiano, J. Li, C. Zhou, **D. E. Brocker**, Y. Qin, D. H. Werner, and P. L. Werner, Accepted for publication in *IEEE Trans. Ind.*
10. Z. H. Jiang, Q. Wu, **D. E. Brocker**, P. E. Sieber and D. H. Werner, *IEEE Trans. Antennas and Propag.*, **62**, 1173-1184, (2014).
11. Z. H. Jiang, **D. E. Brocker**, P. E. Sieber, and D. H. Werner, *IEEE Trans. Antennas Propagat.*, **62**, 4021-4030, (2014).

Book Chapters

1. D. H. Werner, M. D. Gregory, Z. H. Jiang, and **D. E. Brocker**, "Optimization Methods in Antenna Engineering," Chapter in Handbook of Antenna Technologies, edited by Z. N. Chen, D. Liu, H. Nakano, X. Qing, and T. Zwick, Springer, pp. 1-47, 2016.
2. J. Nagar, S. D. Campbell, **D. E. Brocker**, X. Wang, K. L. Morgan, and D. H. Werner, "Broadband performance of lenses design with quasiconformal transformation optics," Chapter in Broadband Metamaterials in Electromagnetics: Technology and Applications, edited by D. H. Werner, Pan Stanford, to appear in 2017.